ATLAS Note
ANA-HDBS-2021-23-INT1
August 3, 2022
Draft version 0.7.5

Search for $X \to SH$ model in the final states of two photons and multiple leptons using 139 fb^{-1} of proton-proton collision data at $\sqrt{s}$ = 13 TeV recorded with the ATLAS detector at the LHC

Yaquan Fang[a], Kaili Zhang[a], Zhijun Liang[a], Bo Liu[a], Xinchou Lou[a,c], Xin Shi[a], Qiyu Sha[a], Shuiting Xin[a], Wei-Ming Yao[b], Yesenia Hernandez Jimenez[d], Fangyi Guo[a]

[a]*Institute of High Energy Physics, Chinses Academy of Sciences, Beijing, China*
[b]*Lawrence Berkeley National Laboratory, USA*
[c]*University of Texas at Dallas, USA*
[d]*University of Valencia, Spain*

This note presents a search for a new heavy scalar particle X decaying into a Standard Model Higgs boson and a singlet scalar particle S using 139 fb^{-1} of proton-proton collision data at the centre-of-mass energy of 13 TeV recorded with the ATLAS detector at LHC. The explored X mass range varies from 300 GeV to 1000 GeV, with the corresponding S mass range being from 170 GeV to 500 GeV. This search uses the event signature of two photons from the Higgs boson decay and one or two leptons (e or μ) coming from the process of $S \to WW/ZZ$. The observed (expected) upper limits at the 95% confidence level on the cross-section for $gg \to X \to Sh$ assuming the decay of S following the SM prediction is between X fb (167 fb) and Y fb (710 fb).

List of contributions

Yaquan Fang	Contact editor, optimization, supervision of IHEP students
Kaili Zhang	Contact editor, optimization, plots production, signal/background estimation, systematics and limit setting
Zhijun Liang	Analysis Optimization for BDT and supervision of Bo Liu
Bo Liu	Analysis Strategy and editor of the note
Xinchou Lou	Statisics and supervisiion of Shuiting Xin
Xin Shi	Optimization of the analysis and supervisiion of Kaili Zhang
Qiyu Sha	Signal sample preparation, plotting
Shuiting Xin	Signal sample preparation
Wei-Ming Yao	the optimiazation of BDT analysis and editor of the note
Yesenia Hernandez Jimenez	Editor of the note
Fangyi Guo	Editor of the note

Contents

To do list

0.1 Updated time: 19th Sep. 2021.

- full CP systematics implement. Est. time: 1 week.
- background estimated from 0l region, lepton depandancy study. Est. time: 1 week when samples are ready.
- different function forms to fitting. Est. time: in parallel with background estimation.

0.2 Updated time: 6th Dec. 2021.

- Spurious signal test for different background functions. Est. time: 1 week.
- Reco-level background estimation. Est. time: 1 week when samples are ready.
- The validations of this parametrized BDT method. Est. time: 1 week.
- Implement all mass points with kinematic distributions, BDT outputs, CP systematics plots in the appendix. Est. time: 1 week.
- Describe the selection of BDT input variables in appendix. Est time: 1-2 week.
- Theoretical uncertainties for signal and single higgs sample used. Est time: 1 month.
- More specific explanation for the comments raised by the community. Est time: -.

0.3 Updated time: 16th Feb. 2022.

- explanation for SS test, Theoretical uncertainties, background shape study, CP systematics
- interpretation for independent WW,ZZ poi, extrapolate to whole planes
- MXAOD cutflow and plot to show table 8,9 better.
- describe how variables are selected, correlation and variable importance. change plot accrodingly.
-

0.4 Updated time: 31th July. 2022.

- To add the parton Shower uncertainty

Changelogs

0.1

Updated time: 19th Sep. 2021.

- Refine the MC ratio to make MC and sideband data more consistent.
- Use BDT instead of BDTG. better consistence between data sideband and MC.
- More description for analysis strategy.

0.2

Updated time: 30th Nov. 2021.

- Updating systematics implementation. Major NPs studied.
- More description for analysis strategy.

0.3

Updated time: 1st Dec. 2021.

- 4.2 Adding the definations for BDT-High and BDT-Middle regions and the BDT cut values.
- 5 Adding the statements for ZZ2l and WW1e1m. Replace plots.
- 5.2 and 6.2.2. How the background is modelled and How the lepton dependence systematics implemented.

0.4

Updated time: 3rd Dec. 2021.

- Replying the questions from convenors.

0.5

Updated time: 6th Dec. 2021.

- Replying the questions from CDS comments.
- Lepton efficiencies explained in p.19 Section 3.2.
- Cross validation method the ks test plots are replaced by the individual folds plots to avoid confusion. See Section 4.1.2
- Alternative cut solution discussed.
- Better text all over the draft.

0.6

Updated time: June 2022, aiming for 2nd EB circulation.

- Section 6: Add details about syst.
- Add Appendix A: visualized the cutflow and moved the numbers in appendix.
- Add Appendix E: diphoton vertex check for SH samples

0.7

Updated time July 2022, aiming for the 2nd EB meeting in August.

- Section 5: Add the spurious signal study.
- Add Appendix G: The inject test is added.
- Add Appendix F: The toylimit is added.
- Add Appendix C: The detail of reweighted method is added.

1 Introduction

The discovery of the Higgs boson (H) by the ATLAS and CMS Collaborations in 2012 [1, 2] is a milestone in the particle physics. Studies of its properties indicate that the behaviour of this observed particle is consistent with the Standard Model (SM) prediction. However, this doesn't preclude the possible new physics, e.g. the presence of heavy scalar boson coupling to two Higgs bosons or some mixtures of additional scalars coupling to the SM Higgs boson.

In the former case, scenarios of extended Higgs sectors could enhance the Higgs boson pair productions significantly. One of the most common trials is to search the heavier CP-even component of the two Higgs-doublet model (2HDM) decaying to two Higgs bosons. Both ATLAS and CMS have preformed exhaustive searches for heavy Higgs boson with Run-1 and Run-2 data and no obvious excess has been observed [3–5].

One possibility for the latter case is to extend the 2HDM model by introducing a new scalar singlet, S, in the process through the decay $X \to SH$ [6, 7], where X is the heavy CP-even scalar as predicted by the extended 2HDM model (2HDM+S model) and H represents the SM Higgs boson. In this model, the heavy scalar X has Yukawa couplings to other SM particles and is assumed to be related to Electroweak Symmetry Breaking(EWSB), where the Higgs field acquires mass according to the Vacuum expectation value(VEV). As a singlet scalar, S is assumed to only interact with X and the SM Higgs boson, and its couplings to other SM particles are substantially suppressed. This allows the production of S only through the process of $X \to SH, SS$. The production processes are illustrated with Feynman diagrams presented in Figure 1 where X is produced dominantly through gluon fusion (ggF), and has the dominant decay modes $X \to SS$ and $X \to SH$.

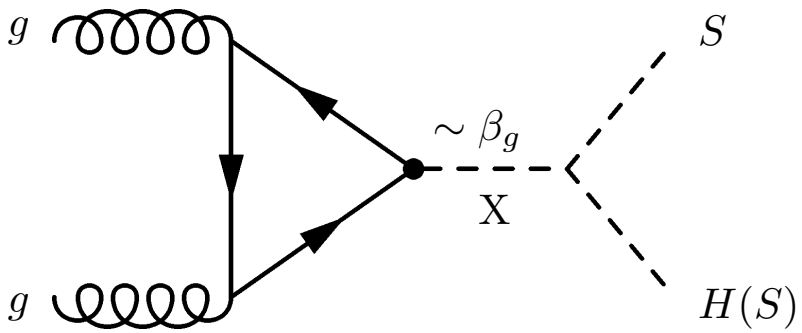

Figure 1: Representative diagrams that contribute to $X \to SH, SS$ via the gluon fusion process.

The ggF production cross-section is considered to be SM-like as a function of m_X, which is also modifiable by a free parameter β_g, a dimensionless constant that multiplies the effective g-g-X coupling in the BSM

Lagrangian. A more concrete statement would be that the production cross section is given by:

$$\sigma_X = \beta_g^2 \sigma_{\mathrm{SM}}^{\mathrm{ggF}}(m_X). \tag{1}$$

The relative decay rates of these two X decay modes are considered as a free parameter, and can be controlled by the ratio a_1 of their branching ratios (BRs):

$$a_1 = \frac{\mathrm{BR}(X \to SS)}{\mathrm{BR}(X \to SH)}. \tag{2}$$

It is convenient to have the assumption of $\mathrm{BR}(X \to SH) = 1$ by considering the lack of sensitivity to probe a_1 directly. In addition, the cross-section of X from ggF production is assumed to be 1 pb as a benchmark, and X mass has been chosen from 300 to 1000 GeV. The BSM model often treats S as a portal to the Dark Matter (DM) interactions through the decay $S \to \chi\chi$ where χ is a DM candidate. However, the DM interpretation completely decouples from this search and $\mathrm{BR}(S \to \chi\chi)$ can be set to 0 without any loss of generality. Moreover, in this study, S is assumed to share the same decay BRs as the SM Higgs like particle[8, 9], as documented in the Higgs Yellow Report 4[10]. In addition, for the convenience of the theoretical interpretations, the upper limits assuming 100% decaying to $W^{\pm}W^{\mp}$ or ZZ will also be addressed in the note.

For the chain decay of X, on the one hand, S masses are assumed to be higher than H, ranging from 170 GeV up to 500 GeV. Thus, we focus on the dominant decays of S, i.e. $S \to W^{\pm}W^{\mp}$ and $S \to ZZ$ in this study. The sum of these two decay modes counts no less than 80% of the total branch ratio of S decay. The rest is mostly occupied by $t\bar{t}$ decay in particular if S mass is higher than $t\bar{t}$ mass threshold. In order to effectively reject huge QCD backgrounds, one or two lepton the final states from $S \to W^{\pm}W^{\mp} or ZZ$ are required in this analysis. These requirements lead to this search mainly in final states of $X \to SH \to \gamma\gamma + 1, 2$ leptons.

On the other hand, $\gamma\gamma$ decay of the H is chosen to take the advantage of the excellent di-photon mass resolution and smooth sideband when estimating backgrounds as well as to further suppress the QCD background. In addition, a fit on the di-photon mass spectrum can be implemented to extract the signal.

Finally, b-jet veto is implemented in the analysis to avoid the overlap with any bb related final states covered by other analyses.

This note provides supporting material for the search of $X \to SH$ model in the final states of di-photon and multi-leptons using 139 fb^{-1} of proton-proton collision data at $\sqrt{s}$ = 13 TeV. It is organized as follows. In Section 1, the current data set and the MC samples relevant for this analysis are described. Section 2 defines the objects such as photon, lepton, jet etc. used in this analysis. In Section 3, the event selections are summarized. Section 4 describes the BDT method to optimize the analysis. The estimations of the signal and various backgrounds are discussed in Section 5. In Section 6, the systematic uncertainties are presented. Section 7 documents the statistical procedure used to extract the sensitivity of the analysis. Finally, Section 9 summarizes the results and conclusions of the study in this note.

sectionData and Monte Carlo samples

1.1 Data samples

The data samples used in this analysis correspond to the data collected by ATLAS during 2015-2018 at the center of mass $\sqrt{s}$ = 13 TeV, which sums up to an integrated luminosity of $(139.0 \pm 2.4)\,\text{fb}^{-1}$ [11, 12] after the data quality requirement [13]:

- Year 2015: data15_1V3TeV.periodAllYear_DetStatus-v89-pro21-02_Unknown_PHYS_StandardGRL_All_Good_25ns.xml
- Year 2016: data16_13TeV.periodAllYear_DetStatus-v89-pro21-01_DQDefects-00-02-04_PHYS_StandardGRL_All_Good_25ns.xml
- Year 2017: data17_13TeV.periodAllYear_DetStatus-v99-pro22-01_Unknown_PHYS_StandardGRL_All_Good_25ns_Triggerno17e33prim.xml
- Year 2018: data18_13TeV.periodAllYear_DetStatus-v102-pro22-04_Unknown_PHYS_StandardGRL_All_Good_25ns_Triggerno17e33prim.xml

Events are selected by a logical OR of a diphoton trigger and a single photon trigger. The former has transverse energy thresholds of 35 GeV and 25 GeV for leading and sub-leading photon candidates. The single trigger requires an energy threshold of 120 GeV for 2015-2016 data and 140 GeV for 2017-2018 data to enhance acceptance in the very high p_T^H region. Loose photon isolation requirements [14] are applied by this diphoton trigger in 2015-2016 and are tightened in 2017 to cope with a higher instantaneous luminosity.

1.2 Monte Carlo samples

SM single Higgs and dihiggs events are estimated with Monte Carlo (MC) simulated samples that are documented in this section, while the continuum photon background of the SM processes with di-photon and multiple leptons is determined with the data in sideband[1] with the data-driven method. Nevertheless, two relevant MC samples, vector boson production associated with photons ($V+\gamma\gamma$, $VV+\gamma\gamma$) and multi-jet processes associated with photons ($\gamma\gamma$+jets) are used to check and validate the performance of TMVA modeling and are described in this section.

There are three MC campaigns used for each simulated process, mc16a, mc16d and mc16e, which correspond to different assumptions on the distribution of the number of interactions per branching crossing in 2015-2016, 2017 and 2018 periods, respectively. To match the number of interactions in data, the Monte Carlo samples are reweighted to the observed distribution using the `PileupReweightingTool` [15]. These multiple overlaid proton-proton collisions are simulated with the soft QCD processes of Pythia 8.186 [16] using the A2 set of tuned parameters [17] and the MSTW2008LO PDF set.

[1] The sideband is defined as $m_{\gamma\gamma} \in [105, 120] \cup [130, 160]$ GeV orthogonal to the signal region defined in Section 3.

1.2.1 MC samples for signals

For 2HDM+S signal production, the event generation is performed at the leading-order (LO) accuracy with PYTHIA8 [16] for matrix element calculation. Parton showering and hadronization are also simulated using the PYTHIA8 generator with the A14 tune [18] and using the NNPDF 2.3 LO PDF set [19]. The EVTGEN [20] program is used for b- and c-hadron modeling. Detector effects are simulated using AltFastII(AF2) [21], in which the calorimeter response is fast simulated.

Two scalars, X and S, are assumed to have a narrow width with respect to the experimental resolution. Technically, their decay widths are set to 10 MeV in the event generation. The heavier boson X is constrained to decay only to S and H, with S decaying to a pair of W or Z bosons. In order to suppress QCD backgrounds, semi-leptonic and full leptonic decays of WW are taken into account in the analysis. While for ZZ case, the final state with 2 leptons is considered. The decay of ZZ into 4 leptons is not used in this study due to the limited statistics. The SM H boson from X decay is required to decay into a pair of photons. Thus three dedicated samples with the following final states are produced: $\gamma\gamma + WW(\ell\nu q\bar{q}')$, $\gamma\gamma + WW(\ell\nu\ell\nu)$ and $\gamma\gamma + ZZ(\ell\ell q\bar{q})$. Each of these 3 samples has 200k events. In addition, a `MultiLeptonFilter` requires the transverse momentums of the leptons with $p_{\mathrm{T}} > 7$ GeV and $|\eta| < 3$. To produce on-shell W or Z bosons from S decay, the lower bound of m_S is set to 170 GeV.

In order to perform an efficient search on $X \to S + H$ process, a total of 20 signal MC simulated samples corresponding to various combinations of m_X and m_S hypotheses for each of the three final states are generated to cover the most interesting phase space. The mass grid is shown in Figure 2. The signal sample lists of all three channels $\gamma\gamma + \ell\nu q\bar{q}'$, $\gamma\gamma + \ell\nu\ell\nu$ and $\gamma\gamma + \ell\ell q\bar{q}$ are presented in Table 2, Table 3 and Table 4, respectively.

Taking $\gamma\gamma + \ell\nu q\bar{q}'$ in $m(X, S) = (1000, 170)$ GeV as an example, the value of the cross-section in the first row of Table 2 is calculated by the following formula:

$$\begin{aligned} &\sigma(X \to SH) \times Br_{(S_{170} \to WW)} \times Br_{(H_{125} \to \gamma\gamma)} \times k_{Ef\,f_{Filter}} \\ &= 1pb \times 96.28\% \times 0.0228\% \times 38.74\% \\ &= 8.50 \times 10^{-4} pb \end{aligned} \tag{3}$$

One example jobOption file to generate signal samples with Pythia8 is in Appendix B. For $\gamma\gamma + \ell\nu\ell\nu$ channel, both W bosons are forced to decay leptonically at the generator level, which means an extra $Br_{(WW \to \ell\nu\ell\nu)} = 10.71\%$ needs to be counted. For $\gamma\gamma + \ell\ell q\bar{q}$ channel, although the $ZZ \to \ell\ell\nu\nu$ is not forbidden at the generator level, the contribution from this final state is low, thus ignored in the analysis.

In this study, the expected branching ratios of the decay from S are assumed to be the same as the heavy Standard Model-like Higgs boson as well as 100% decay to WW/ZZ. In either case, the Parameter Of Interest(POI) of this study will be the $\sigma(pp \to X) \times Br(X \to Sh)$. In former case, the branching ratios of S decay to WW and ZZ are fixed at the SM prediction, as shown in Table 1.

1.2.2 MC samples for SM single Higgs and Di-Higgs backgrounds

Simulated samples for SM single Higgs backgrounds are produced to investigate their contributions in $m_{\gamma\gamma}$ peak around 125 GeV. The SM single Higgs backgrounds considered here are produced via five production modes: ggH, VBF, WH, ZH and ttH, where H represents the 125 GeV Higgs boson.

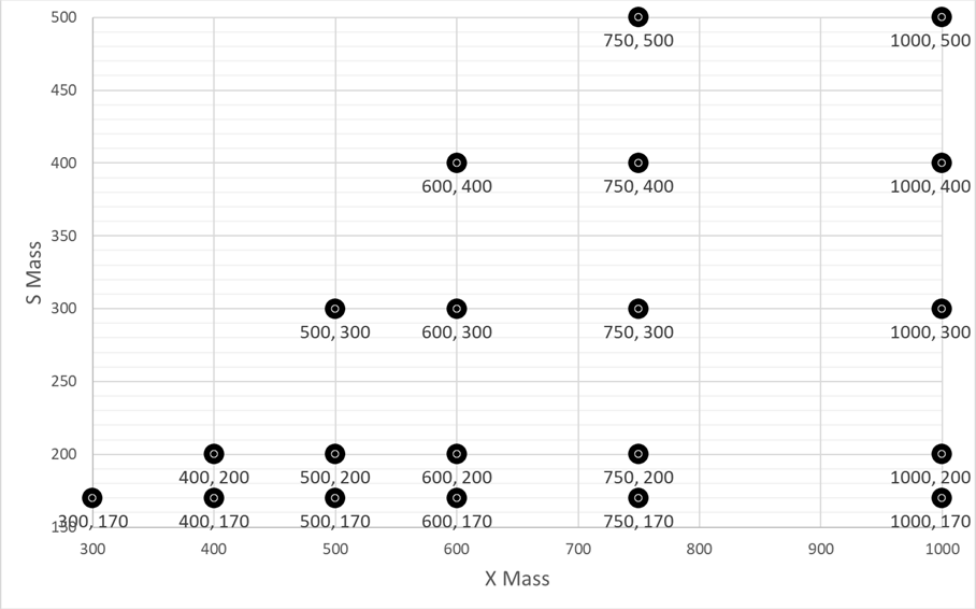

Figure 2: The m_X and m_S grid for the generated signal samples.

The MC simulated events for the ggH process are produced with the PowHegv2 generator at the next-to-leading-order (NLO) accuracy and interfaced to Pythia8 for Parton showering (PS). The PDF4LHC15 PDF set is used for incoming parton description in the matrix element (ME) calculation, and the CTEQ6L1 [23] set is used for parton showering calculation with the AZNLO tuned parameters for hadronization and factorization [24]. The EvtGen program is used for b- and c-hadrons modeling.

Kinematic distributions are also reweighted to the next-to-next-to-leading-order (NNLO) and next-to-next-to-leading-logarithmic (NNLL) calculation to have a better prediction of the Higgs boson p_{T} and rapidity [25]. The Parton shower simulation is also at the NNLO level, called NNLOPS [26]. Events are normalized to the cross-section calculated at the next-to-next-to-next-to-leading-order ($\mathrm{N^3LO}$) QCD accuracy with the NLO EW corrections [27].

The VBF production events are generated with the PowHegv2 generator at the NLO accuracy and interfaced to Pythia8 for Parton showering. The PDF4LHC15 set is used for ME calculation, and the CTEQ6L1 set is used for PS with AZNLO tuned parameters incorporated with EvtGen for b- and c-hadrons modeling.

m_S[GeV]	$BR(S \to WW)$	$BR(S \to ZZ)$
170	96.28%	2.44%
200	73.90%	25.68%
300	69.12%	30.72%
400	57.65%	26.90%
500	54.09%	25.86%

Table 1: The branching ratios of WW and ZZ from S following the decay of a Higgs-like particle for different masses from [22]

Generated events are normalized to the cross-section calculated at the NLO QCD accuracy with the NNLO QCD and NLO EW corrections applied.

Events corresponding to the Higgs boson production in association with the vector boson (WH and ZH) are generated with Powhegv2 for ME and interfaced to Pythia8 for PS. The PDF4LHC15 set is used for ME calculation and the CTEQ6L1 set is used for PS with the AZNLO tune. The EvtGen program is used for b- and c-hadron modeling. All samples except for $gg \to ZH$ are generated at the NLO QCD accuracy while events for $gg \to ZH$ are produced at the LO QCD accuracy. Events are finally normalized to corresponding higher-order cross-sections respectively.

Both ttH and bbH events are generated with the Powhegv2 generator and interfaced to Pythia8 for PS. The PDF4LHC15 set is used for ME calculation and the NNPDF2.3 set [28] is used for PS calculation with the A14 tune [18]. The EvtGen program is used for b- and c-hadron modeling. Events are normalized to cross-section calculation at the NLO QCD accuracy with the NLO EW correction applied.

Samples for single Higgs boson production in association with single top-quark are generated with the MadGraph5_aMC@NLO generator for ME calculation at the NLO QCD accuracy and interfaced to Pythia8 for Parton showering. Two final state samples are considered: tHW and $tHbj$ in this analysis. The NNPDF3.0 set is used for ME calculation and the NNPDF2.3 set is used for PS with A14 tune incorporated with EvtGen for b- and c-hadron modeling.

SM ggF Di-Higgs processes are generated with Powheg-Box-V2 generator at NLO and interfaced to Herwig7.1 for Parton shower. The PDF4LHC15 set is used for ME calculation. A set of lepton filters are

DSID	m_X [GeV]	m_S [GeV]	$\sigma \times BR(h \to \gamma\gamma)$ [pb]	Filter efficiency	N_{events}
800938	1000	170	0.0008504143	38.74%	200000
800939	1000	200	0.0006439764	38.22%	200000
800940	1000	300	0.0006131967	38.91%	200000
800941	1000	400	0.0005170928	39.34%	200000
800942	1000	500	0.000494904	40.13%	200000
800943	300	170	0.0008488777	38.67%	200000
800944	400	170	0.0008657806	39.44%	200000
800945	400	200	0.0006562763	38.95%	200000
800946	500	170	0.0008574389	39.06%	200000
800947	500	200	0.0006796967	40.34%	200000
800948	500	300	0.0005700161	36.17%	200000
800949	600	170	0.0008302186	37.82%	200000
800950	600	200	0.0006372367	37.82%	200000
800951	600	300	0.000611148	38.78%	200000
800952	600	400	0.0005153841	39.21%	200000
800953	750	170	0.00081134	36.96%	200000
800954	750	200	0.0006402696	38.00%	200000
800955	750	300	0.0006046866	38.37%	200000
800956	750	400	0.0005139382	39.10%	200000
800957	750	500	0.0004878745	39.56%	200000

Table 2: Signal samples for $\gamma\gamma + \ell\nu q\bar{q}'$ final state.

applied targeting $\gamma\gamma$+multi-lepton final states in this analysis, requiring the lepton kinematic at $p_T > 7$ GeV and $|\eta| < 3$. No kinematic cut for the photon is required at the generator level.

These samples are simulated using the full ATLAS simulation and reconstruction chain. The mass of the SM Higgs boson is set to 125 GeV. A summary is listed in Table 5.

1.2.3 MC samples for continuum backgrounds

3 different types of continuum backgrounds are used in this study: $\gamma\gamma + multijets$, $V + \gamma\gamma$ and $t\bar{t}\gamma\gamma$. In addition to these samples, dedicated $\gamma\gamma + 0\ell$, $\gamma\gamma + \ell\nu$ jj, and $\gamma\gamma + \ell\nu\ell\nu$ are generated to demonstrate the consistency of $m_{\gamma\gamma}$ distributions with the above three samples. This allows one to estimate the shape of $m_{\gamma\gamma}$ distributions in $\gamma\gamma + \ell\nu$ jj, and $\gamma\gamma + \ell\nu\ell\nu$ samples with that from $\gamma\gamma + 0\ell$ sample. Of course, the corresponding differences should be counted as one source of the systematics.

$\gamma\gamma + multijets$ samples, generated with Sherpa 2.2.4, describe the continuum background shape for the diphoton spectrum. The main processes are dressed up by ME NNPDF30 and PDF4LHC15 in NNLO when the number of jets is equal to 0 or 1. For events with more than two jets, the accuracy is NLO. Moreover, the diphoton mass spectrum has been constrained to between 90 GeV to 175 GeV in LO. Note that multijets samples do not have real leptons in the final states, so these samples can be treated as a fake background since the lepton originates from a misidentified jet.

DSID	m_X [GeV]	m_S [GeV]	$\sigma \times BR(h \to \gamma\gamma)$ [pb]	Filter efficiency	N_{events}
800958	1000	170	0.0001352752	57.56%	200000
800959	1000	200	0.0001054183	58.44%	200000
800960	1000	300	9.95782e-05	59.02%	200000
800961	1000	400	8.38138e-05	59.56%	200000
800962	1000	500	7.81892e-05	59.22%	200000
800963	300	170	0.0001246525	53.04%	200000
800964	400	170	0.0001272142	54.13%	200000
800965	400	200	9.83111e-05	54.50%	200000
800966	500	170	0.0001303869	55.48%	200000
800967	500	200	9.93753e-05	55.09%	200000
800968	500	300	9.63557e-05	57.11%	200000
800969	600	170	0.0001313035	55.87%	200000
800970	600	200	0.0001013776	56.20%	200000
800971	600	300	9.62207e-05	57.03%	200000
800972	600	400	8.14497e-05	57.88%	200000
800973	750	170	0.0001331366	56.65%	200000
800974	750	200	0.0001035423	57.40%	200000
800975	750	300	9.76548e-05	57.88%	200000
800976	750	400	8.22799e-05	58.47%	200000
800977	750	500	7.78723e-05	58.98%	200000

Table 3: Signal samples for $\gamma\gamma + \ell\nu\ell\nu$ final state.

$V + \gamma\gamma$ samples are generated with generator SHERPA in version 2.2.4 and the basic accuracy is also NNLO in NNPDF30. Additionally, the photon pT is required to be larger than 17 GeV and diphoton mass larger than 80 GeV in LO accuracy. with the different final states, those samples are separated as $ee + \gamma\gamma$, $\mu\mu + \gamma\gamma$, $\tau\tau + \gamma\gamma$, $e\nu + \gamma\gamma$, $\mu\nu + \gamma\gamma$, $\tau\nu + \gamma\gamma$, and $\nu\nu + \gamma\gamma$. Those processes had one or two real leptons in the final states and share the similar kinematics as our signals, so they make important contributions the background, especially in 2-lepton cases.

Another sample used in this analysis is the top-pair production in association with two photons where both top-quarks decay hadronically or one of them decay leptonically: $t\bar{t}\gamma\gamma$ (noallhad) and $t\bar{t}\gamma\gamma$ (allhad). Events for such processes are generated with MADGRAPH5_AMC@NLO generator and interfaced to PYTHIA8 for Parton showering.

Although the MCs have been simulated to describe the continuum backgrounds, only the data sideband is reliable. The consistency study between MC and data and rescaling of the MC corresponding to the data sideband will be done in Section 4. Moreover, the treatments of the continuum backgrounds for $\gamma\gamma + \ell\nu$ jj, and $\gamma\gamma + \ell\nu\ell\nu$ are done separately due to their different background components.

DSID	m_X [GeV]	m_S [GeV]	$\sigma \times BR(h \to \gamma\gamma)$ [pb]	Filter efficiency	N_{events}
800978	1000	170	7.8942e-06	14.19%	200000
800979	1000	200	8.74157e-05	14.93%	200000
800980	1000	300	0.000109405	15.62%	200000
800981	1000	400	9.66592e-05	15.76%	200000
800982	1000	500	9.55755e-05	16.21%	200000
800983	300	170	7.2488e-06	13.03%	200000
800984	400	170	7.4936e-06	13.47%	200000
800985	400	200	8.32587e-05	14.22%	200000
800986	500	170	7.7106e-06	13.86%	200000
800987	500	200	8.95236e-05	15.29%	200000
800988	500	300	0.0001054826	15.06%	200000
800989	600	170	8.011e-06	14.40%	200000
800990	600	200	8.44297e-05	14.42%	200000
800991	600	300	0.0001033814	14.76%	200000
800992	600	400	9.11394e-05	14.86%	200000
800993	750	170	7.7551e-06	13.94%	200000
800994	750	200	9.0636e-05	15.48%	200000
800995	750	300	0.0001070936	15.29%	200000
800996	750	400	9.45126e-05	15.41%	200000
800997	750	500	9.38656e-05	15.92%	200000

Table 4: Signal samples for $\gamma\gamma + \ell\ell q\bar{q}$ final state.

DSID	Generator	PDF (ME)	PDF+Tune (PS)	Prod. Mode	Events in AOD
343981	NNLOPS + Pythia8	PDF4LHC15	AZNLOCTEQ6	ggH	18.3M
346214	Powheg + Pythia8	PDF4LHC15	AZNLOCTEQ6	VBF	7M
345318	Powheg + Pythia8	PDF4LHC15	AZNLOCTEQ6	W^+H	0.6M
345317	Powheg + Pythia8	PDF4LHC15	AZNLOCTEQ6	W^-H	0.6M
345319	Powheg + Pythia8	PDF4LHC15	AZNLOCTEQ6	$qq \rightarrow ZH$	1.5M
345061	Powheg + Pythia8	PDF4LHC15	AZNLOCTEQ6	$gg \rightarrow ZH$	0.15M
346525	Powheg + Pythia8	PDF4LHC15	A14NNPDF23	ttH	7.8M
345315	Powheg + Pythia8	PDF4LHC15	A14NNPDF23	bbH	0.299M
346188	MGMCatNLO + PYTHIA8	NNPDF	A14NNPDF23	tHbj	0.4M
346486	MGMCatNLO + PYTHIA8	NNPDF	A14NNPDF23	tHW	0.208M
345868	MGMCatNLO + PYTHIA8			$t\bar{t}\gamma\gamma$ (noallhad)	1.94M
345869	MGMCatNLO + PYTHIA8			$t\bar{t}\gamma\gamma$ (allhad)	1.6M
600542	Powheg + Herwig7	PDF4LHC15		SM Dihiggs $\gamma\gamma$+0L	0.1M
600543	Powheg + Herwig7	PDF4LHC15		SM Dihiggs $\gamma\gamma$+1L	0.5M
600544	Powheg + Herwig7	PDF4LHC15		SM Dihiggs $\gamma\gamma$+2L	0.5M
507017	MadGraph+ PYTHIA8	PDF4LHC15	NNPDF23LO	$\gamma\gamma$+0L	500k
504650	MadGraph+ PYTHIA8	PDF4LHC15	NNPDF23LO	$\gamma\gamma$+1L	200k
507018	MadGraph+ PYTHIA8	PDF4LHC15	NNPDF23LO	$\gamma\gamma$+2L	200k

Table 5: Summary of nominal Single Higgs, dihiggs and di-photon background samples

2 Object definition

This section outlines the photon, lepton, jet, and E_T^{miss} selections used in this analysis.

2.1 Photons

The photon is reconstructed by using the supercluster method with the energy deposits in the EM calorimeter. The detailed photon performance for Run-2 analyses can be found in Ref. [29]. A photon candidate is required to have $p_{\mathrm{T}} > 25\,\mathrm{GeV}$ and $|\eta| < 2.37$. Photon inside the crack region $1.37 < |\eta| < 1.52$ is rejected. The photon candidate is also required to pass the *Tight* cut-based photon identification selection which is based on the longitudinal and transverse shower profiles measured in the calorimeter. In addition, the photon candidate has to be isolated and passes both calorimeter-based isolation topoEtCone20$< 0.065 \times p_{\mathrm{T}}$ and track-based isolation ptcone20$< 0.05 \times p_{\mathrm{T}}$. A candidate event is required to have at least two good isolated photons. To match the trigger threshold, the leading photon is required to have $p_{\mathrm{T}} > 35\,\mathrm{GeV}$ and the subleading photon with $p_{\mathrm{T}} > 25\,\mathrm{GeV}$.

2.2 Jets and b-jets

The jet used in this analysis is reconstructed by the anti-k_t algorithm with radius parameter $R = 0.4$ from the particle-flow objects. The particle-flow (PFlow) algorithm provides a list of tracks and a list of topo-clusters containing both the unmodified topo-clusters and a set of new topo-clusters resulting from the energy subtraction procedure. The algorithm attempts to match each track to a single topo-cluster in the calorimeter. The expected energy deposited in the calorimeter (based on topo-cluster position and the track momentum) is subtracted cell by cell from the set of matched topo-clusters. If the remaining energy is consistent with the expected shower fluctuations of a single particle's signal, the topo-cluster remnants are removed [30].

To increase the efficiency of primary vertex identification in the presence of photons, HGam analyses are using a Neural Network relying on the tracks as well as the di-photon system [31]. The corresponding efficiency check for this study has been documented in Appendix E. The reconstructed jet collection is called `AntiKt4PFlowCustomVtxHggJets` [29] and is used as default in all analyses as well as in this document unless stated differently. Technical details on the collection used are shown in Table 6.

Collection name:	`AntiKt4PFlowCustomVtxHggJets`, `AntiKt4EMPFlowJets`
Configuration file:	`JES_MC16Recommendation_Consolidated_PFlow_April2019_Rel21`
Calibration sequence:	`JetArea_Residual_EtaJES_GSC_Smear[_Insitu]`
Calibration area version:	00-04-82

Table 6: PFlow jet calibration recommendations. The `_Insitu` calibration is applied on data while the jet energy resolution `_Smear` is applied on MC.

The jet selection used for this analysis is:

- $p_{\mathrm{T}} > 25$ GeV.
- anti-kt R = 0.4.

- $|\eta| < 2.5$ (for central jets).
- $|y| < 4.4$
- Jet-Vertex Tagger (JVT) WP:Tight
- Jet cleaning WP:LooseBad

The flavour tagging algorithm used to determine the flavour of the jet is a high-level algorithm based on a deep neural network that uses the output of "recurrent neural network impact parameter" (RNNIP) as input. DL1r outputs three different probabilities (p_b, p_c and p_u) that are combined to define a final discriminant. DL1r algorithm has been re-optimized in 2019 in order to maximize the performance on the jet collections recommended for use in ATLAS, PFlow jets, and VR jets and to extend the algorithm performance to very high jet p_T [32],[33]. The b-tagging working point with a 77% efficiency is chosen, such efficiency is measured from $t\bar{t}$ MC samples and dedicated $t\bar{t}$ data. The associated SFs are taken into account.

2.3 Leptons

The selection of a lepton uses the official working point of identification and isolation.

- Electrons: Electrons are reconstructed by matching the energy deposits from the EM calorimeter to the track in the inner detector. It requires $p_T > 10$ GeV, $|\eta| < 1.37$ or $1.52 < |\eta| < 2.37$, Medium LH ID, $|d_0\text{significance}| < 5$, $|\Delta z_0 \sin\theta| < 0.5$ mm. Isolation requirements: topoEtCone20 $< 0.02 \times p_T$ and ptcone20 $< 0.15 \times p_T$.
- Muons: Muons are reconstructed by using the information of the Muon spectrometer and the Inner detector. The candidates should pass $p_T > 10$ GeV, $|\eta| < 2.7$, Medium ID, $|d_0\text{significance}| < 3$, $|\Delta z_0 \sin\theta| < 0.5$ mm and GradientLoose isolation criteria.

2.4 Missing transverse energy

The E_T^{miss} involves all the reconstructed and calibrated objects described above. Compared to the general definition, τ leptons are treated as normal hadronic jets here and do not change the performances [29]. The Track-based Soft Term (TST) is the chosen approach in all HGam analyses to compute the E_T^{miss} soft term and is therefore used here. Compared to the usual computation, this term is derived with respect to the chosen di-photon vertex instead of the usual hardest vertex.

2.5 Overlap removal

Since objects are reconstructed with different algorithms in parallel, one needs to implement a set of rules to remove objects close to each other to avoid double counting. This overlap removal is done just after full object definitions and two loose photons so that in the samples of reverse ID or reverse isolation, overlap removal is also implemented. The rules are defined below. More details can be found in Ref [34].

- The two leading photons are always kept.
- Electrons with $\Delta R(e, \gamma) < 0.4$ are removed.
- Jets with $\Delta R(jet, \gamma) < 0.4$ are removed.

- Jets with $\Delta R(jet, e) < 0.2$ are removed.
- Muons with $\Delta R(\mu, \gamma) < 0.4$ or $\Delta R(\mu, jet) < 0.4$ are removed
- Electrons with $\Delta R(e, jet) < 0.4$ are removed.

3 Event selection

3.1 Selections

The event selection procedure identifies two photons and then applies requirements on the existence of one or two leptons in order to increase the signal purity and background rejection. The event selection for the analysis starts with the full di-photon selection from the $h \to \gamma\gamma$ analysis in Run-2 to select two high p_{T} isolated photons. The selections listed below are similar to the other HGamma analyses, except for optimizations of the b-veto working point and the BDT selection that will be described in Sec 4.

- **Trigger**: di-photon trigger with two reconstructed photons with E_{T} larger than 35 and 25 GeV passing *loose* (2015/2016) and *medium* (2017/2018) requirements based on the energy leakage in the hadronic compartment and on the shower shape in the second layer of the electromagnetic calorimeter are used for the analysis.
  - HLT_g35_loose_g25_loose (2015/2016)
  - HLT_g35_loose_g25_medium_L12EM20VH (2017/2018)
- **Good Run List and Detector Quality**: Events must belong to the luminosity blocks specified in the Good Run Lists as Sec 1 shows. Events with data integrity errors in the calorimeters and incomplete events where some detector information is missing are rejected, as well as events which are corrupted due to power supply trips in the tile calorimeter.
- **Primary Vertex**: The primary vertex is selected using the neural network (NN) algorithm from HGam group. The photons' four momenta, JVT and track isolation are corrected with respect to this origin, and the mass of the di-photon system is accordingly recalculated.
- **2 tight isolated photons**: At least two tight isolated photons with $E_{\mathrm{T}} > 35\,\mathrm{GeV}$ for the leading photon and $E_{\mathrm{T}} > 25\,\mathrm{GeV}$ for the subleading photon. A further p_{T} selection recommended by the $H\to\gamma\gamma$ analysis [29] is applied to photon candidates with $p_{\mathrm{T}}/m_{\gamma\gamma} > 0.35$ (0.25) for the leading (subleading) photon. Furthermore, the mass range of diphoton mass is required to be between $[105, 160]$ GeV.
- **Number of leptons**: one lepton (muon or electron) for $\gamma\gamma + 1\ell$ analysis and two leptons with opposite charges for $\gamma\gamma + 2\ell$ analysis.
- **Number of jets**: At least two central jets for 1 lepton, and ZZ2l analysis.
- **b-veto**: In order to suppress backgrounds with top quarks, the event is rejected if there is any b-jet. The b-tagger is DL1r with a b-tagging efficiency of 77%.
- **Tight mass window**: The tight mass window ($120\,\mathrm{GeV} < m_{\gamma\gamma} < 130\,\mathrm{GeV}$) is used to define the final signal region which is blinded till the background estimation is consolidated. In the final fit on the background shape of $m_{\gamma\gamma}$ in Section 5, the events both in the window and outside are used.
- **Classification of events**: Events are classified into 4 different categories.
  - **1lepton**: One event with only one lepton and two central jets.
  - **WW1e1m**: One event with two leptons and the flavor of leptons are different.
  - **WW2l**: One event with two same-flavor leptons but failing $|m_{\ell\ell} - m_Z|$<10 GeV.

– **ZZ2l**: One event with two same-flavor leptons where $|m_{\ell\ell} - m_Z|$<10 GeV and two central jets; Events in which Z decays to 2 neutrinos are dropped in this analysis. .

3.2 Selection efficiencies

The efficiencies of signal event selection are visualized in Figure 3 - 5. The exact numbers are listed in Appendix A. These efficiencies are derived from signals of the simulated samples. After the selection of the two photons, the signal efficiencies range from 30.4% to 52.1%, while after the additional selection on the jets and the leptons , the signal efficiencies range from 10% up to 30%, for (X, S) mass grid from (300, 170) to (1000, 500) GeV. These selection efficiencies are consistent with previous studies for $WW^*\gamma\gamma$ analysis [35, 36].

Same selections are applied on SM single Higgs and di-Higgs background samples. Table 7 lists the selection efficiency for each process up to the selection of 2 tight photons, and the efficiency is around 35.0%, which agrees with other diphoton analyses. The event yield after the photon selections are listed in the Table 8 and Table 9 in Section 5.

	ggh	VBF	W^+h	W^-h	$qqZh$	$ggZh$	$t\bar{t}h$	di-Higgs
All Events	100.0	100.0	100.0	100.0	100.0	100.0	100.0	100.0
Pass Trigger	59.9	61.0	55.6	60.4	57.1	67.7	73.5	78.7
2 loose photons	49.8	50.8	43.2	48.1	46.0	56.2	59.1	60.5
Trig Match	49.7	50.7	43.1	48.0	45.9	56.0	58.6	52.8
Tight ID	43.2	43.8	37.0	41.1	39.4	48.1	48.6	48.5
Isolation	38.6	39.6	32.6	36.2	34.7	43.2	40.3	42.3
Rel.Pt cuts	35.8	36.0	29.9	33.1	31.7	39.4	36.7	38.7
$105 < m_{\gamma\gamma} < 160$ GeV	35.8	36.0	29.7	33.0	31.6	39.2	36.3	38.2

Table 7: Selection efficiencies in percent for SM single Higgs and double Higgs processes up to the selection of 2 tight photons.

The contributions from signals, SM Higgs and di-Higgs are estimated with MC statistics. The expected signal yields of resonant X scalar as a function of (m_X, m_S) with the assumption of $\sigma(gg \to X) \times \mathrm{BR}(X \to SH) = 1$ pb are listed in Table 8 and Table 9. Corresponding SM Higgs yields as well as SM di-Higgs contributions with $\sigma(gg \to hh) = 31.05$ fb are listed as well.

Contributions from ggF and VBF processes are negligible due to the requirements on one or two leptons in the selections. SM di-Higgs contributions are effectively suppressed because of its low cross-section and the different kinematics from the signal.

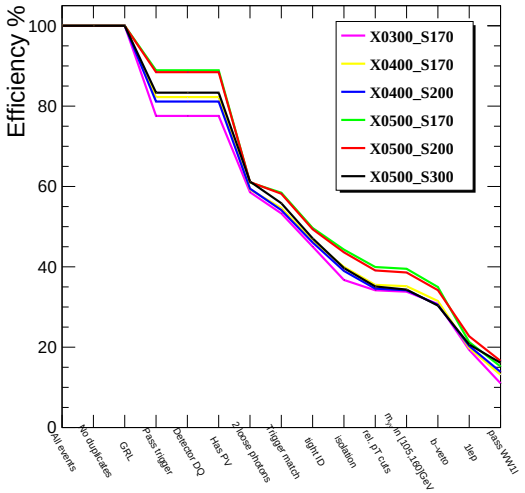

(a) m_X = 300/400/500 GeV

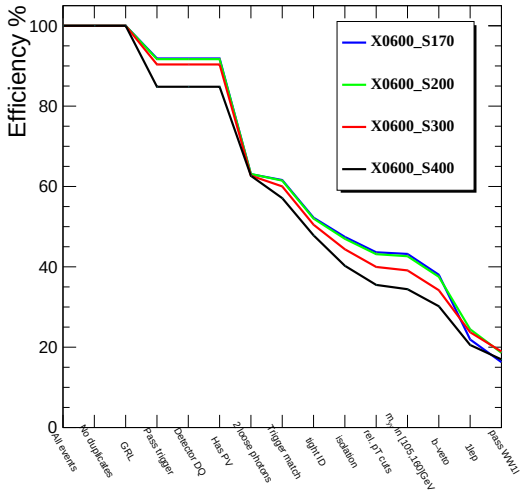

(b) m_X = 600 GeV

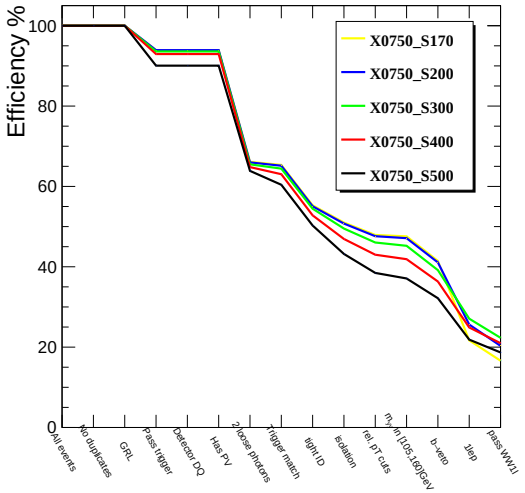

(c) m_X = 750 GeV

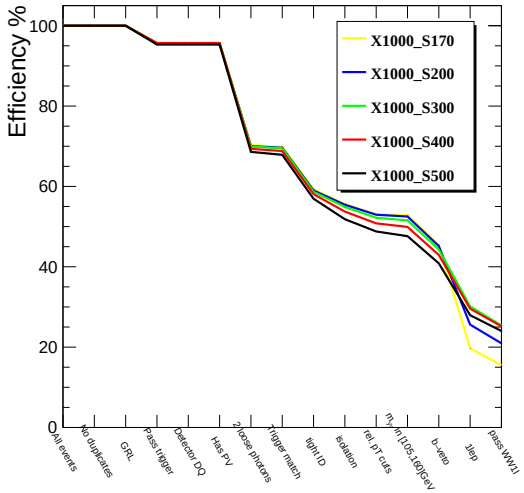

(d) m_X = 1000 GeV

Figure 3: Selection efficiency in WW1l category. All 20 mass points are separated to 4 groups based on m_X.

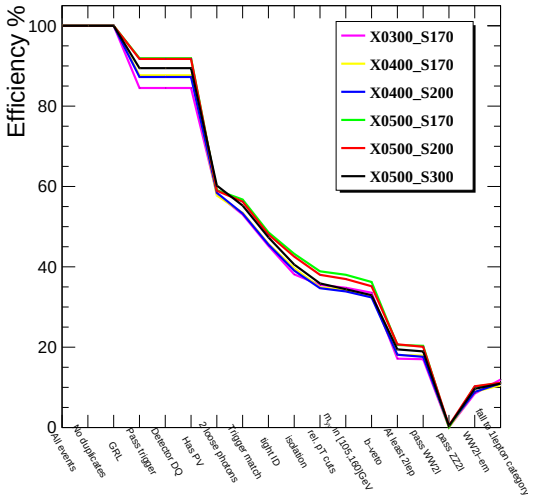

(a) m_X = 300/400/500 GeV

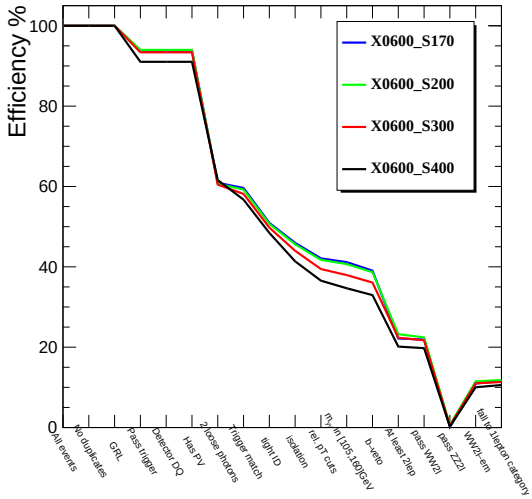

(b) m_X = 600 GeV

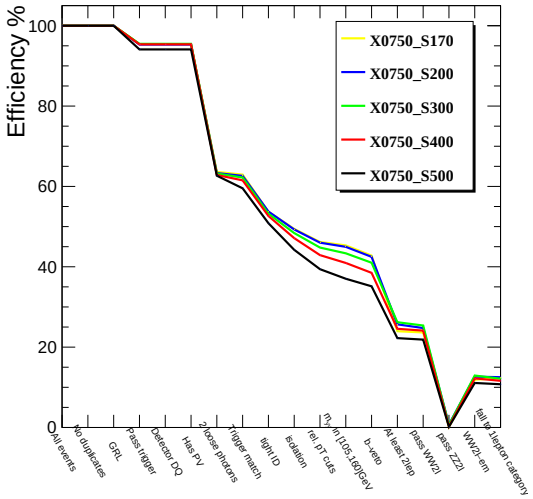

(c) m_X = 750 GeV

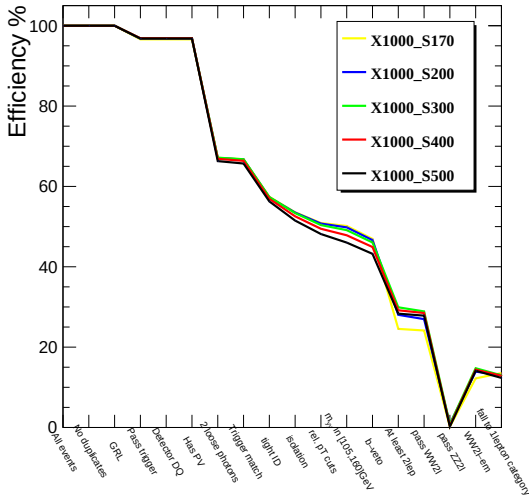

(d) m_X = 1000 GeV

Figure 4: Selection efficiency in WW2l category. All 20 mass points are separated to 4 groups based on m_X.

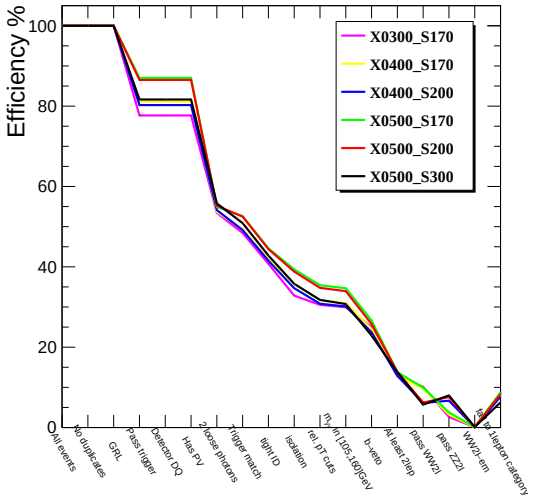

(a) m_X = 300/400/500 GeV

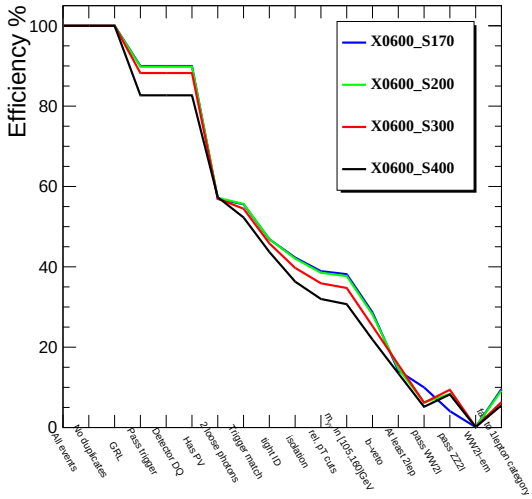

(b) m_X = 600 GeV

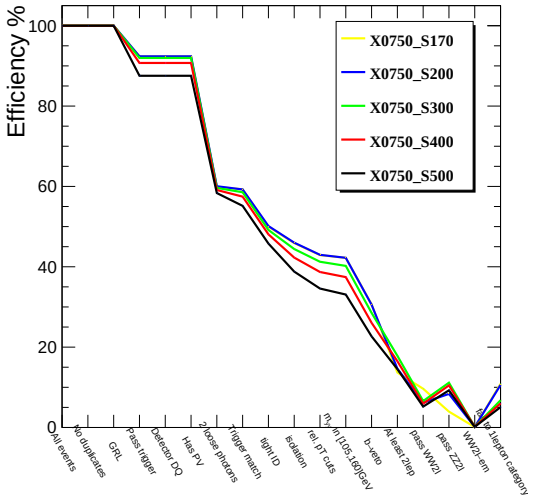

(c) m_X = 750 GeV

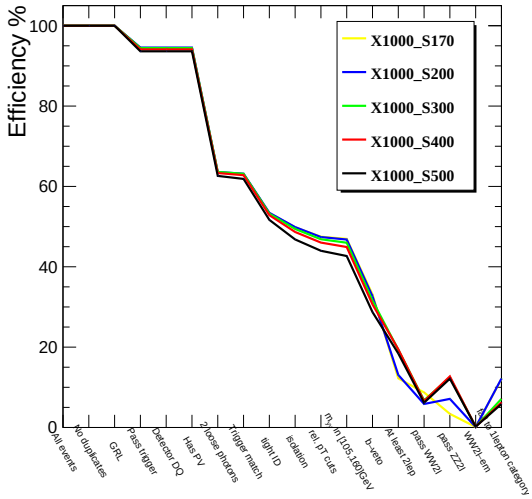

(d) m_X = 1000 GeV

Figure 5: Selection efficiency in ZZ1l category. All 20 mass points are separated to 4 groups based on m_X.

m_X	300	400	500	600	750	1000	400	500	600	750	1000
m_S	170						200				
1 lepton region											
Signals	10.9469	12.0659	13.9792	18.9271	18.0051	17.9718	8.5875	14.3348	15.7590	11.0111	21.7103
ggF	0.0191						0.0134				
VBF	0.0048						0.0046				
VH	0.6836						0.6257				
ttH	0.4410						0.3915				
tH+bbH	0.0770						0.0703				
di-Higgs	0.0948						0.0832				
2 lepton region											
Signals	2.7433	8.9129	4.0167	17.2679	5.2911	4.9245	5.9601	5.3006	5.1519	5.8852	6.2947
ggF	0.0000						0.0000				
VBF	0.0001						0.0000				
VH	0.1493						1.1642				
ttH	0.0822						0.1355				
tH+bbH	0.0087						0.0125				
di-Higgs	0.0427						0.0460				

Table 8: Signal, SM Higgs as well as SM di-Higgs yields. The signal yields correspond to m_S<= 200 GeV assuming the cross section $\sigma(gg \to X) \times \mathrm{BR}(X \to SH)$ of 1 pb, with the integrated luminosity of 139 fb^{-1}. For the SM di-Higgs, $\sigma(gg \to hh)$ = 31.05 fb.

m_X	500	600	750	1000	600	750	1000	750	1000
m_S	300				400, 500				
1 lepton region									
Signals	0.5737	8.0312	32.5921	23.8881	0.5564	10.8044	22.0978	4.5707	23.4183
ggF	0.0049				0.0042				
VBF	0.0015				0.0009				
VH	0.4077				0.3194				
ttH	0.2597				0.1926				
tH+bbH	0.0400				0.0296				
di-Higgs	0.0445				0.0314				
WW 2 lepton region									
Signals	4.0596	7.7640	6.2101	7.5156	2.3114	4.6149	6.1617	3.6571	5.8629
ggF	0.0000				0.0000				
VBF	0.0000				0.0000				
VH	0.6371				0.1100				
ttH	0.1241				0.0903				
tH+bbH	0.0123				0.0090				
di-Higgs	0.0301				0.0152				

Table 9: Signal, SM Higgs as well as SM di-Higgs yields. The Signal yields correspond to m_S>= 300 GeV assuming the cross section $\sigma(gg \to X) \times \mathrm{BR}(X \to SH)$ of 1 pb, with the integrated luminosity of 139 fb^{-1}. For the SM di-Higgs, $\sigma(gg \to hh)$ = 31.05 fb.

4 BDT optimization for the analysis

Reconstruction of physics objects and the optimizations of the event selections are discussed in this section.

Various optimization strategies are used for different channels, as shown in Table 10. For WW1l and WW2l channels, a Boosted Decision Tree (BDT) is employed to reach better performances; While for WW1e1m and ZZ2l channels, events are directly counted after straightforward selections due to the low statistics and high signal-over-background ratios.

For the two channels using BDT, multiple discriminating variables separating signal and background are chosen as inputs for the BDT training. The BDT output, which reflects an optimal combination of these input variables to separate signal and background, is used to define the signal regions to have a good significance. Such signal regions are defined according to the expected significance as described in Eq.(4) and the procedure is mentioned in Section 4.2. When doing the optimization, the cross sections for signals is assumed to be 1 pb as mentioned in the Section 1. To blind the signal region, which is defined as the mass window $m_{\gamma\gamma} \in (120, 130)$GeV, the sideband data is used to estimate the yields for the continuum background in the signal region.

Channel	Definition	Optimization strategy
WW1l	1lepton, 2 central jets	BDT
WW2l	2lepton, same flavor, $\|m_{\ell\ell} - m_Z\|$>10GeV	BDT
WW1e1m	1 electron 1 muon	Cut based
ZZ2l	2lepton, 2 central jets, same flavor, $\|m_{\ell\ell} - m_Z\|$<10GeV	Cut based

Table 10: Definition of the four channels and the corresponding optimization strategies.

4.1 BDT training and testing

The Toolkit for Multi-Variant Data Analysis (`TMVA`) package [37] is used to perform the BDT training. The training is applied on the partial amount of the events (called training sample) and the results are tested and evaluated with the remaining events (called test sample). Events with odd and even numbers are grouped to the training and test samples respectively, in order to avoid possible biases. Moreover, the Cross Validation method[38] is applied with 4 folds to improve the performance. As the events are split by the event ID, it is possible to trace the corresponding fold for each training event.

4.1.1 Input variables

The major production and decay process for SH signal in this study is $X \to SH, H \to \gamma\gamma$ and $S \to W^+W^-$. In the WW1l channel, one W boson decays leptonically ($W \to l\nu$) and the other goes with hadronic decay ($W \to q\bar{q}$). While in the WW2l channel, both 2 W bosons have to decay leptonically. Several kinematic variables regarding different objects can be constructed as listed respectively in Table 11 and Table 12 for WW1l and WW2l channels.

Variable	Definition	Separation
Regarding particle X		
$\Delta R(\gamma\gamma, l\nu jj)$	Angular difference between diphoton system (H) and $l\nu jj$ system (S)	0.048
Regarding particle S		
$\Delta R(jj, l\nu)$	Angular difference between dijet system (W_{had}) and $l\nu$ system (W_{lep})	0.089
$p_T^{l\nu jj}$	Transverse momentum of $l\nu jj$ system (S)	0.373
Regarding SM Higgs boson		
$p_T^{\gamma\gamma}$	Transverse momentum of diphoton system (H)	0.484
$\Delta\Phi(\gamma\gamma, l)$	Polar angle difference between di-photon system (H) and signal lepton	0.026
Regarding single W boson from S		
$\Delta R(j, j)$	Angular difference between two jets (W_{had})	0.171
p_T^{jj}	Transverse momentum of di-jet system (W_{had})	0.181
$m_{jj}(m_W)$	Invariant mass of di-jet system whose mass is closest to m_W (W_{had})	0.119
$\Delta R(l, E_{\mathrm{T}}^{\mathrm{miss}})$	Angular difference between lepton and $E_{\mathrm{T}}^{\mathrm{miss}}$ (W_{lep})	0.108
$E_{\mathrm{T}}^{\mathrm{miss}}$	Missing transverse momentum	0.248
p_T^l	Transverse momentum of the single lepton	0.203
$m_T(l\nu)$	Transverse mass of $l + E_{\mathrm{T}}^{\mathrm{miss}}$ system (W_{lep})	0.044

Table 11: Variables used for BDT training in WW1l channel and their separation powers.

Variable	Definition	Separation
Regarding particle X		
$\Delta R(\gamma\gamma, ll + E_{\mathrm{T}}^{\mathrm{miss}})$	Angular difference between diphoton system (H) and $ll + E_{\mathrm{T}}^{\mathrm{miss}}$ system (S)	0.031
Regarding particle S		
$\Delta R(l_1 + E_{\mathrm{T}}^{\mathrm{miss}}, l_2)$	Angular difference between leading lepton + $E_{\mathrm{T}}^{\mathrm{miss}}$ (W_{l1}) and l_2	0.038
Regarding SM Higgs boson		
$p_T^{\gamma\gamma}$	Transverse momentum of diphoton system (H)	0.621
$\Delta\Phi(\gamma\gamma, l_1)$	Polar angle difference between di-photon system (H) and the leading lepton	0.079
Regarding single W boson from S		
$p_T^{l_1}$	Transverse momentum of the leading lepton	0.415
$E_{\mathrm{T}}^{\mathrm{miss}}$	Missing transverse momentum	0.638
$p_T^{l_1+E_{\mathrm{T}}^{\mathrm{miss}}}$	Transverse momentum of the leading lepton and $E_{\mathrm{T}}^{\mathrm{miss}}$ system	0.533
$m_T(l_1 + E_{\mathrm{T}}^{\mathrm{miss}})$	Transverse mass of leading lepton and $E_{\mathrm{T}}^{\mathrm{miss}}$ system	0.362
m_{ll}	Invariant mass of di-lepton system	0.358

Table 12: Variables used for BDT training in WW2l channel and their separation powers.

To simplify the training processes in 20 mass hypotheses of X and S, a parameterized BDT method [39] is applied in this analysis. This method targets the classification tasks with uncertain parameters in the training sample, e.g. the hypothesis of new particle mass m_X. These parameters are given to the classifier as the extension of input event-level features. The machine-learning algorithm is expected to learn from these parameters, thus the trained can have good performance by specifying the parameter in different cases. Considering the BDT may not have smooth interpolation for several unknown parameters in this method, m_X is treated as the only input parameter and signal processes are assigned to 4 groups with m_S: $m_S = 170$ GeV, $m_S = 200$ GeV, $m_S = 300$ GeV, and $m_S \geq 400$ GeV. This procedure is performed in both WW1l and WW2l channels, so in total 8 different BDTs are trained.

In each channel, the SH processes are treated as the signal during the BDT training, with the input variables described above and the truth m_X as a parameter. The background training samples includes all processes described in Section 1.2.2. To ensure a better agreement between the data and MC, the continuum backgrounds (Sherpa $\gamma\gamma + jets$, $V\gamma\gamma$ and $t\bar{t}\gamma\gamma$) are reweighted to the sideband data as a function of the transverse mass of leptonic decayed W boson m_T^{W1}. Before this procedure, an individual normalization factor based on the data and MC ratio is implemented on the MC for each channel. The distribution before and after reweighting is shown in Figure 6. Decent consistencies between sideband data and continuum MC for the disbributions of the discriminating variables can be reached with this method. Appendix C describes the method in detail and presents the comparisons of the other distributions for the kinematic variables before and after the reweighting.

The parameter m_X for the training background sample is randomly assigned with the corresponding signal mass points in each m_S group. While this number is assigned to the signal hypothesis when applying the trained results. Hyperparameters used in the training are summarized in Table 13.

Parameters	Value
`BoostType`	AdaBoost
`AdaBoostBeta`	0.5
`NTrees`	850
`MinNodeSize`	2.5%
`UseBaggedBoost`	True
`BaggedSampleFraction`	0.5
`SeparationType`	GiniIndex
`nCuts`	20
`MaxDepth`	3
`NegWeightTreatment`	Ignore
`UseCrossValidation`	True
`Nums of Folds`	4

Table 13: Summary of hyper-parameters used in BDT training.

The distributions of input variables after the tuning used in WW1l channels for signals, backgrounds and sideband data, are shown in Figure 7 - 9 with corresponding signal mass $(m_X, m_S) = (1000, 500)$ GeV. To easily compare the shape, the scales of the signals are renormalized to the same as the background. Reasonable consistencies between sideband data and MC for the discriminating variables are observed. The corresponding distributions of the input variables for WW2l channels are shown in Figure 10 - 11.

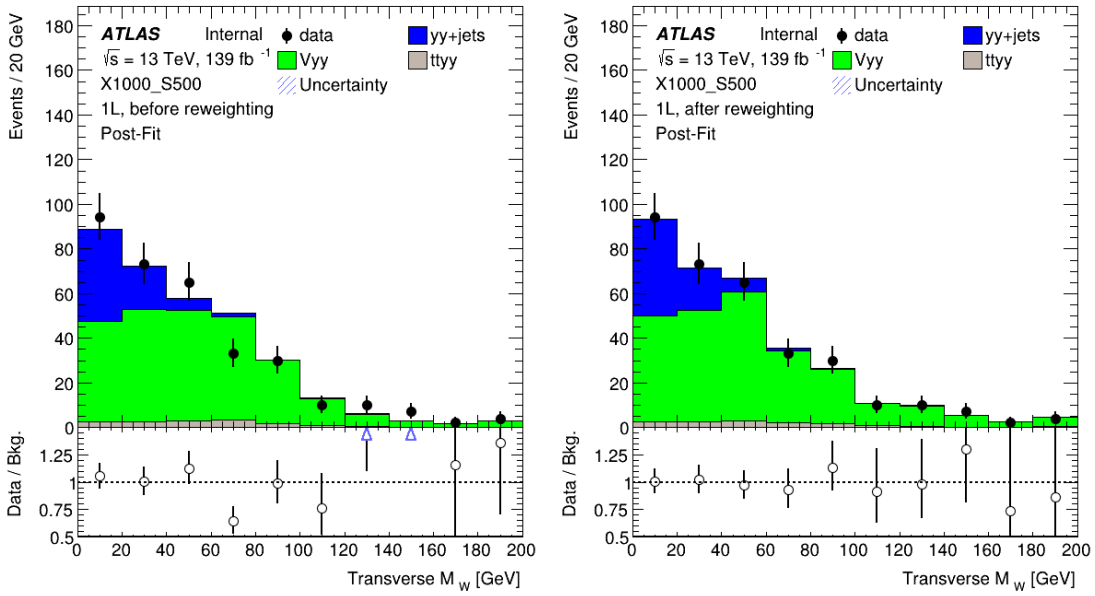

(a) (b)

Figure 6: m_T^{W1} distribution for $\gamma\gamma + jets$, $V\gamma\gamma$ and $t\bar{t}\gamma\gamma$ processes and the sideband data before(a) and after(b) background reweighting. The relative ratio between the 3 MC processes is fixed to the SM prediction.

The correlation matrix between input variables along with $m_{\gamma\gamma}$ are shown in Figure 12 and 13. Relevant plots for the other mass points are displayed in Appendix D.

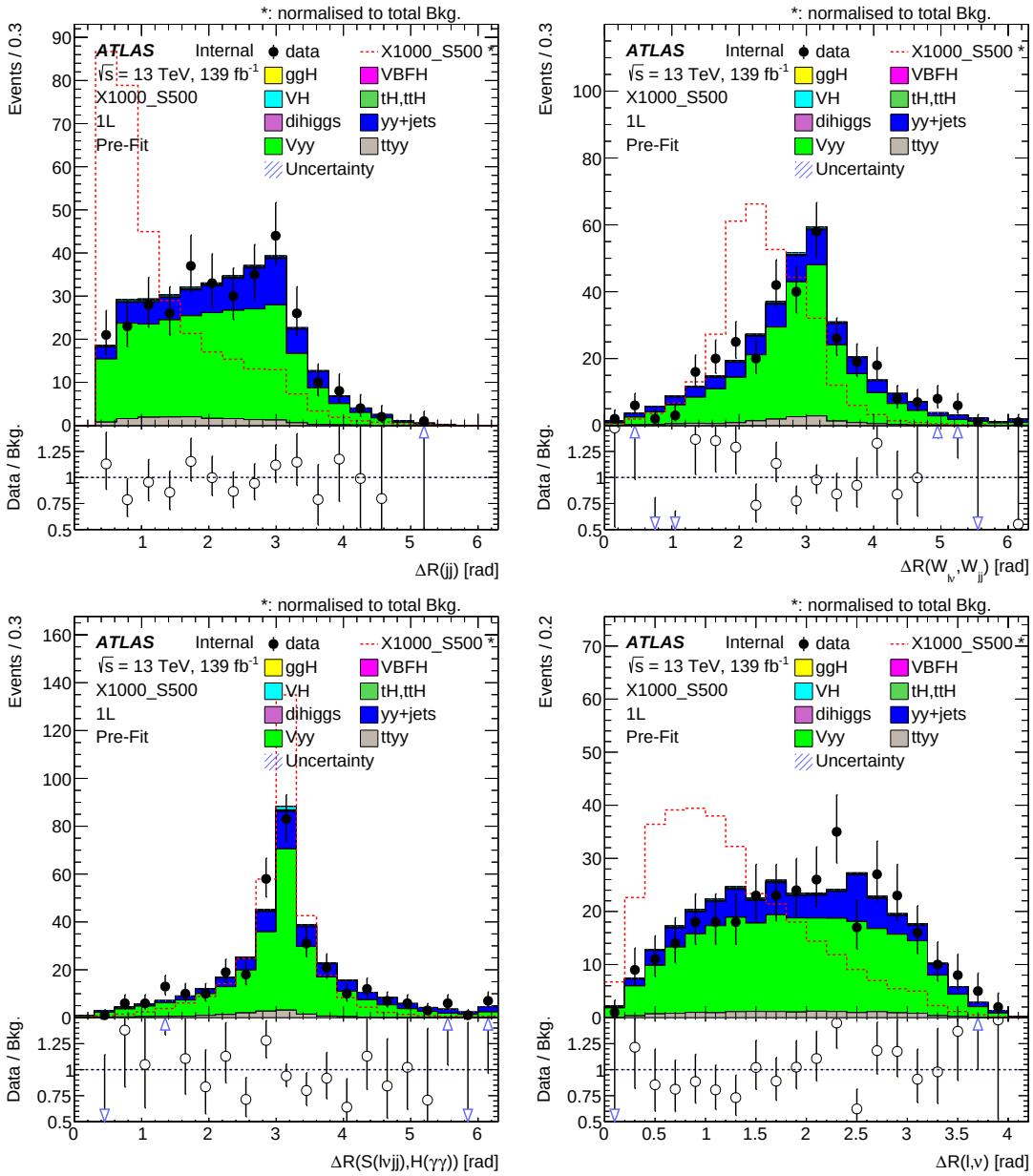

Figure 7: $\Delta R(j,j)$, $\Delta R(W1,W2))$, $\Delta R(S,H)$, $\Delta R(\ell,\nu))$ distributions for the WW1l channel. The events of the continuum MC and data are from the sideband region. For the single Higgs, dihiggs and signal samples, events are from the mass window between 120 and 130 GeV.

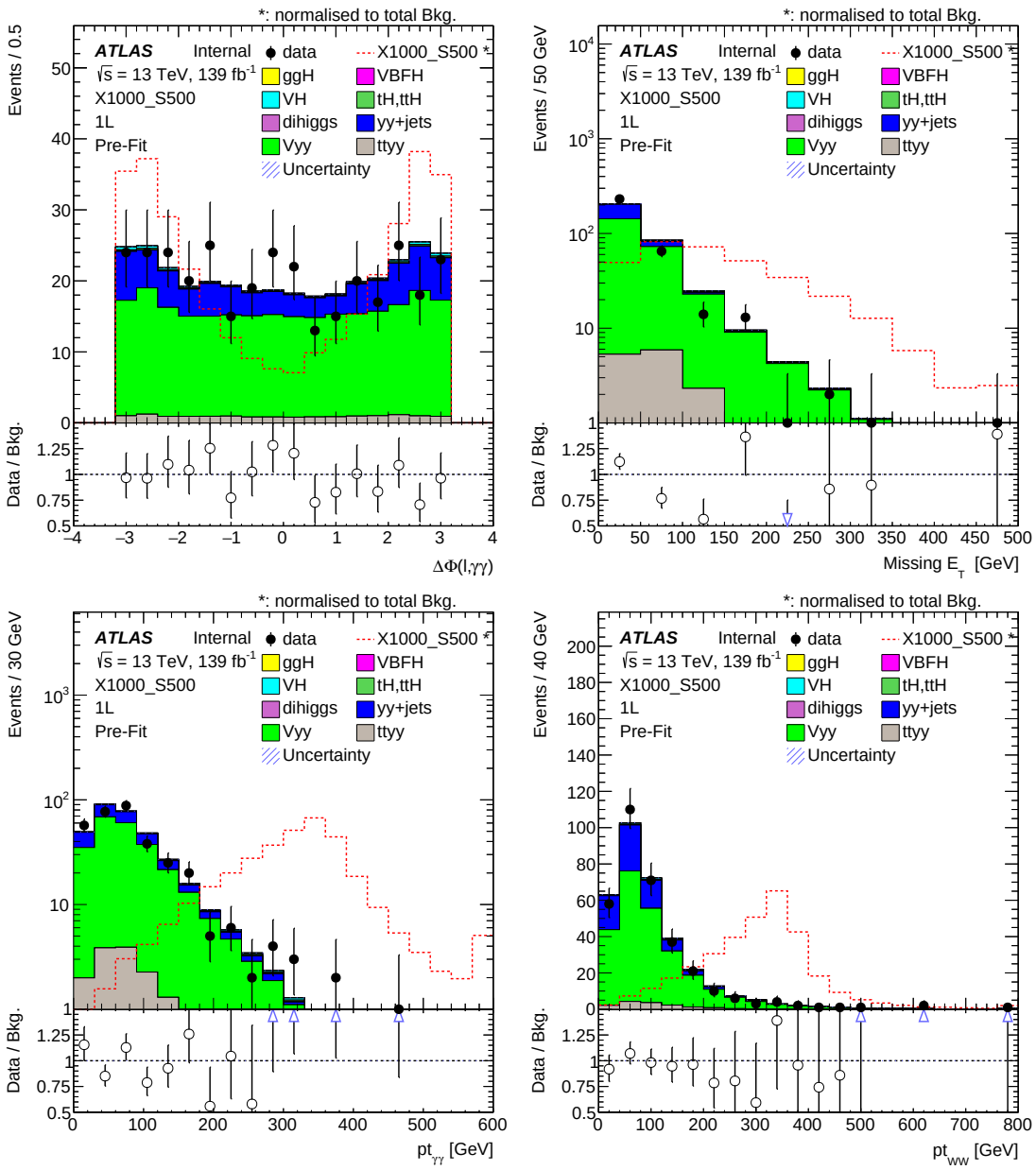

Figure 8: $\Delta\Phi(\gamma\gamma, \ell_1)$, $E_{\mathrm{T}}^{\mathrm{miss}}$, $p_{\mathrm{T}}(\gamma\gamma)$ and $p_{\mathrm{T}}(WW)$ distributions for the WW1l channel. The events of the continuum MC and data are from the sideband region. For the single Higgs, dihiggs and signal samples, events are from the mass window between 120 and 130 GeV.

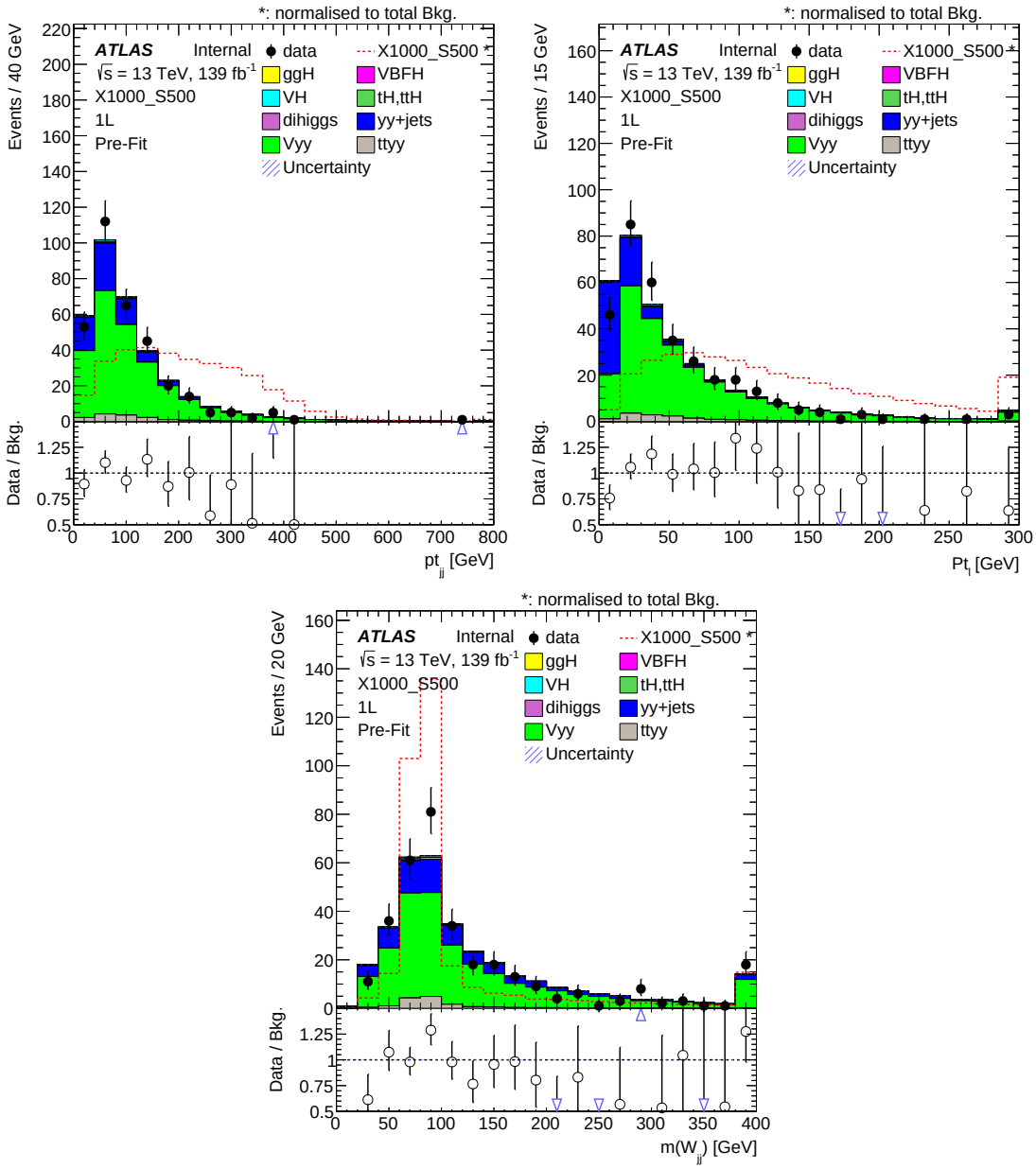

Figure 9: $p_{\mathrm{T}}(jj)$, $p_{\mathrm{T}}(\ell 1)$ and $M_{W(jj)}$ and distributions for the WW1l channel. The events of the continuum MC and data are from the sideband region. For the single Higgs, dihiggs and signal samples, events are from the mass window between 120 and 130 GeV.

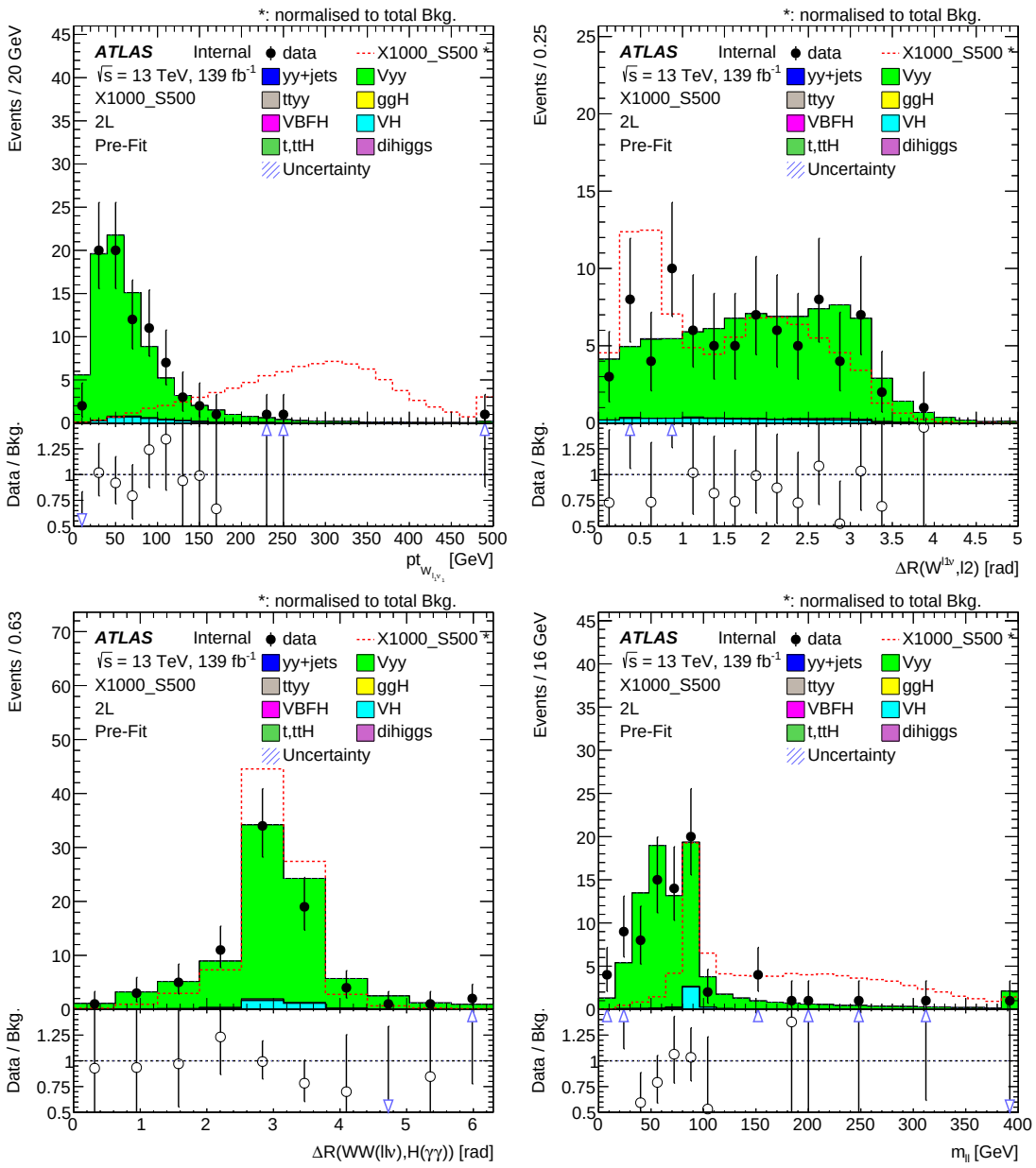

Figure 10: $p_{\mathrm{T}}(\ell\nu)$, $\Delta R(W1, W2))$, $\Delta R(S, H)$, m_{ll} distributions for the WW2l channel. The events of the continuum MC and data are from the sideband region. For the single Higgs, dihiggs and signal samples, events are from the mass window between 120 and 130 GeV.

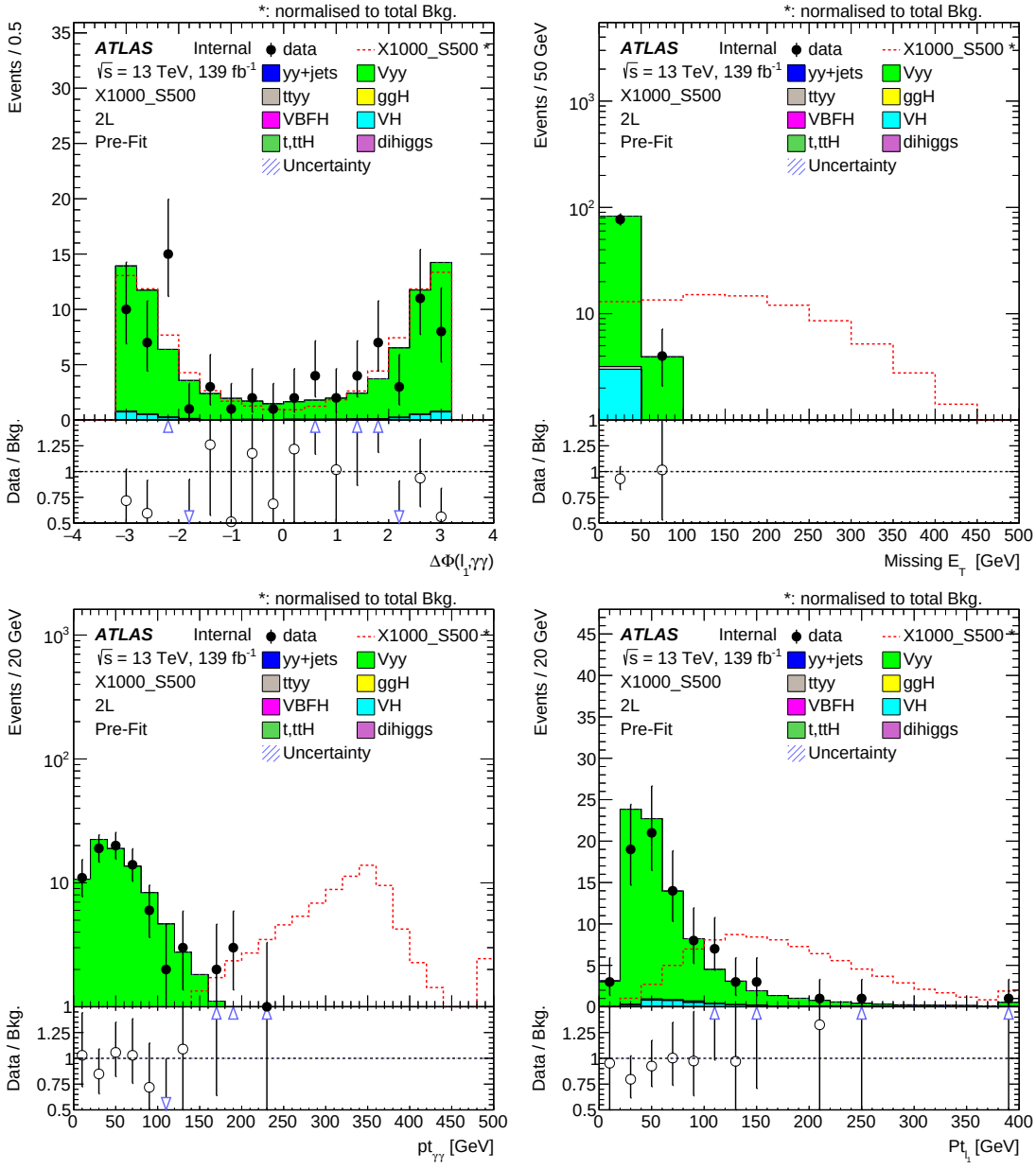

Figure 11: $\Delta\Phi(\gamma\gamma, \ell_1)$, $E_{\mathrm{T}}^{\mathrm{miss}}$, $p_{\mathrm{T}}(\gamma\gamma)$ and $p_{\mathrm{T}}(\ell 1)$ distributions for the WW2l channel. For the continuum MC and data events, are from the sideband region. For the single Higgs, dihiggs and signal samples, are in the mass window.

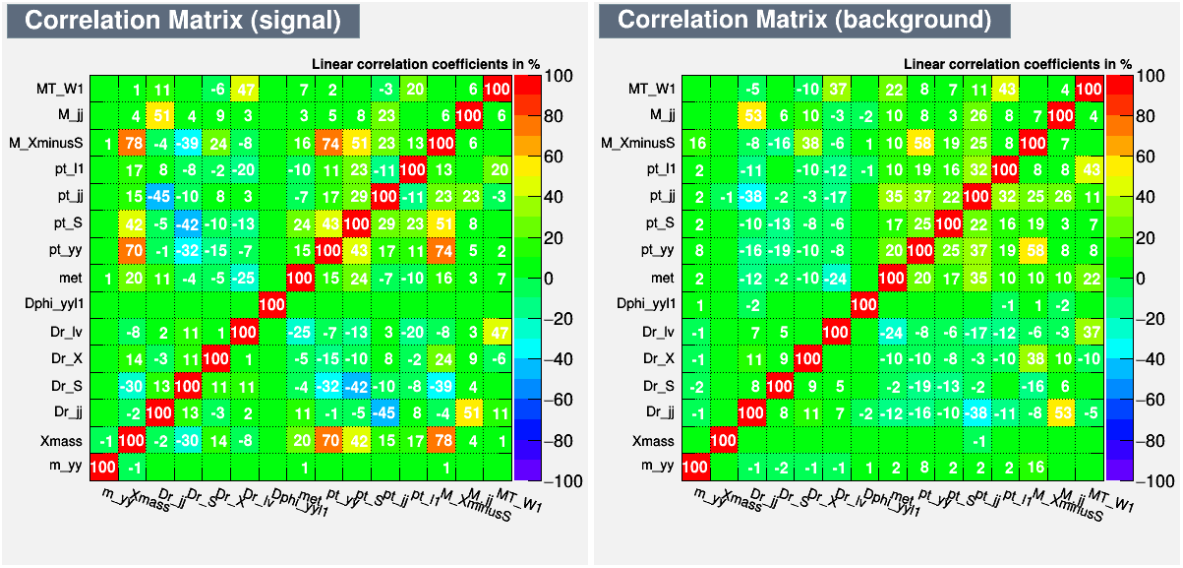

(a) (b)

Figure 12: Linear correlation matrix between input variables and $m_{\gamma\gamma}$ for signal $(m_X, m_S) = (1000, 500)$ GeV and background in the WW1l channel.

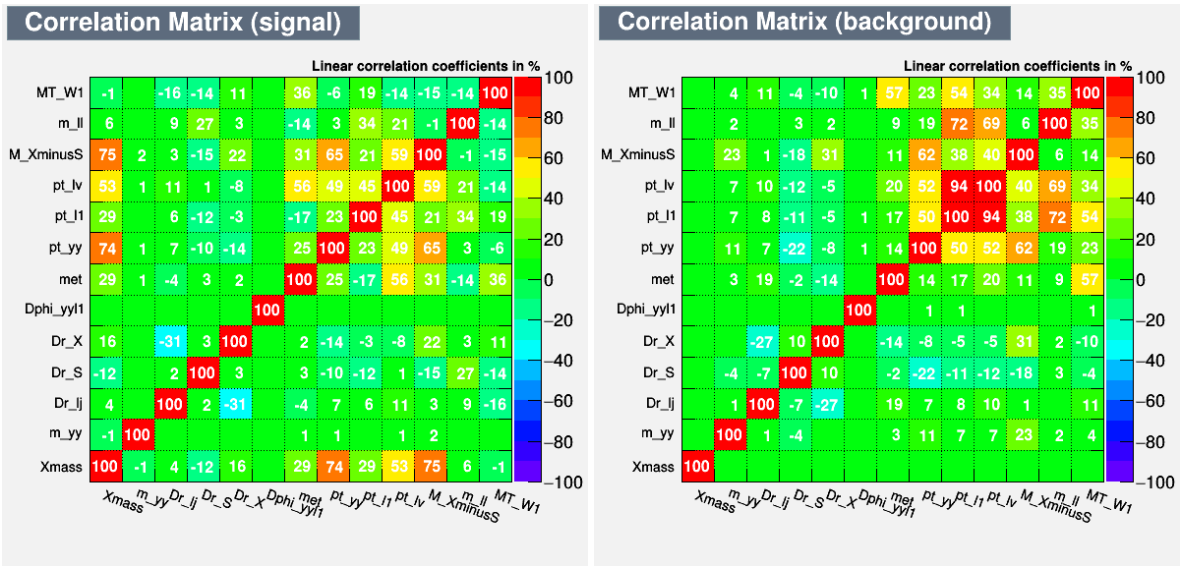

(a) (b)

Figure 13: Linear correlation matrix between input variables and $m_{\gamma\gamma}$ for signal $(m_X, m_S) = (1000, 500)$ GeV and background in the WW2l channel.

4.1.2 Training results

Figure 14 presents the BDT training result and the agreement between training and test samples in 4 folds in the WW1l channel. Figure 15 shows the signal efficiency vs background rejection curve. Considering the low correlation between input variables and $m_{\gamma\gamma}$, the BDT outputs are naturally thought to be independent of $m_{\gamma\gamma}$, which is further demonstrated in Table 16.

Similar information for WW2l channels is shown in Figure 16 and 17. For both 1l and 2l cases, The linear correlation factors are checked to be about 1% for signal and 5% for MC and data sideband events. The variable importance in these 2 BDTs are listed in Table 14 and 15.

Figure 18 shows the trained BDT response for all processes and sideband data with $m_S = 500$ GeV hypothesis in two categories. The agreement of the BDT distribution between sideband data and MC is reasonable considering the complex phase space in this process, the known imperfect description in MC and the limited statistics in sideband data.

Ranking	Variable	Importance
1	$p_T^{\gamma\gamma}$	0.1017
2	$m_{all} - m_{l\nu jj}$	0.0936
3	p_T^{l}	0.0741
4	$E_{\mathrm{T}}^{\mathrm{miss}}$	0.0732
5	$\Delta R(j, j)$	0.0727
6	$\Delta\Phi(\gamma\gamma, l)$	0.0726
7	$\Delta R(l, E_{\mathrm{T}}^{\mathrm{miss}})$	0.0704
8	$\Delta R(jj, l\nu)$	0.0674
9	m_{jj}	0.0633
10	$DeltaR(\gamma\gamma, l\nu jj)$	0.0616
11	p_T^{jj}	0.0594
12	$m_T\,(l\nu)$	0.0529
13	$p_T^{l\nu jj}$	0.0421

Table 14: Variable importance in WW1l BDT.

Ranking	Variable	Importance
1	$p_T^{\gamma\gamma}$	0.1077
2	$E_{\mathrm{T}}^{\mathrm{miss}}$	0.1038
3	$\Delta\Phi(\gamma\gamma, l_1)$	0.0939
4	$m_{all} - m_{ll+E_{\mathrm{T}}^{\mathrm{miss}}}$	0.0929
5	$\Delta R(l1, l2)$	0.0885
6	m_{ll}	0.0874
7	$\Delta R(\gamma\gamma, ll + E_{\mathrm{T}}^{\mathrm{miss}})$	0.0782
8	$p_T^{l+E_{\mathrm{T}}^{\mathrm{miss}}}$	0.0739
9	$p_T^{l_1}$	0.0686
10	$m_T\,(l_1 + E_{\mathrm{T}}^{\mathrm{miss}})$	0.0609

Table 15: Variable importance in WW2l BDT.

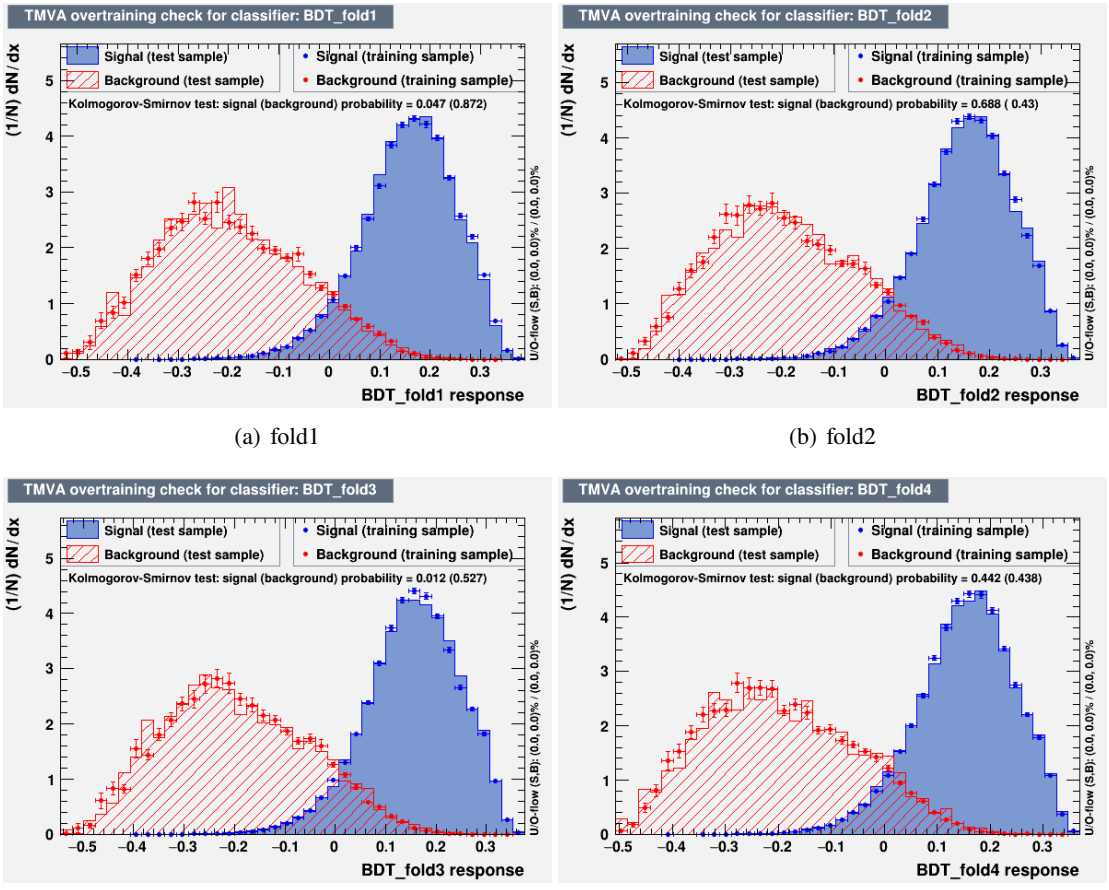

(a) fold1 (b) fold2

(c) fold3 (d) fold4

Figure 14: The overtraining plots with ks test values for 4 individual folds in 1 lepton $m_S \geq 400$ GeV group.

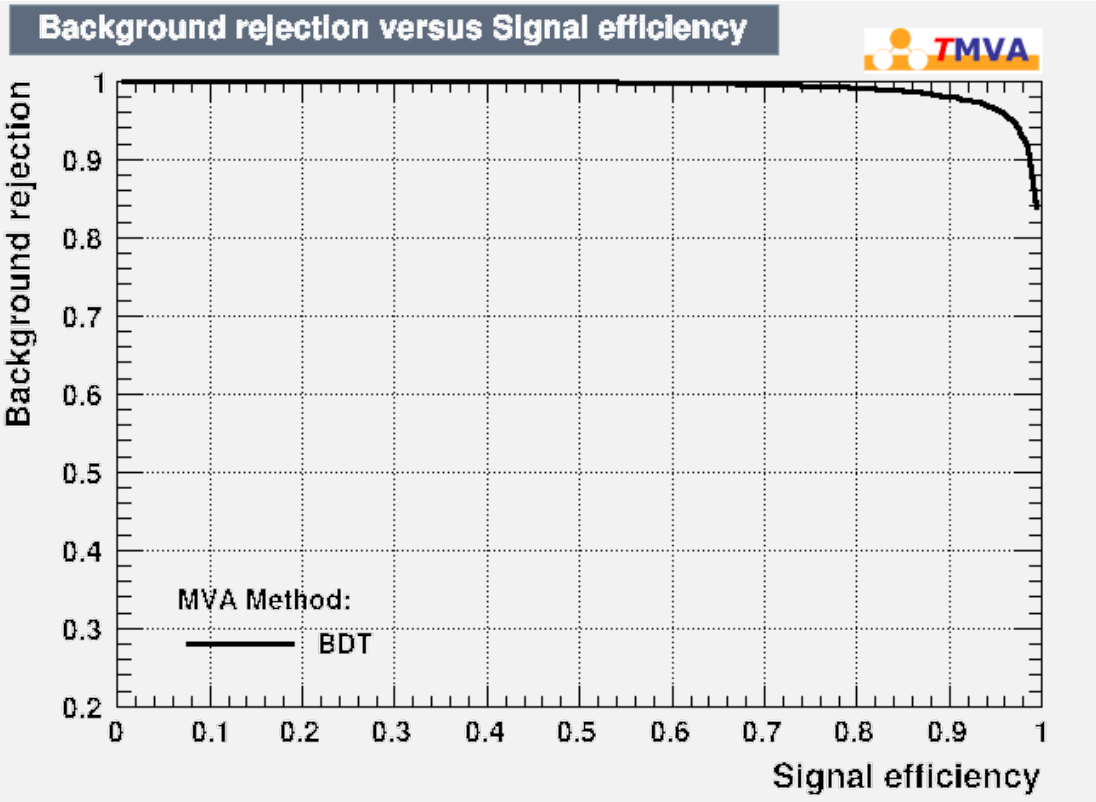

Figure 15: The signal efficiency vs background rejection curve (ROC curve) in WW1l channel for $m_S \geq 400$ GeV group.

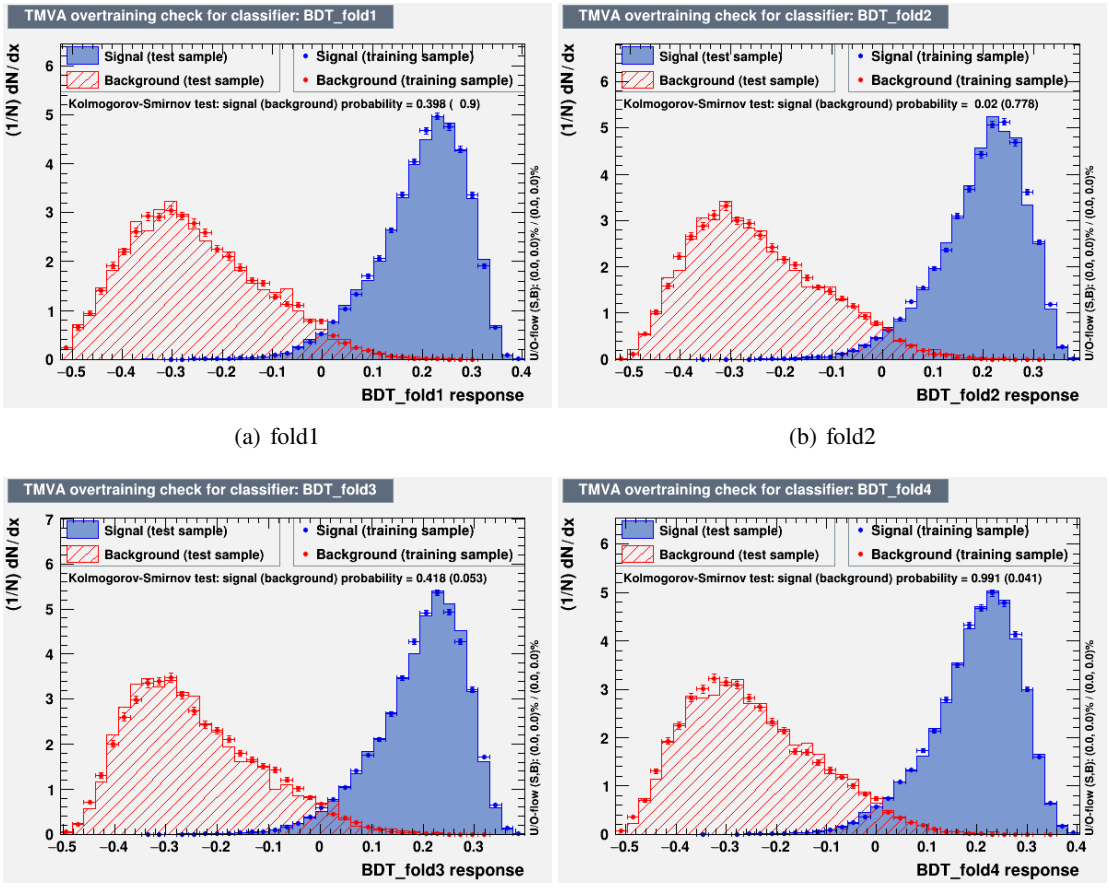

(a) fold1 (b) fold2

(c) fold3 (d) fold4

Figure 16: The overtraining plots with ks test values for 4 individual folds in 2 leptons $m_S \geq 400$ GeV group.

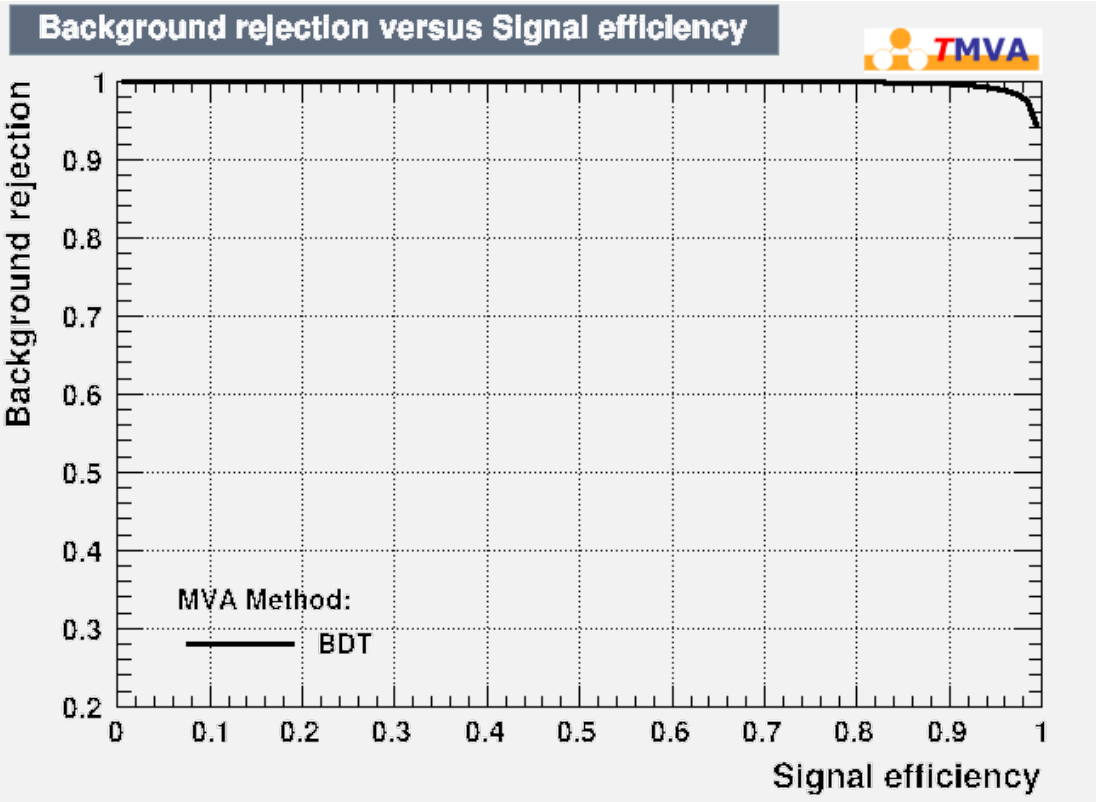

Figure 17: The signal efficiency vs background rejection curve (ROC curve) in WW2l channel for $m_S \geq 400$ GeV group.

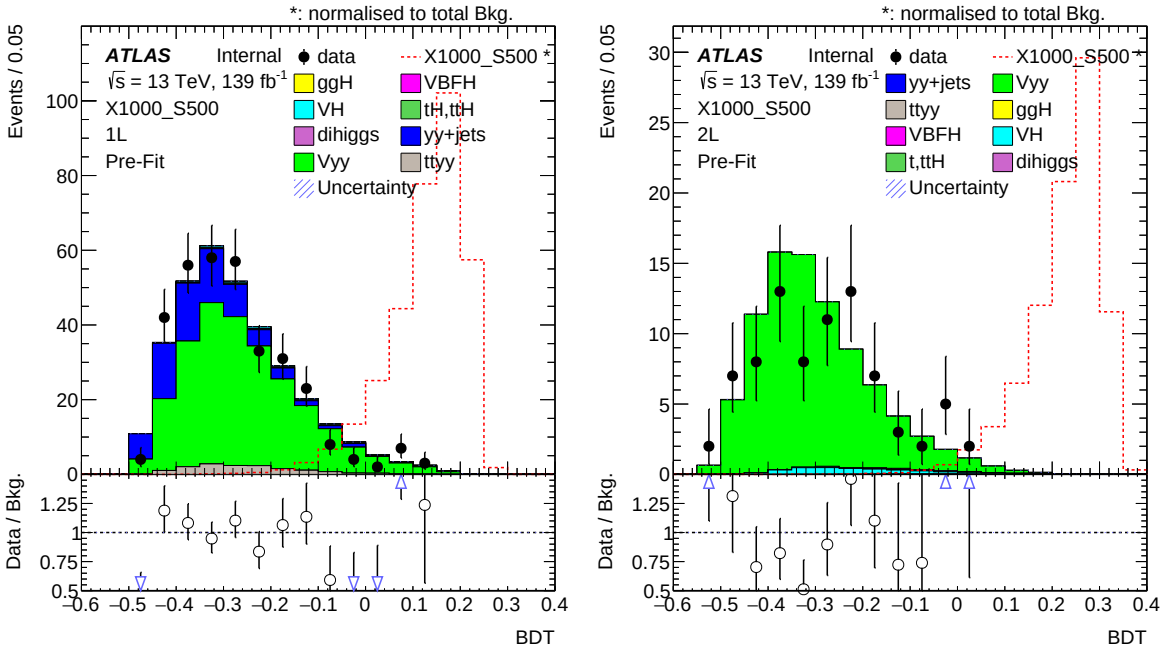

Figure 18: BDT outputs for WW1l and WW2l channels for signal, background MC and sideband data..

1l	data	signal	2l	data	signal
X1000_S170	-6.08%	-0.24%	X1000_S170	-7.27%	-0.74%
X1000_S200	0.66%	-0.40%	X1000_S200	3.90%	0.87%
X1000_S300	-0.31%	0.55%	X1000_S300	1.82%	1.62%
X1000_S400	3.95%	0.83%	X1000_S400	4.88%	2.22%
X1000_S500	3.55%	-0.57%	X1000_S500	4.32%	2.59%
X0300_S170	2.22%	-0.97%	X0300_S170	-0.22%	-1.70%
X0400_S170	5.44%	1.03%	X0400_S170	4.50%	3.59%
X0400_S200	5.46%	0.08%	X0400_S200	4.17%	4.79%
X0500_S170	5.93%	0.20%	X0500_S170	0.59%	1.25%
X0500_S200	2.57%	-0.82%	X0500_S200	-3.54%	0.75%
X0500_S300	6.40%	1.91%	X0500_S300	4.17%	4.65%
X0600_S170	6.11%	0.41%	X0600_S170	4.02%	4.19%
X0600_S200	8.06%	0.16%	X0600_S200	0.91%	1.92%
X0600_S300	6.66%	-0.12%	X0600_S300	-2.77%	0.81%
X0600_S400	6.66%	-0.12%	X0600_S400	-2.77%	0.81%
X0750_S170	7.19%	1.52%	X0750_S170	4.29%	3.07%
X0750_S200	6.41%	1.93%	X0750_S200	3.94%	3.32%
X0750_S300	8.64%	2.00%	X0750_S300	0.72%	2.46%
X0750_S400	9.13%	-0.09%	X0750_S400	-3.01%	1.10%
X0750_S500	9.13%	-0.09%	X0750_S500	-3.01%	1.10%

Table 16: The correlation between BDT output value and diphoton mass, for signal and data sideband events.

4.2 Optimization of the analysis with BDT output

Figure 18 shows the BDT output distributions for the signal with mass (m_X, m_S)=(1000,500) GeV, background and sideband data. Based on this, events are categorized into two regions, namely loose and tight, by optimizing the signal significance:

$$Z = \sqrt{2 \times [(S+B) \times (\ln \frac{S+B}{B}) - S]} \tag{4}$$

where S is the signal yield and B is the background yield in each category.

For WW1l and WW2l channels, BDT thresholds dividing events into loose and tight regions are obtained by scanning the BDT cut value to reach the highest Z in the combined BDT category significance. Specifically, the scan is done with a step size 0.005 and the maximization of $Z_{combined} = \sqrt{Z_{tight}^2 + Z_{loose}^2}$ is chosen. Moreover, for the WW2l channel, the tight region requires at least 1 sideband data event left for the convenience to apply background estimation. The two categories are named with `WW1l_Tight` (`WW2l_Tight`) and `WW1l_Loose` (`WW2l_Loose`). The individual threshold on BDT determined for signals with different masses is summarized in Table 17.

X Mass [GeV]	S Mass [GeV]	WW1L BDT Cut	WW2L BDT Cut
300	170	0.09	0.155
400	170	0.08	0.145
400	200	0.03	0.13
500	170	0.125	0.165
500	200	0.095	0.14
500	300	0.025	0.115
600	170	0.16	0.115
600	200	0.115	0.085
600	300	0.045	0.11
600	400	0.035	0.1
750	170	0.21	0.03
750	200	0.155	0.035
750	300	0.11	0.06
750	400	0.085	0.11
750	500	0.035	0.11
1000	170	0.185	-0.01
1000	200	0.195	-0.04
1000	300	0.165	0.005
1000	400	0.125	0.04
1000	500	0.125	0.04

Table 17: BDT thresholds to divide events into tight and loose regions, concerning the signals with different mass points

5 Signal and background estimations

In this analysis, the statistical result is obtained from a binned signal + background fit $m_{\gamma\gamma}$ distribution in data. The shape of the SH signal is derived from MC simulation, analytical function is not used to describe the signal for this binned model. The continuum $\gamma\gamma$ background is modeled using data in 0ℓ control region for 1-lepton region and 2-lepton region, following the strategy of previous $X \to hh \to WW\gamma\gamma$ analysis with 36 fb^{-1} data in ATLAS[35]. An analytical function is fitted to side band data, and the choice of the function form is determined from so-called spurious signal approach.

5.1 Models of signals, SM Higgs and SM Higgs pair backgrounds

5.2 Continuum background estimation

The continuum background is expected to be a smoothly falling shape that can be modeled with an analytical function. So this background yield under the signal peak can be modeled with a functional form that is largely constrained by the mass sidebands. Due to the low statistics of sideband data with 1/2 leptons in the final state, the function is determined using the $m_{\gamma\gamma}$ shape in 0 lepton + jets control region data. The difference is covered by one systematic uncertainty term which is derived from MC discussed in Section 6.2.2. This strategy was used in previous analysis[35]. Two different kinds of control regions are adapted based on the phase space of different channels. The control region for the 1-lepton case (WW1l channel) is defined as $\gamma\gamma + 0l + 1j$. And the control region for the 2-lepton case (WW2l, ZZ2l, $WWe\mu$) is defined as $\gamma\gamma + 0l + \geq 2j$. In Section 4 the BDT is constructed independently with $m_{\gamma\gamma}$, so different BDT categories, no matter tight/loose, 1-lepton/2-lepton categories, share the common background modeling of $m_{\gamma\gamma}$, which is estimated from 0-lepton control region.

The analytical function used to describe the model is chosen from the spurious signal test. The following functions are considered in the exercise:

- Exponential: $e^{c\cdot m_{\gamma\gamma}}$
- Exponential of 2^{nd} Order Polynomial: format as $e^{c_1\cdot m_{\gamma\gamma}^2 + c_2\cdot m_{\gamma\gamma}}$
- Chebyshev polynomial of order N: N=1-5.

In 1-lepton channel, the continuum background distribution from the CR 0l+1j sideband data, is fitted with different functions and shown in Figure 19.

The main criterion used to select the functional form in each category is a bias test performed by fitting the control region data using a model with free parameters for both the signal and background event yields. The potential bias due to the mis-modeling of the background $m_{\gamma\gamma}$ distribution is estimated from the fitted signal yield, i.e. the spurious signal. In the spurious signal test, the cross-section of the signal process is fixed to the expected upper limit with 95% CL instead of the initial one, namely 1 pb. The absolute value of the fitted signal yield $|S_{spur}|$ is considered the potential bias. The function with the $|S_{spur}|$ satisfying at least one of the following conditions is considered acceptable, which is called the relaxed template:

- $S_{spur} < 10\% N_{s,exp}$ where $N_{s,exp}$ is the expected number of signal yields in that category ($\mu_{sp} = S_{spur}/N_{s,exp}$),

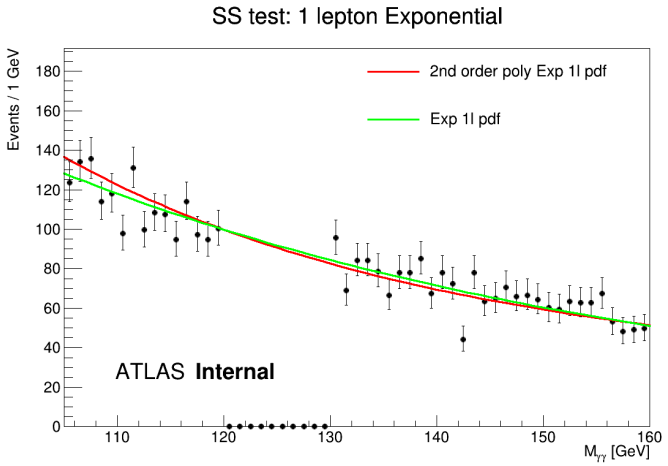

(a)

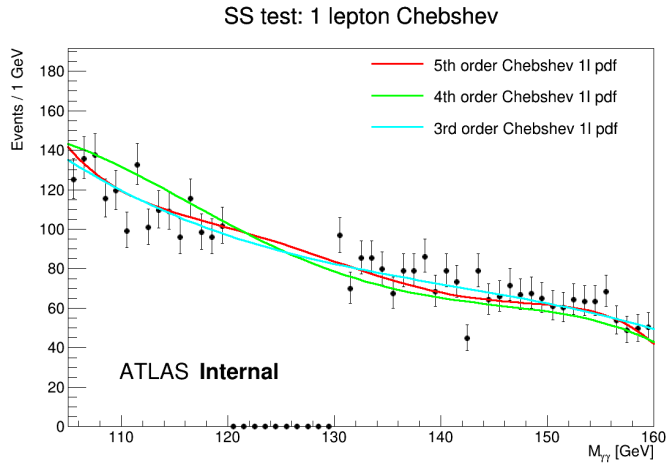

(b)

Figure 19: (a) Exponential and second order exponential fitted $m_{\gamma\gamma}$ distributions for 1l region, (b) 3,4,5 order Chebyshev polynomial fitted $m_{\gamma\gamma}$ distributions for 1l region

- $S_{spur} < 20\%\sigma_{bkg}$, where σ_{bkg} is the statistical uncertainty on the fitted background yields when fitting the signal+background model to a background-only Asimov dataset ($Z_{sp} = S_{spur}/\sigma_{bkg}$).

Especially, since the BDT tight and loose categories share the same $m_{\gamma\gamma}$ shape for the continuum background, but different signal yields. So both tight and loose categoriess have to calculate the yield of spurious signal independently.

Then, the one with the smallest degree of freedom is chosen if the multiple functions pass the criterion. An additional requirement for the χ^2 probability of a background-only fit to be larger than 5% ensures that the full mass range is described well. To calculate the χ^2, the whole mass range is divided into 55 bins, from 105 to 160 GeV. With the exclusion of the blinded region, the integral for (105, 120) and (130, 160) GeV, i.e. 45 bins in total, are normalized to 1. The χ^2 is calculated as:

$$\frac{\chi^2}{ndof} = \frac{\Sigma_1^{45} \frac{(x_{MC} - x_{data,SB})^2}{x_{data,SB}}}{45 - dof} \tag{5}$$

Table 18 lists this spurious signal test results in the WW1l case, taking $m_X = 1000GeV, m_S = 300GeV$ as the example. After the test, the 2^{nd} order exponential polynomial function passing the spurious signal test with the least degrees of freedom, is eventually chosen to be the function to describe the continuum background. The same tests are applied to all the mass points. After the spurious signal test, the $\mu_{sp}[\%]$ is counted as the uncertainty due to the mis-modelling of the background.

1-lepton case						
Function	Ndof	$N_{ss,tight}$	$\mu_{sp,tight}[\%]$	$Z_{sp,tight}[\%]$	$\frac{\chi^2}{ndof}[\%]$	Selected
Exp	1	0.014	7.1	9.1	0.20	Yes
ExpPoly2	2	0.009	4.6	6.2	0.18	Yes
Cheb3	3	0.020	10.2	19.3	0.026	No
Cheb4	4	0.018	8.8	21.2	0.048	No
Cheb5	5	0.016	8.2	23.3	0.027	No

Table 18: The spuirous signal test result for 1 lepton channel in $m_X = 1000GeV, m_S = 300GeV$.

Finally, the background renormalization factor is determined by the sideband data in each category. The di-photon mass spectrum can be found in Figure 20 to Figure 23.

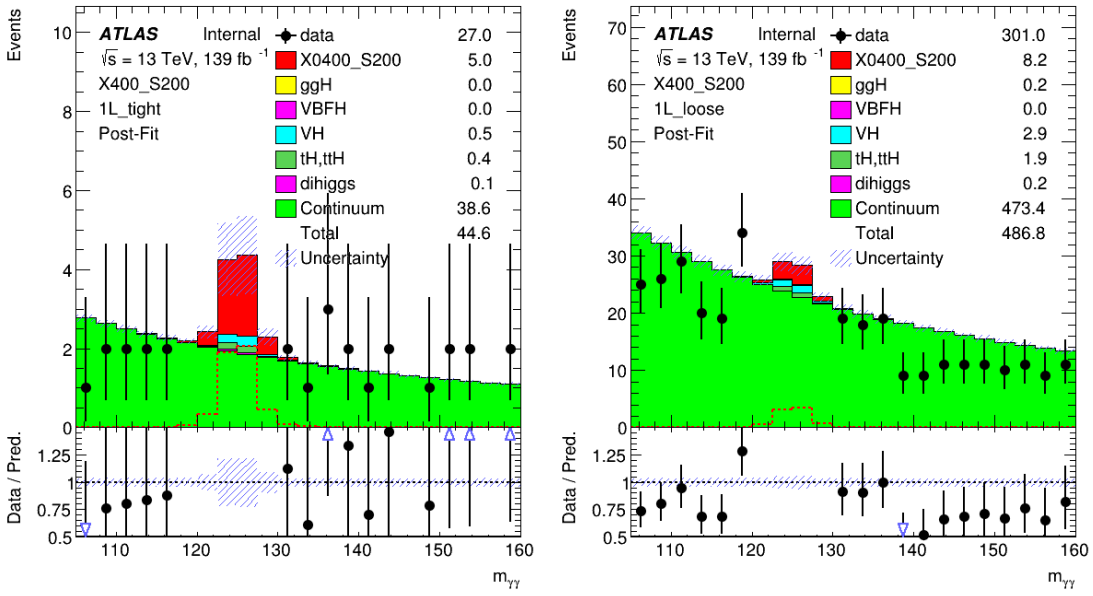

(a)

(b)

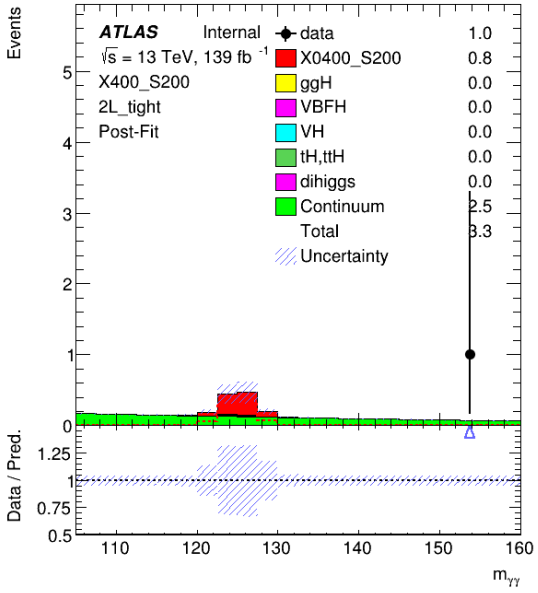

(c)

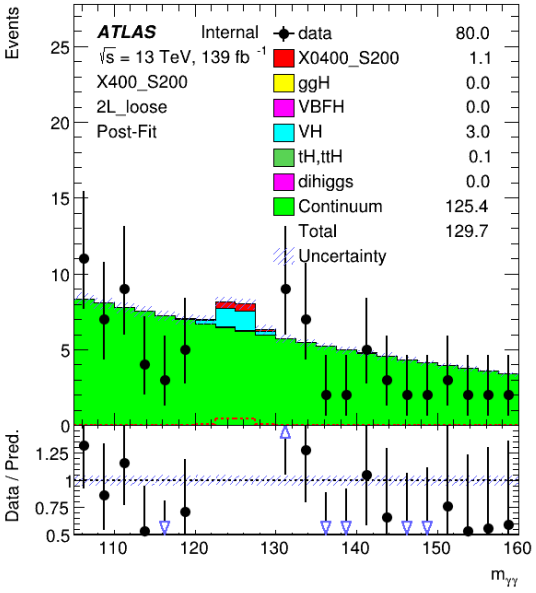

(d)

Figure 20: (a) $m_{\gamma\gamma}$ distributions for 1L BDT tight region, (b) $m_{\gamma\gamma}$ distributions for 1L BDT loose region, (c) $m_{\gamma\gamma}$ distributions for 2L BDT tight region, (d) $m_{\gamma\gamma}$ distributions for 2L BDT loose region, Events pass selections (mX,mS) =(400,200) GeV defined in signal region, with scaled smooth continuum background shapes.

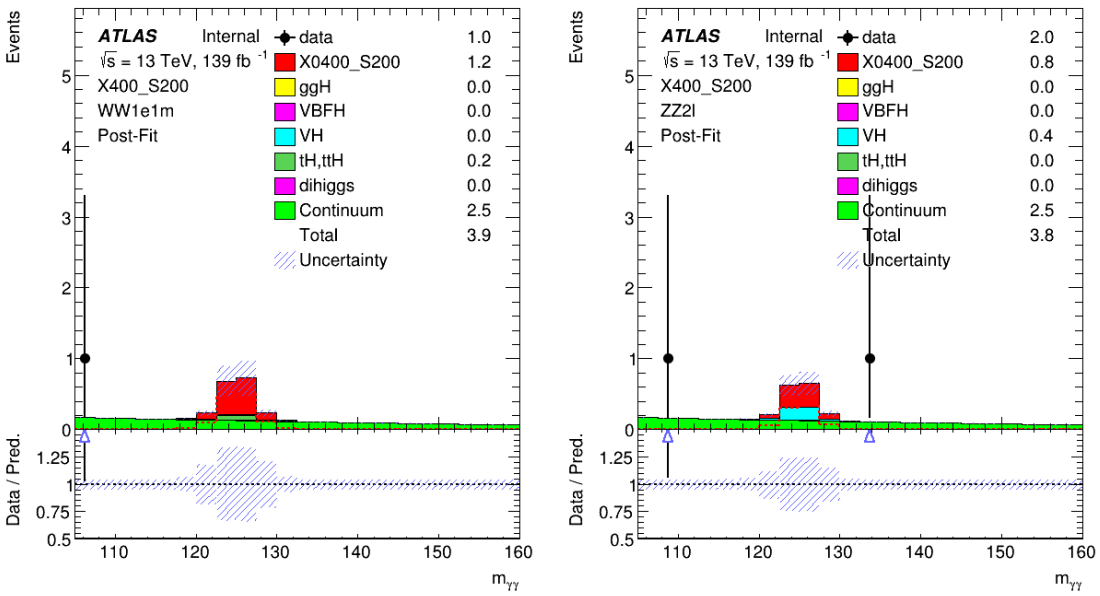

(a) (b)

Figure 21: (a) $m_{\gamma\gamma}$ distributions for WW1e1m region, (b) $m_{\gamma\gamma}$ distributions for ZZ2l region, Events pass selections (mX,mS) =(400,200) GeV defined in signal region, with scaled smooth continuum background shapes.

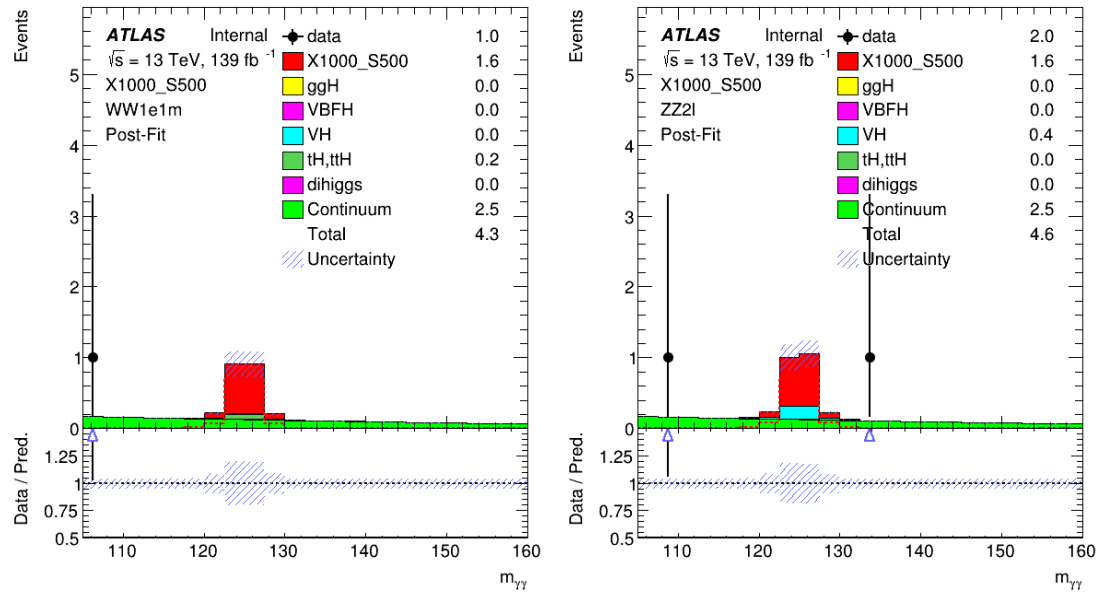

(a) (b)

Figure 22: (a) $m_{\gamma\gamma}$ distributions for WW1e1m region, (b) $m_{\gamma\gamma}$ distributions for ZZ2l region, Events pass selections (mX,mS) =(1000,500) GeV defined in signal region, with scaled smooth continuum background shapes.

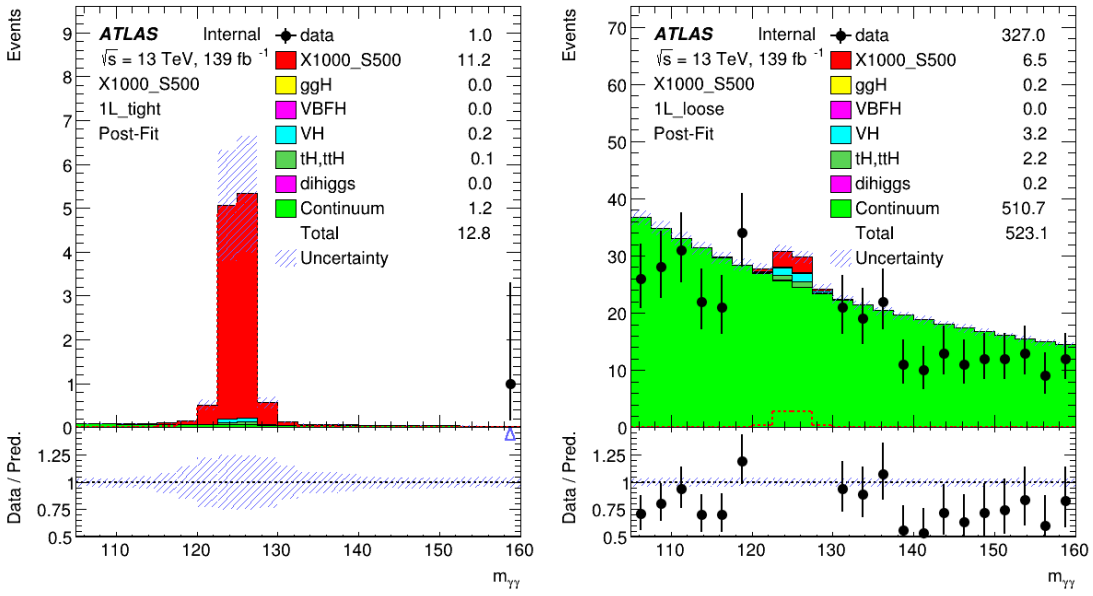

(a)

(b)

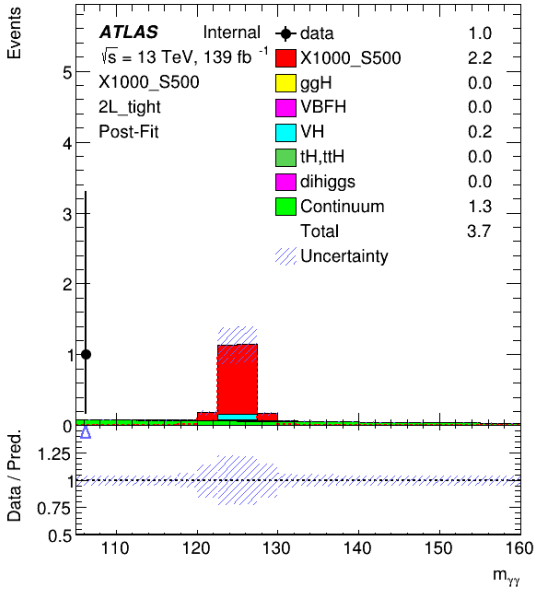

(c)

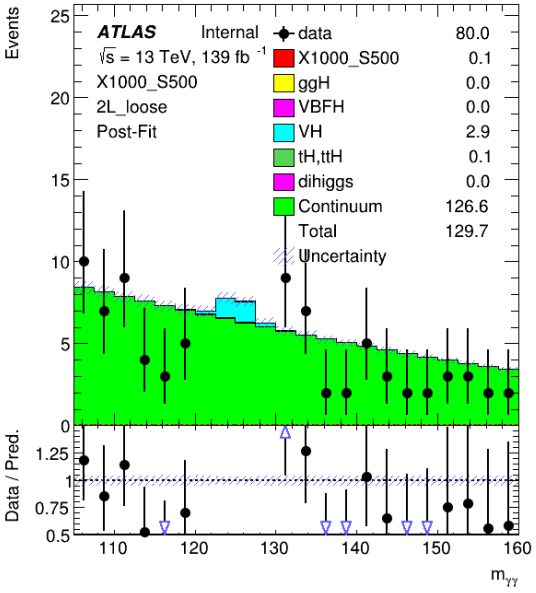

(d)

Figure 23: (a) $m_{\gamma\gamma}$ distributions for 1L BDT tight region, (b) $m_{\gamma\gamma}$ distributions for 1L BDT loose region, (c) $m_{\gamma\gamma}$ distributions for 2L BDT tight region, (d) $m_{\gamma\gamma}$ distributions for 2L BDT loose region, Events pass selections (mX,mS) =(1000,500) GeV defined in signal region, with scaled smooth continuum background shapes.

6 Systematic uncertainties

6.1 Theoretical uncertainties

This search relies on the calculation of predicted event numbers for all the SM processes, the uncertainties arise from the imperfect knowledge of:

- missing higher-order terms in the perturbative QCD calculations;
- the parton density functions (PDFs) and the value of the strong coupling constant, α_s;
- the QCD effects in the soft and collinear regime, hadronization and multi-parton interactions;

6.1.1 Pertubative QCD uncertainties for ggF

The perturbative QCD uncertainties for single Higgs processes are studied under STXS 1.2 scheme. For ggF process, this term is broken into eighteen individual nuisance parameters:

- Four parameters covering the uncertainty in modeling of the jet multiplicities. This is the so-called Boughezal-Liu-Petriello-Tackmann-Walsh (BLPTW) uncertainty scheme (see Section I.4.2.c of Ref. [40]). The four sources of uncertainties are the overall QCD scale uncertainties in fixed-order calculations (QCDscale_ggH_mu), and the resummation scale uncertainty (QCDscale_ggH_res), the migration between the $0 \rightarrow 1$ jet bins (QCDscale_ggH_mig01) and the migration between $1 \rightarrow 2$ jet bins (QCDscale_ggH_mig12).
- Three parameters covering the migration uncertainties across p_T^H below 200 GeV. One of them covers the migration in the 0-jet bins at 10 GeV (QCDscale_ggH_nJ0) while the other to take into account the migrations at 60 (QCDscale_ggH_pTH60) and 120 (QCDscale_ggH_pTH120) GeV.
- Four additional nuisance parameters take into account the migrations between the bins split in m_{jj} (QCDscale_ggH_deltaMJJ350, QCDscale_ggH_deltaMJJ700, QCDscale_ggH_deltaMJJ1000, QCDscale_ggH_deltaMJJ1500).
- One parameter to cover the migrations across p_T^{Hjj} bins (QCDscale_ggH_pTHJJ).
- Six nuisance parameters cover the uncertainties in the high transverse momentum regime. Four of them are designed to cover the migrations between p_T^H bins (QCDscale_ggH_pTH300, QCDscale_ggH_pTH450, QCDscale_ggH_pTH650, QCDscale_ggH_pTHNorm). QCDscale_ggH_pTHNorm covers the migrations across the $p_T^H = 200$ GeV boundary. The high p_T regime is also affected by migrations in p_T^{Hj}/p_T^H covered by a nuisance parameter called QCDscale_ggH_deltapTHJ_pTH in the distributions shown in this section. Additionally, the high p_T^H is sensible to the top mass scheme used in the calculations. To take into account this effect the nuisance parameter QCDscale_ggH_mTop was introduced.

This set of eighteen uncertainties was estimated by the LHC Higgs WG and was collected in a preliminary document in which more information can be obtained about the scheme[2]

[2] https://twiki.cern.ch/twiki/pub/LHCPhysics/LHCHWGFiducialAndSTXS/simplifiedXS_ggF_1.2_theory_uncertainty.pdf

6.1.2 Pertubative QCD uncertainties for VBF and VH

For VH production the inclusive cross section uncertainties [41] are introduced separately for the three main VH production modes (Wh, $q\bar{q} \rightarrow ZH$ and $gg \rightarrow ZH$) and include the effect of renormalization and factorization scale by a factor of 3 around their nominal value. These uncertainties are treated as correlated across all the STXS bins for each VH production mode, and furthermore correlated across Drell-Yan VH production modes. Migration uncertainties due to p_T^V and N_{jets} boundaries are considered. Absolute uncertainties are derived from the relative variations independently in each of the p_T^V boundaries of 75,150,250,400 GeV and they apply in a correlated manner to any further sub-division in N_{jets}. Analogously, migration uncertainties induced by the N_{jets} boundaries of = 1− and >= 2−jets are obtained in each p_T^V bin and V decay mode.

As a summary of the VH uncertainties, 7 nuisance parameters are considered for the three main VH production modes:

- The overall inclusive scale uncertainty.
- Four parameters covering the migrations between p_T^V bins
- Two parameters covering the migrations between bins with different jet multiplicities.

The uncertainties for VBF and VH-hadronic were obtained in a similar fashion by obtaining 10 nuisance parameters:

- The overall inclusive scale uncertainty.
- Two parameters covering the N_{jets} migration from 0 + 1jet bins into the 2-jets bins and migrations between 2- and 3-jet bins with $p_T^{Hjj} > 25$ GeV and $p_T^{Hjj} < 25$ GeV.
- One parameter to cover for migrations between the $p_T^H = 200$ GeV boundary.
- Six parameters covering the migrations between m_{jj} bins with boundaries at 60, 120, 350,700,1000 and 1500 GeV.

6.1.3 Pertubative QCD uncertainties for $t\bar{t}H$

As several STXS bins divided in p_T^H are defined in the $t\bar{t}h$ production mode, apart from the common overall normalization scale, uncertainties to take into account for the migrations across different p_T^H bins are taken into account. In general, six nuisance parameters are considered:

- The overall inclusive scale uncertainty.
- Five parameters covering the migrations between p_T^H bins with boundaries at 60, 120, 200,300,450 GeV.

Uncertainties arising from the comparison with an alternative generator and other sources of uncertainties related to the modeling of initial- and final-state radiation have not been considered so far.

6.1.4 Pertubative QCD uncertainties for di-Higgs processes

Inclusive ggF cross sections for Higgs boson pair production are reported in [42] for m_H = 125 GeVwith the central scale $\mu_0 = \mu_R = \mu_F = M_{HH}/2$. The uncertainties scheme to be considered are PDF, α_s (combined "PDF + α_s unc"), scale and m_{top} (combined "Scale + mtop unc"), as recommended by LHC-HH group [43].

6.1.5 PDF and α_s uncertainties

The PDF and α_s uncertainties are evaluated using generator-level variations coming from on-the-fly weights. The nominal set of PDF used is PDF4LHC15 at NLO which, apart from the central PDF, comes along with 30 error sets. Each of them corresponds to an eigenvector of the covariance matrix in the parameter space of the PDF fit. This is usually called the Hessian representation and the total PDF uncertainty is computed using the master formula. However, in this analysis, the total PDF uncertainty is not computed and the contribution of each eigenvector to the total Hessian PDF uncertainty is propagated through the measurement to facilitate the combination with other decay channels.

Two additional PDF sets are provided with a different value of α_s assumed in the PDF fit. The nominal value of 0.118 is varied by ±0.0015 to compute the α_s uncertainty at the 68% of confidence level.

6.1.6 Parton shower uncertainties

TODO: Consider how many PS uncertainties need to be calculated. For completeness, there should be all single Higgs, di-Higgs processes and all signals.

6.2 Experimental Uncertainties

6.2.1 Uncertainties on signal yields

The uncertainties on signal yields can come from the measured integrated luminosity, the pileup reweighting, the spurious signal, and object (mainly from photons and jets in this analysis) reconstruction as well as particle identification criteria.

The uncertainty due to the combined 2015-2018 integrated luminosity is 1.7%. It is derived, following the methodology documented in Ref [11], from a preliminary calibration of the luminosity scale using x-y beam-separation scans performed from 2015 to 2018. This uncertainty is applied to the signal, SM Higgs as well as the di-Higgs process.

106 experimental systematic sources are taken into account: the main experimental systematics are jet reconstruction uncertainties, including jet flavor composition, flavor response, modeling, topology, jet energy resolution and photon uncertainties on isolation and identification efficiency. Other important sources come from pileup modeling in simulation, spurious signal as discussed in Section 5.2, photon reconstruction and identification efficiencies, as well as the uncertainties on the efficiency of diphoton trigger. Because the impacts of JER and JES on the signal yields for each category are small with respect to other systematic sources, only 1 NP is assigned to cover the combined effect. The PRW systematics is computed by applying the standard ATLAS correction factors.

Each value of the systematics is computed as the relative difference from nominal signal MC samples with $\pm 1\sigma$ variation:

$$\delta n_c^{\pm 1\sigma} = \frac{n_c^{\pm 1\sigma}}{n_c^{\text{nom}}} - 1 \tag{6}$$

Systematic uncertainties are computed for each individual category c. All the systematic sources are implemented in the fit with asymmetric constraints since up and down variations can have different values. A threshold of 0.5% on the variation value is applied when implementing these nuisance parameters to suppress trivial contributions and simplify the computing processes. After this selection, there are 32-39 terms left depending on categories.

6.2.2 Uncertainty on continuum background estimation

As described in Section 5.2, the continuum background models for different categories are determined by fitting the di-photon mass on the sideband data in the region of $\gamma\gamma + 0 - lepton$. The shape differences between this region and $\gamma\gamma + \ell\nu jj$ (1L) and $\gamma\gamma\ell\nu\ell\nu$ (2L) could introduce additional uncertainties in the estimations of background yields for individual categories. This method and corresponding uncertainties can only be evaluated by the MC, due to the low statistics in data. In practice, the region of $\gamma\gamma + 0 - lepton + jets$ as introduced in Section 1.2.3 is adapted to mimic the event topologies for 1-lepton and 2-lepton categories. The mass distributions for di-photon are fitted with the selected function obtained in Section 5.2. The variations between $\gamma\gamma + 0 - lepton + jet$ and $\gamma\gamma + \ell\nu jj/\gamma\gamma\ell\nu\ell\nu$ are computed bin-by-bin, in the region of $m_{\gamma\gamma} \in [105, 160]$GeV with bin width equal to 1 GeV. The average variation for all bins is chosen as the uncertainty of the background modeling.

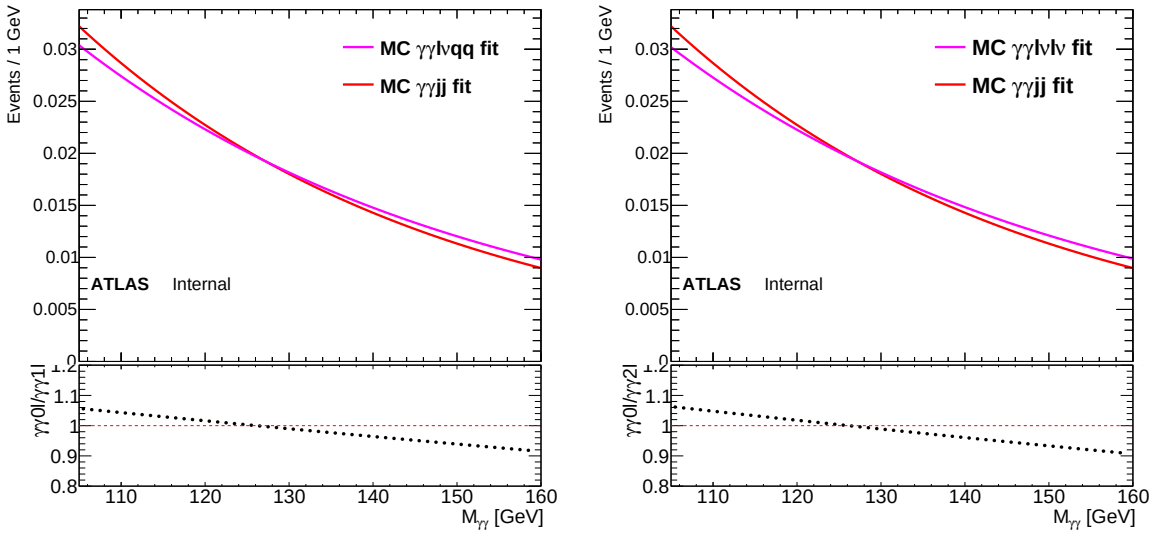

Figure 24: Deviations of di-photon mass distributions between $\gamma\gamma + 0L$ and $\gamma\gamma + 1L$ ($\gamma\gamma + 2L$).

7 Statistical interpretation

7.1 Statistical model

The statistical model is built up with a binned likelihood function. The model is constructed in the following form.

The signal extraction from data is based on the statistical model of binned likelihood estimation. This binned likelihood is built from Poisson distribution in each bin as follows:

$$\mathcal{L} = \prod_{c\in\text{channels}} \prod_{b\in\text{bins}} \text{Poisson}(n^{\text{obs}}_{c,b} | n^{S}_{c,b}, n^{B}_{c,b}) \times \prod_{s\in\mathbb{S}} \mathcal{G}(0|\theta_s, 1), \tag{7}$$

where c stands for channel index, and b is the bin index for each channel. The number of events observed in each bin is shown as $n^{\text{obs}}_{c,b}$, and the expected numbers of signal and background in such bin are $n^{S}_{c,b}$ and $n^{B}_{c,b}$, respectively. $n^{S}_{c,b}$ can be written as a function of the cross-section of X production: σ, which is shared among different bins and channels. This parameter is treated as the Parameter-of-Interest (POI). The number of background includes contributions from the SM resonant backgrounds n_{SM} and continuum backgrounds n_{cont}. The shape of the continuum background is determined by sideband fit and the normalization is floating during the fit. The systematic uncertainty is shown as marked as s for each term and constraint with a Gaussian distribution: $\mathcal{G}(0|\theta_s, 1)$, where θ_s is the nuisance parameter (NP) in fit.

7.2 Upper limit setting

A likelihood ratio-based test statistic is used in the statistical analysis. It is defined as follows:

$$\tilde{q}_\sigma = \begin{cases} -2\ln\frac{\mathcal{L}(\sigma,\hat{\hat{\boldsymbol{\theta}}}(\sigma))}{\mathcal{L}(0,\hat{\hat{\boldsymbol{\theta}}}(0))} & \text{if } \hat{\sigma} < 0 \\ -2\ln\frac{\mathcal{L}(\sigma,\hat{\hat{\boldsymbol{\theta}}}(\sigma))}{\mathcal{L}(\hat{\sigma},\hat{\boldsymbol{\theta}})} & \text{if } 0 \le \hat{\sigma} \le \sigma \\ 0 & \text{if } \hat{\sigma} > \sigma \end{cases} \tag{8}$$

where $\mathcal{L}$ stands for the likelihood function for the statistical model of the analysis, $\boldsymbol{\theta}$ is a set of nuisance parameters through which the systematic uncertainties are introduced, and the parameter of interest σ is the cross-section of resonant X production. Single hat stands for unconditional fit and double hat for conditional fit, i.e., POI σ is fixed to a certain value. With this test statistic, the upper limits of the cross section X production at 95% confidence level can be derived by using the CL_s method [44] under the asymptotic approximation [45].

8 Results

The simultaneous binned fit on $m_{\gamma\gamma}$ sharing the same set of parameters for the background modeling is performed on different categories with `TRExFitter`. One advantage of binned fit is that the variations of the nuisance parameters can be easily incorporated into the content for each bin. Thus, it is easier for the estimation of some systematics in particular those for shape uncertainties.

Configurations of `TRExFitter` are listed in Table 19. The binning width for di-photon mass is chosen to be 2.5GeV which is a bit larger than the di-photon mass resolution from Higgs in ATLAS.

Parameters	Value
`MCstatThreshold`	0.005
`SystPruningNorm`	0.005
`SystPruningShape`	0.005
`BlindSRs`	FALSE
`FitType`	SPLUSB
`FitRegion`	CRSR
`LimitType`	ASYMPTOTIC
`Observed Variable`	$m_{\gamma\gamma}$
`Variable Range`	(105, 160)GeV
`Blind Range`	(120, 130)GeV
`Numebr of bins`	22
`Bin width`	2.5 GeV

Table 19: Summary of configurations used in `TRExFitter`.

8.1 Expected results

The expected 95% C.L. upper limits on cross-section are derived for X separately assuming $S \rightarrow WW$ with 100%, S decaying 100% to ZZ, or S decays to WW and ZZ following the SM prediction. Figure 25 - 27 show the results with the 3 scenarios above. The upper limits in other m_X values are extrapolated to a plane through the existing results. $m_X = 1000GeV, m_S = 400GeV$ provides the best limit among all the mass points with the assumption of the decay of S 100% to WW. The exact values of the limits in detail are summarized in Table 20, 21 and 22.

In order to compute the limits for the $\sigma(pp \rightarrow X \rightarrow S(\rightarrow ZZ/WW)H)$, WW1l, WW2l , WW$e\mu$ and ZZ2l channels are combined in which WW1l dominates, as Figure 27 and Table 22 show. The results are obtained with Asymptotic fits on the Asmovi data and a cross check with throwing toy MC to extract the limit which is documented in Appendix F. As Table 25 shows, these two methods agree with each other. Moreover, the signal injection test has been done and fitted signal strengths are consisent with the injected ones as Appendix G shows.

m_X [GeV]	$m_S[GeV]$	$+2\sigma$ [pb]	$+1\sigma$ [pb]	Median [pb]	-1σ [pb]	-2σ [pb]
300	170	1.327	0.863	0.578	0.417	0.310
400	170	1.166	0.788	0.535	0.385	0.287
400	200	1.126	0.769	0.524	0.378	0.281
500	170	0.762	0.499	0.333	0.240	0.179
500	200	0.831	0.557	0.376	0.271	0.202
500	300	0.981	0.673	0.460	0.332	0.247
600	170	0.648	0.420	0.280	0.202	0.150
600	200	0.573	0.380	0.256	0.184	0.137
600	300	0.615	0.416	0.282	0.203	0.151
600	400	0.796	0.538	0.364	0.263	0.196
750	170	0.564	0.356	0.235	0.169	0.126
750	200	0.450	0.293	0.195	0.140	0.105
750	300	0.450	0.298	0.200	0.144	0.108
750	400	0.466	0.300	0.199	0.144	0.107
750	500	0.776	0.523	0.355	0.256	0.191
1000	170	0.410	0.254	0.167	0.120	0.089
1000	200	0.326	0.202	0.133	0.096	0.071
1000	300	0.280	0.175	0.115	0.083	0.062
1000	400	0.272	0.172	0.113	0.081	0.061
1000	500	0.309	0.196	0.129	0.093	0.069

Table 20: Upper limits at the 95% confidence level for the cross-section of the gluon fusion production of the resonance $X \rightarrow SH$ and the S particle is assumed to decay 100% to WW.

8.2 Pull, ranking and correlation matrix

For the process of the fit, if the impacts of the systematic uncertainties are less than 0.5%, the corresponding NPs are dropped by the fit tool to simplify the procedure. The pull and ranking distributions for survived NPs are shown in Figure 28 for the signal with $m_X = 1000\,\text{GeV}$ and $m_S = 500\,\text{GeV}$. Correlations between major NPs can be found in Figure 29 for this signal. No obvious abnormal behaviors from the pulls and their constraints have been observed in this analysis during the Asimov fit and the most significant impacts of the uncertainties on the extracted signal yield turn out to be from egamma systematic uncertainties.

m_X [GeV]	$m_S[GeV]$	+2σ [pb]	+1σ [pb]	Median [pb]	−1σ [pb]	−2σ [pb]
300	170	5.059	3.230	2.119	1.527	1.137
400	170	3.875	2.469	1.620	1.167	0.870
400	200	2.597	1.656	1.088	0.784	0.584
500	170	3.075	1.953	1.280	0.923	0.687
500	200	2.187	1.392	0.915	0.659	0.491
500	300	2.142	1.366	0.900	0.648	0.483
600	170	2.725	1.726	1.130	0.814	0.606
600	200	1.926	1.223	0.803	0.579	0.431
600	300	1.753	1.113	0.732	0.527	0.393
600	400	2.036	1.297	0.854	0.615	0.458
750	170	2.537	1.606	1.050	0.757	0.564
750	200	1.825	1.155	0.758	0.547	0.407
750	300	1.417	0.898	0.589	0.425	0.316
750	400	1.532	0.972	0.639	0.460	0.343
750	500	1.749	1.112	0.731	0.527	0.393
1000	170	2.384	1.499	0.983	0.708	0.527
1000	200	1.999	1.260	0.825	0.594	0.443
1000	300	1.216	0.766	0.502	0.362	0.270
1000	400	1.209	0.762	0.500	0.360	0.268
1000	500	1.272	0.803	0.526	0.379	0.282

Table 21: Upper limits at the 95% confidence level for the cross-section of the gluon fusion production of the resonance $X \rightarrow SH$ and the S particle is assumed to decay fully to ZZ.

m_X [GeV]	$m_S[GeV]$	+2σ [pb]	+1σ [pb]	Median [pb]	−1σ [pb]	−2σ [pb]
300	170	0.600	0.896	0.600	0.433	0.322
400	170	0.555	0.819	0.555	0.400	0.298
400	200	0.710	1.041	0.710	0.512	0.381
500	170	0.346	0.518	0.346	0.250	0.186
500	200	0.509	0.754	0.509	0.367	0.273
500	300	0.666	0.974	0.666	0.480	0.357
600	170	0.291	0.437	0.291	0.209	0.156
600	200	0.346	0.514	0.346	0.249	0.186
600	300	0.407	0.601	0.407	0.294	0.219
600	400	0.632	0.933	0.632	0.456	0.339
750	170	0.244	0.369	0.244	0.176	0.131
750	200	0.264	0.396	0.264	0.190	0.142
750	300	0.290	0.432	0.290	0.209	0.156
750	400	0.345	0.521	0.345	0.249	0.185
750	500	0.657	0.968	0.657	0.474	0.353
1000	170	0.173	0.264	0.173	0.125	0.093
1000	200	0.179	0.273	0.179	0.129	0.096
1000	300	0.167	0.254	0.167	0.120	0.089
1000	400	0.196	0.298	0.196	0.141	0.105
1000	500	0.239	0.363	0.239	0.172	0.128

Table 22: Upper limits at the 95% confidence level for the cross-section of the gluon fusion production of the resonance $X \rightarrow SH$ and the S particle is assumed to decay to WW/ZZ following the SM prediction.

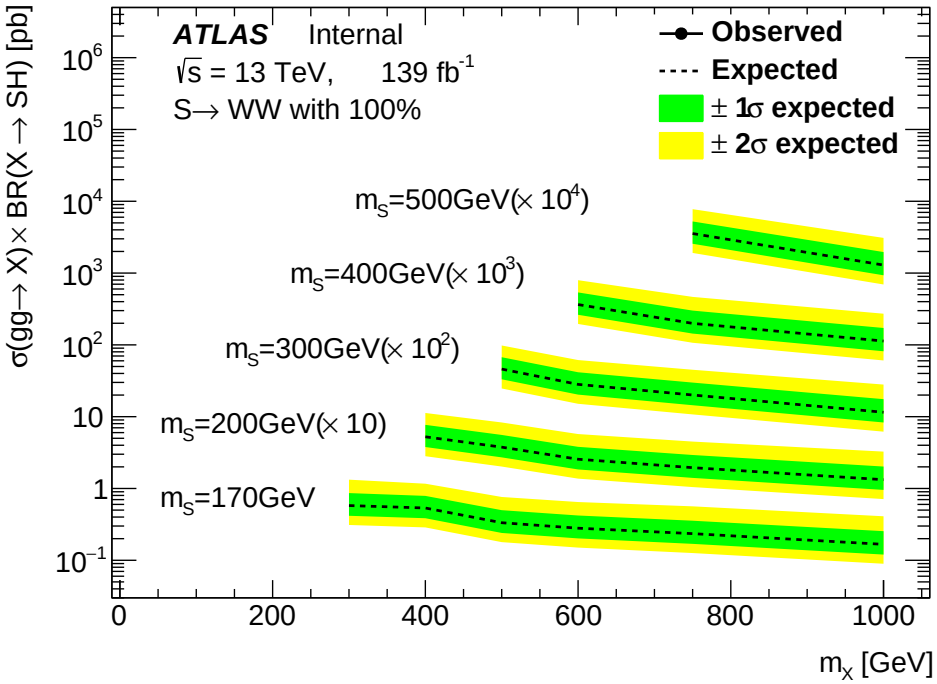

Figure 25: Expected 95% C.L. upper limits on $\sigma(pp \to X \to SH)$ for resonance as a function of the mass of the heavy scalars X and S, assuming $S \to WW$ with 100%.

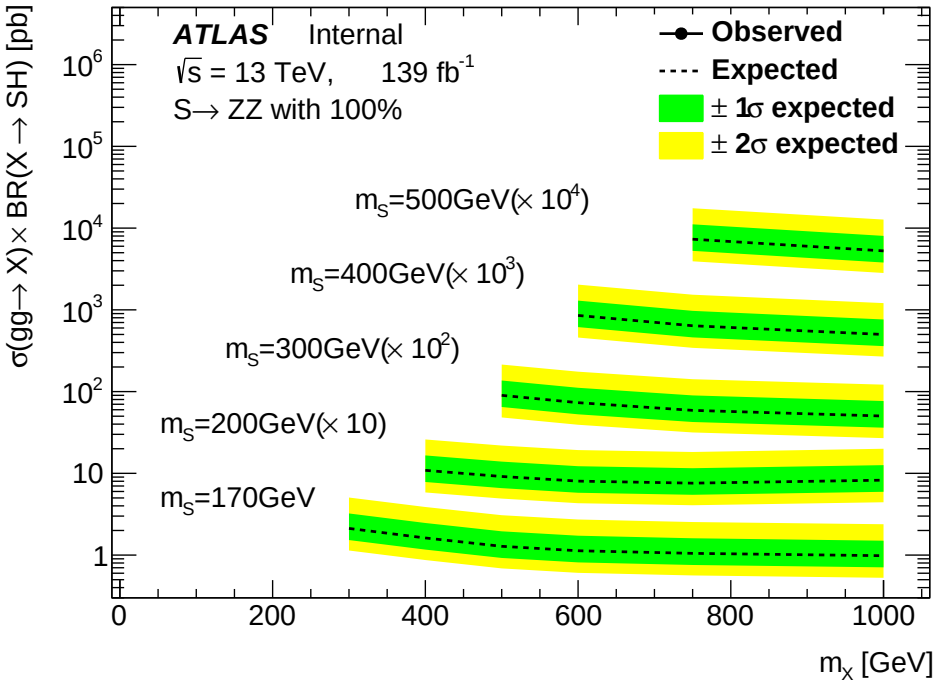

Figure 26: Expected 95% C.L. upper limits on $\sigma(pp \to X \to SH)$ for resonance as a function of the mass of the heavy scalars X and S, assuming $S \to ZZ$ with 100%.

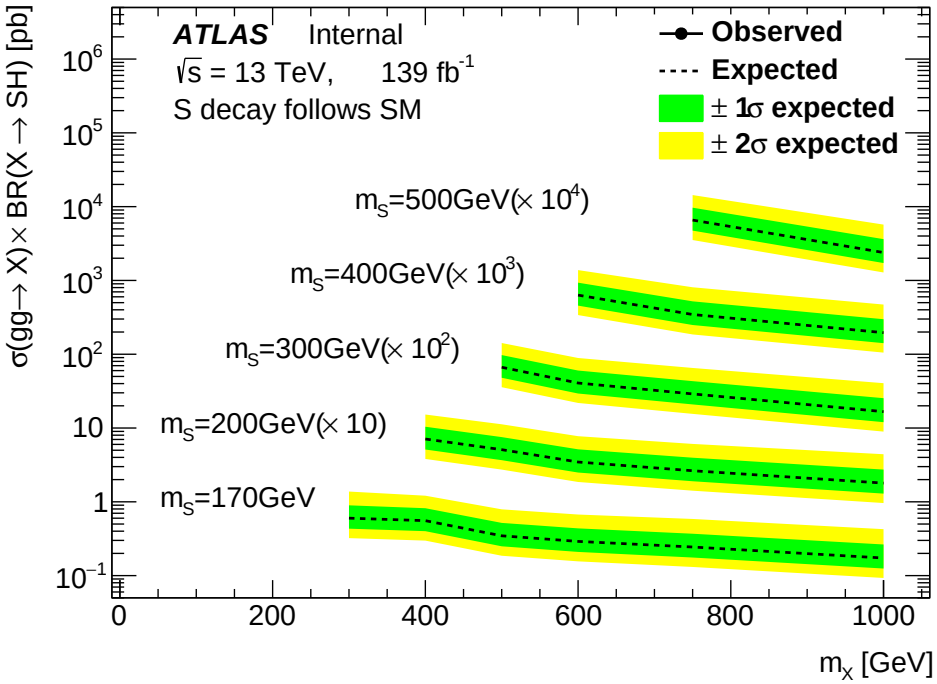

Figure 27: Expected 95% C.L. upper limits on $\sigma(pp \to X \to SH)$ for resonance as a function of the mass of the heavy scalars X and S, where the branching ratio of S to WW/ZZ is assumed to be SM-like.

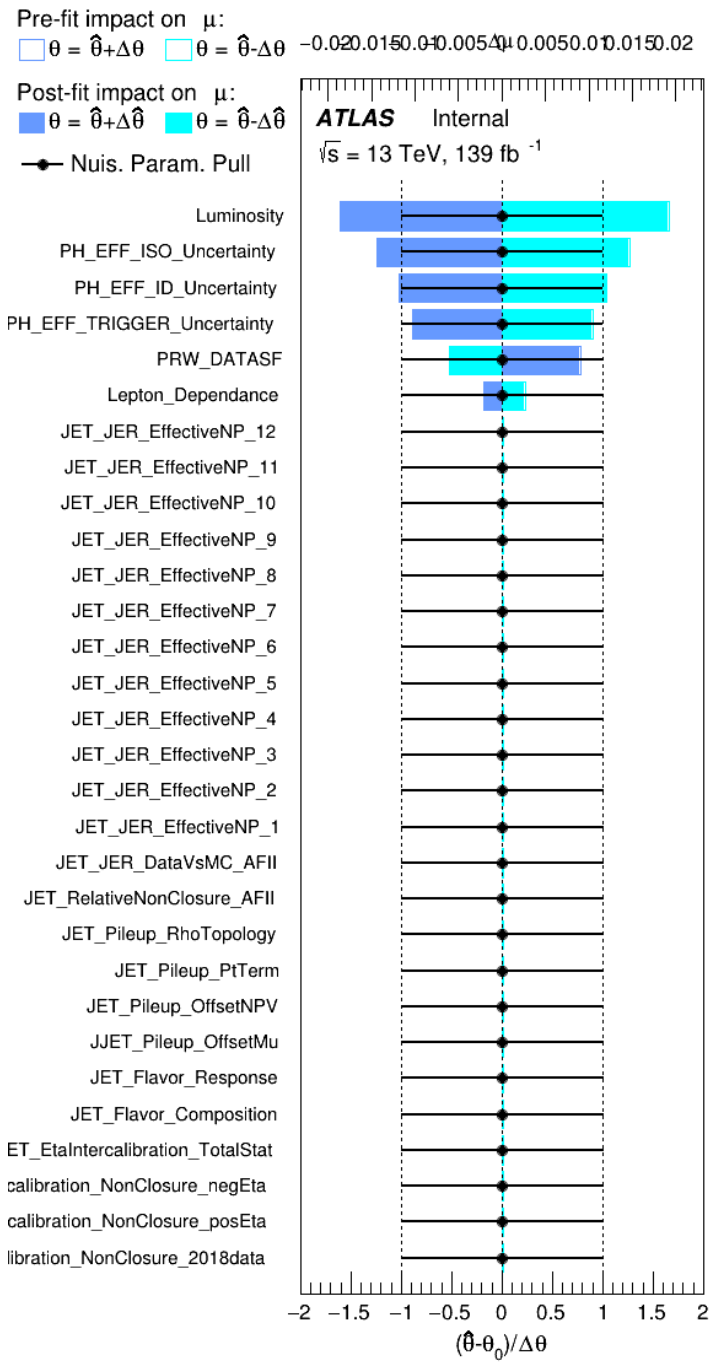

Figure 28: NPs ranking and pull distrbutions in (m_X 1000 GeV, m_S = 500 GeV) fit.

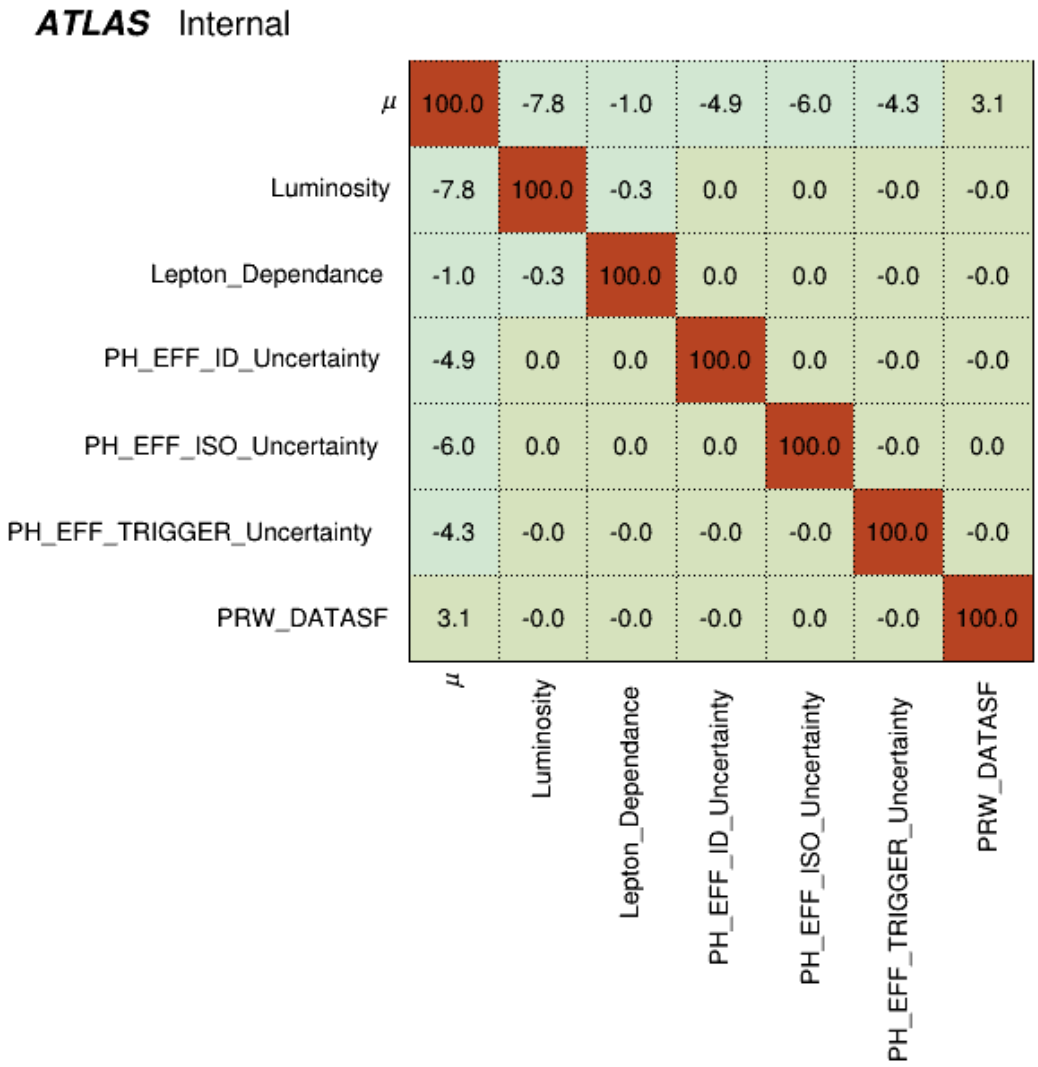

Figure 29: Major NP correlation in $(m_X 1000\,\text{GeV}, m_S = 500\,\text{GeV})$ fit.

9 Summary

In this note, a search for heavy resonance X decaying into a new scalar S and a SM Higgs boson with subsequently this Higgs boson decaying to two photons and S decaying to WW or ZZ is performed. In this analysis, both fully leptonic and semileptonic decays of WW bosons and semileptonic decays of ZZ bosons are explored. Analysis selections are optimized separately for different final states based on their dedicated event topologies. In order to improve significance, the BDT method is performed based on reconstructed discriminating variables. An optimized threshold on the BDT output divides events into tight and loose regions to maximize the significance and the signal contribution is extracted from a binned fit to $m_{\gamma\gamma}$ distribution from 105 to 160 GeV. The signal Higgs boson contribution is determined from SM predictions and the non-resonant background is estimated from $m_{\gamma\gamma}$ sideband fit with analytic function in the $\gamma\gamma + 0L$ control region. The binned likelihood fit is performed by combining all channels as well as assuming S 100% decays to WW or ZZ to extract signal contributions with different m_X and m_S hypotheses.

The observed (expected) upper limits at the 95% confidence level on the cross-section for $gg \to X \to Sh$ assuming the decay of S following the SM prediction is between X fb (167 fb) and Y fb (710 fb).

References

[1] ATLAS Collaboration, *Observation of a new particle in the search for the Standard Model Higgs boson with the ATLAS detector at the LHC*, Phys. Lett. B **716** (2012) 1, arXiv: 1207.7214 [hep-ex] (cit. on p. 8).

[2] CMS Collaboration, *Observation of a new boson at a mass of 125 GeV with the CMS experiment at the LHC*, Phys. Lett. B **716** (2012) 30, arXiv: 1207.7235 [hep-ex] (cit. on p. 8).

[3] ATLAS Collaboration, *Searches for Higgs boson pair production in the $hh \to bb\tau\tau, \gamma\gamma WW^*, \gamma\gamma bb, bbbb$ channels with the ATLAS detector*, Phys. Rev. D **92** (2015) 092004, arXiv: 1509.04670 [hep-ex] (cit. on p. 8).

[4] ATLAS Collaboration, *Combination of searches for Higgs boson pairs in pp collisions at $\sqrt{s} = 13$ TeV with the ATLAS detector*, (2019), arXiv: 1906.02025 [hep-ex] (cit. on p. 8).

[5] CMS Collaboration, *Combination of Searches for Higgs Boson Pair Production in Proton–Proton Collisions at $\sqrt{s} = 13$ TeV*, Phys. Rev. Lett. **122** (2019) 121803, arXiv: 1811.09689 [hep-ex] (cit. on p. 8).

[6] S. von Buddenbrock et al., *Phenomenological signatures of additional scalar bosons at the LHC*, Eur. Phys. J. **C76** (2016) 580, arXiv: 1606.01674 [hep-ph] (cit. on p. 8).

[7] S. von Buddenbrock et al., *Constraints on a 2HDM with a singlet scalar and implications in the search for heavy bosons at the LHC*, Journal of Physics G: Nuclear and Particle Physics **46** (2019) 115001, ISSN: 1361-6471, URL: http://dx.doi.org/10.1088/1361-6471/ab3cf6 (cit. on p. 8).

[8] S. Buddenbrock et al., *The emergence of multi-lepton anomalies at the LHC and their compatibility with new physics at the EW scale*, JHEP **10** (2019) 157, arXiv: 1901.05300 [hep-ph] (cit. on p. 9).

[9] S. von Buddenbrock et al., *Multi-lepton signatures of additional scalar bosons beyond the Standard Model at the LHC*, J. Phys. G **45** (2018) 115003, arXiv: 1711.07874 [hep-ph] (cit. on p. 9).

[10] *CERN Yellow Report 4*, https://twiki.cern.ch/twiki/bin/view/LHCPhysics/LHCHWG (cit. on p. 9).

[11] ATLAS Collaboration, *Luminosity determination in pp collisions at $\sqrt{s} = 13$ TeV using the ATLAS detector at the LHC*, ATLAS-CONF-2019-021, 2019, URL: https://cds.cern.ch/record/2677054 (cit. on pp. 10, 52).

[12] G. Avoni et al., *The new LUCID-2 detector for luminosity measurement and monitoring in ATLAS*, Journal of Instrumentation **13** (2018) P07017, URL: https://doi.org/10.1088/1748-0221/13/07/p07017 (cit. on p. 10).

[13] ATLAS Collaboration, *ATLAS data quality operations and performance for 2015–2018 data-taking*, (2019), arXiv: 1911.04632 [hep-ex] (cit. on p. 10).

[14] M. Aaboud et al., *Measurement of the photon identification efficiencies with the ATLAS detector using LHC Run 2 data collected in 2015 and 2016*, The European Physical Journal C **79** (2019), ISSN: 1434-6052, URL: http://dx.doi.org/10.1140/epjc/s10052-019-6650-6 (cit. on p. 10).

[15] ATLAS Internal, *ExtendedPileupReweighting*, 2016, URL: https://twiki.cern.ch/twiki/bin/view/AtlasProtected/ExtendedPileupReweighting (cit. on p. 10).

[16] T. Sjöstrand et al., *An introduction to PYTHIA 8.2*, Comput. Phys. Commun. **191** (2015) 159, arXiv: 1410.3012 [hep-ph] (cit. on pp. 10, 11).

[17] ATLAS Collaboration, *Summary of ATLAS Pythia 8 tunes*, ATL-PHYS-PUB-2012-003, 2012, URL: https://cds.cern.ch/record/1474107 (cit. on p. 10).

[18] ATLAS Collaboration, *ATLAS Pythia 8 tunes to 7 TeV data*, ATL-PHYS-PUB-2014-021, 2014, URL: https://cds.cern.ch/record/1966419 (cit. on pp. 11, 13).

[19] R. D. Ball et al., *Parton distributions for the LHC Run II*, JHEP **04** (2015) 040, arXiv: 1410.8849 [hep-ph] (cit. on p. 11).

[20] D. J. Lange, *The EvtGen particle decay simulation package*, Nucl. Instrum. Meth. A **462** (2001) 152 (cit. on p. 11).

[21] The ATLAS Collaboration, *The simulation principle and performance of the ATLAS fast calorimeter simulation FastCaloSim*, (2010), ATL-PHYS-PUB-2010-013, URL: http://cdsweb.cern.ch/record/1300517 (cit. on p. 11).

[22] *LHC Higgs Cross Section Working Group*, URL: https://twiki.cern.ch/twiki/bin/view/LHCPhysics/CERNYellowReportPageBR#Higgs_2_fermions (cit. on p. 12).

[23] P.M. Nadolsky, et al., *Implications of CTEQ global analysis for collider observables*, tech. rep., 2008 013004, URL: %7Bhttp://prd.aps.org/abstract/PRD/v78/i1/e013004%7D (cit. on p. 12).

[24] ATLAS Collaboration, *Measurement of the Z/γ^* boson transverse momentum distribution in pp collisions at $\sqrt{s} = 7$ TeV with the ATLAS detector*, JHEP **09** (2014) 145, arXiv: 1406.3660 [hep-ex] (cit. on p. 12).

[25] G. Bozzi, S. Catani, D. de Florian, and M. Grazzini, *Transverse-momentum resummation and the spectrum of the Higgs boson at the LHC*, Nucl. Phys. B **737** (2006) 73, arXiv: hep-ph/0508068 (cit. on p. 12).

[26] K. Hamilton, P. Nason, E. Re, and G. Zanderighi, *NNLOPS simulation of Higgs boson production*, JHEP **10** (2013) 222, arXiv: 1309.0017 [hep-ph] (cit. on p. 12).

[27] J. R. Andersen et al., *Handbook of LHC Higgs Cross Sections: 3. Higgs Properties*, (2013), ed. by S. Heinemeyer, C. Mariotti, G. Passarino, and R. Tanaka, arXiv: 1307.1347 [hep-ph] (cit. on p. 12).

[28] R. D. Ball, V. Bertone, S. Carrazza, C. S. Deans, L. Del Debbio, et al., *Parton distributions with LHC data*, Nucl. Phys. **B867** (2013) 244, arXiv: 1207.1303 [hep-ph] (cit. on p. 13).

[29] I. Nomidis et al., *Event selection, performance and background estimation in the $H \to \gamma\gamma$ channel with Run-2 data*, tech. rep., CERN, 2020, URL: https://cds.cern.ch/record/2718255 (cit. on pp. 17, 18, 20, 115).

[30] ATLAS Collaboration, *Jet reconstruction and performance using particle flow with the ATLAS Detector*, Eur. Phys. J. C **77** (2017) 466, arXiv: 1703.10485 [hep-ex] (cit. on p. 17).

[31] J. Adelman et al., *Measurement of fiducial and differential cross sections in the $H \to \gamma\gamma$ decay channel with 140fb^{-1} of 13 TeV proton–proton collision data with the ATLAS detector*, tech. rep. ATL-COM-PHYS-2019-035, CERN, 2019, URL: https://cds.cern.ch/record/2654897 (cit. on p. 17).

[32] A. Collaboration, *ATLAS Flavor-Tagging Calibration Results with 139 ifb*, 2019, URL: http://atlas.web.cern.ch/Atlas/GROUPS/PHYSICS/PLOTS/FTAG-2019-004/ (cit. on p. 18).

[33] A. Collaboration, *Expected performance of the 2019 ATLAS b-taggers*, 2019, URL: http://atlas.web.cern.ch/Atlas/GROUPS/PHYSICS/PLOTS/FTAG-2019-005/ (cit. on p. 18).

[34] ATLAS Collaboration, *Supporting Note: Selection and performance for the $H \to \gamma\gamma$ and $H \to Z\gamma$ analyses*, (2015), URL: https://cds.cern.ch/record/2196102 (cit. on p. 18).

[35] M. Aaboud et al., *Search for Higgs boson pair production in the $\gamma\gamma WW^*$ channel using pp collision data recorded at $\sqrt{s}$ = 13 TeV with the ATLAS detector*, The European Physical Journal C **78** (2018), ISSN: 1434-6052, URL: http://dx.doi.org/10.1140/epjc/s10052-018-6457-x (cit. on pp. 21, 44).

[36] G. Aad et al., *Searches for Higgs boson pair production in the $hh \to bb\tau\tau, \gamma\gamma WW^*, \gamma\gamma bb, bbbb$ channels with the ATLAS detector*, Phys. Rev. **D92** (2015) 092004, arXiv: 1509.04670 [hep-ex] (cit. on p. 21).

[37] A. Hoecker et al., *TMVA - Toolkit for Multivariate Data Analysis*, 2007, arXiv: physics/0703039 [physics.data-an] (cit. on p. 26).

[38] A. Hoecker, P. Speckmayer, J. Stelzer, J. Therhaag, E. von Toerne, and H. Voss, "TMVA 4 (Toolkit for Multivariate Data Analysis with ROOT) Users Guide," 2009 (cit. on p. 26).

[39] P. Baldi, K. Cranmer, T. Faucett, P. Sadowski, and D. Whiteson, *Parameterized neural networks for high-energy physics*, Eur. Phys. J. C **76** (2016) 235, arXiv: 1601.07913 [hep-ex] (cit. on p. 28).

[40] D. de Florian et al., *Handbook of LHC Higgs Cross Sections: 4. Deciphering the Nature of the Higgs Sector*, (2016), arXiv: 1610.07922 [hep-ph] (cit. on p. 50).

[41] ATLAS Collaboration, *Evaluation of theoretical uncertainties for simplified template cross section measurements of V-associated production of the Higgs boson*, ATL-PHYS-PUB-2018-035, 2018, URL: https://cds.cern.ch/record/2649241 (cit. on p. 51).

[42] M. Grazzini et al., *Higgs boson pair production at NNLO with top quark mass effects*, Journal of High Energy Physics **2018** (2018) 59, ISSN: 1029-8479, URL: https://doi.org/10.1007/JHEP05(2018)059 (cit. on p. 52).

[43] *LHCHXSWGHH*, URL: https://twiki.cern.ch/twiki/bin/view/LHCPhysics/LHCHWGHH?redirectedfrom=LHCPhysics.LHCHXSWGHH (cit. on p. 52).

[44] A. L. Read, *Presentation of search results: The CL(s) technique*, J.Phys. **G28** (2002) 2693 (cit. on p. 54).

[45] G. Cowan et al., *Asymptotic formulae for likelihood-based tests of new physics*, Eur. Phys. J. **C71** (2011) 1554, arXiv: 1007.1727 [physics.data-an] (cit. on p. 54).

Appendices

A Cutflow of signal samples

m_X	300	400	400	500	500	500	600	600	600	600
m_S	170	170	200	170	200	300	170	200	300	400
WW1l, DSID	800943	800944	800945	800946	800947	800948	800949	800950	800951	800952
All events	100	100	100	100	100	100	100	100	100	100
No duplicates	100	100	100	100	100	100	100	100	100	100
GRL	100	100	100	100	100	100	100	100	100	100
Pass trigger	77.56	82.25	81.14	88.92	88.45	83.35	91.86	91.69	90.37	84.82
Detector DQ	77.56	82.25	81.14	88.92	88.45	83.35	91.86	91.69	90.37	84.82
Has PV	77.56	82.25	81.14	88.92	88.45	83.35	91.86	91.69	90.37	84.82
2 loose photons	58.57	59.26	59.46	60.98	61.10	61.23	63.06	63.11	62.69	62.65
Trigger match	53.29	54.64	54.12	58.45	58.19	55.83	61.60	61.46	60.02	57.10
tight ID	45.04	46.47	46.07	49.67	49.36	47.09	52.24	52.01	50.49	47.84
isolation	36.73	39.99	38.98	44.28	43.61	39.70	47.45	46.98	44.37	40.26
rel. pT cuts	34.16	35.51	34.57	39.95	39.10	35.11	43.62	43.15	39.97	35.50
m_{yy} in [105, 160]GeV	33.81	35.18	34.16	39.51	38.59	34.34	43.21	42.64	39.11	34.43
b-veto	30.75	31.49	30.52	34.97	34.19	30.35	38.03	37.52	34.18	30.19
At least 1lep	19.32	19.81	20.30	21.27	22.71	20.67	21.92	24.46	23.73	20.55
pass WW1l	11.01	13.12	13.85	15.20	16.58	16.11	16.27	18.60	18.92	16.95
WW2l, DSID	800963	800964	800965	800966	800967	800968	800969	800970	800971	800972
All events	100	100	100	100	100	100	100	100	100	100
No duplicates	100	100	100	100	100	100	100	100	100	100
GRL	100	100	100	100	100	100	100	100	100	100
Pass trigger	84.51	87.68	87.25	91.92	91.75	89.45	93.83	93.99	93.39	91.03
Detector DQ	84.51	87.68	87.25	91.92	91.75	89.45	93.83	93.99	93.39	91.03
Has PV	84.51	87.68	87.25	91.92	91.75	89.45	93.83	93.99	93.39	91.03
2 loose photons	58.15	57.75	58.43	59.10	58.94	60.23	60.91	60.68	60.45	61.59
Trigger match	53.03	53.45	53.28	56.75	56.22	55.25	59.63	59.21	58.15	56.72
tight ID	45.22	45.74	45.55	48.59	48.07	47.34	50.94	50.69	49.77	48.45
isolation	38.12	39.65	39.06	43.23	42.55	40.57	45.96	45.60	43.99	41.37
rel. pT cuts	35.49	34.90	34.68	38.88	38.01	35.87	42.10	41.73	39.45	36.56
m_{yy} in [105, 160]GeV	34.79	34.22	33.88	38.02	36.96	34.43	41.17	40.68	37.95	34.67
b-veto	33.56	32.74	32.39	36.23	35.17	32.95	39.05	38.65	36.08	32.96
At least 2lep	17.14	18.06	18.12	20.55	20.72	19.45	22.16	23.23	22.35	20.15
pass WW2l	17.01	17.90	17.60	20.34	20.09	18.95	21.90	22.44	21.73	19.76
pass ZZ2l	0.07	0.10	0.43	0.13	0.52	0.40	0.14	0.65	0.46	0.23
WW2l-em	8.46	8.91	8.85	10.17	10.27	9.64	10.96	11.50	11.02	10.03
fall to 1lepton category	11.93	10.51	10.99	11.07	11.14	10.93	11.54	11.82	11.33	10.58
ZZ2l, DSID	800983	800984	800985	800986	800987	800988	800989	800990	800991	800992
All events	100	100	100	100	100	100	100	100	100	100
No duplicates	100	100	100	100	100	100	100	100	100	100
GRL	100	100	100	100	100	100	100	100	100	100
Pass trigger	77.68	81.12	80.26	87.03	86.52	81.65	89.98	89.82	88.24	82.69
Detector DQ	77.68	81.12	80.26	87.03	86.52	81.65	89.98	89.82	88.24	82.69
Has PV	77.68	81.12	80.26	87.03	86.52	81.65	89.98	89.82	88.24	82.69
2 loose photons	53.42	53.66	54.13	54.92	55.21	55.79	56.92	57.19	56.96	57.33
Trigger match	48.43	49.46	49.14	52.63	52.49	50.88	55.57	55.65	54.47	52.29
tight ID	40.75	41.91	41.52	44.61	44.41	42.81	46.87	46.93	45.85	43.71
isolation	32.83	35.78	34.68	39.36	38.81	35.77	42.31	42.05	39.74	36.32
rel. pT cuts	30.54	31.61	30.81	35.43	34.77	31.78	38.92	38.53	35.90	32.00
m_{yy} in [105, 160]GeV	29.93	30.98	30.14	34.67	33.94	30.73	38.17	37.69	34.73	30.70
b-veto	25.04	24.53	23.71	26.65	25.77	22.89	28.65	28.14	25.25	21.89
At least 2lep	12.82	12.97	12.87	13.79	13.86	13.75	14.16	14.69	15.67	13.50
pass WW2l	10.13	9.66	6.13	9.94	6.21	5.69	9.99	6.26	6.18	5.16
pass ZZ2l	2.64	3.24	6.68	3.77	7.60	7.99	4.08	8.35	9.40	8.25
WW2l-em	0.07	0.09	0.08	0.09	0.09	0.13	0.11	0.11	0.14	0.11
fall to 1lepton category	8.52	8.06	7.69	8.76	8.32	6.26	9.56	9.20	6.33	5.53

Table 23: Efficiencies in percent for event selection for signals.

X	750	750	750	750	750	1000	1000	1000	1000	1000
S	170	200	300	400	500	170	200	300	400	500
WW1l, DSID	800953	800954	800955	800956	800957	800938	800939	800940	800941	800942
All events	100	100	100	100	100	100	100	100	100	100
No duplicates	100	100	100	100	100	100	100	100	100	100
GRL	100	100	100	100	100	100	100	100	100	100
Pass trigger	93.90	93.92	93.60	92.95	90.06	95.70	95.56	95.69	95.69	95.31
Detector DQ	93.90	93.92	93.60	92.95	90.06	95.70	95.56	95.69	95.69	95.31
Has PV	93.90	93.92	93.60	92.95	90.06	95.70	95.56	95.69	95.69	95.31
2 loose photons	66.12	65.98	65.50	64.81	63.87	70.26	70.03	69.93	69.35	68.60
Trigger match	65.35	65.15	64.43	63.04	60.41	69.85	69.62	69.50	68.81	67.87
tight ID	55.30	55.05	54.46	52.80	50.27	59.30	58.99	58.67	58.08	56.94
isolation	51.01	50.75	49.51	46.92	43.19	55.65	55.44	54.89	53.74	51.84
rel. pT cuts	47.92	47.61	46.04	43.00	38.47	53.12	52.95	52.20	50.81	48.79
m_{yy} in [105, 160]GeV	47.57	47.12	45.22	41.89	37.09	52.87	52.51	51.55	49.92	47.62
b-veto	41.45	41.08	39.16	36.33	32.17	45.53	45.14	44.30	42.94	40.86
1lep	21.69	25.62	27.08	24.90	21.87	19.71	25.60	30.14	29.57	27.95
pass WW1l	16.62	20.31	22.32	20.98	18.68	15.49	20.95	25.37	25.19	24.01
WW2l, DSID	800973	800974	800975	800976	800977	800958	800959	800960	800961	800962
All events	100	100	100	100	100	100	100	100	100	100
No duplicates	100	100	100	100	100	100	100	100	100	100
GRL	100	100	100	100	100	100	100	100	100	100
Pass trigger	95.43	95.31	95.49	95.37	94.10	96.61	96.77	96.84	96.88	96.82
Detector DQ	95.43	95.31	95.49	95.37	94.10	96.61	96.77	96.84	96.88	96.82
Has PV	95.43	95.31	95.49	95.37	94.10	96.61	96.77	96.84	96.88	96.82
2 loose photons	63.62	63.33	63.21	62.85	62.67	67.11	67.07	67.16	66.86	66.30
Trigger match	62.94	62.62	62.21	61.51	59.53	66.77	66.70	66.76	66.37	65.70
tight ID	53.72	53.75	53.21	52.64	50.85	57.43	57.28	57.33	56.91	56.27
isolation	49.43	49.29	48.39	47.13	44.22	53.56	53.49	53.36	52.56	51.50
rel. pT cuts	46.18	46.00	44.78	42.90	39.40	50.90	50.75	50.38	49.46	48.15
m_{yy} in [105, 160]GeV	45.32	44.96	43.35	40.95	37.02	50.16	49.81	49.12	47.84	46.02
b-veto	42.79	42.47	41.01	38.49	35.14	46.94	46.63	46.05	44.92	43.22
At least 2lep	23.96	25.67	26.20	24.56	22.24	24.54	28.04	29.91	29.17	28.33
pass WW2l	23.65	24.75	25.38	24.11	21.87	24.14	26.97	28.89	28.49	27.84
pass ZZ2l	0.17	0.74	0.63	0.29	0.16	0.22	0.86	0.80	0.42	0.22
WW2l-em	11.90	12.65	12.93	12.22	11.08	12.22	13.90	14.75	14.40	14.12
fall to 1lepton category	12.27	12.52	12.14	11.62	10.76	13.54	13.04	12.99	12.88	12.34
ZZ2l, DSID	800993	800994	800995	800996	800997	800978	800979	800980	800981	800982
All events	100	100	100	100	100	100	100	100	100	100
No duplicates	100	100	100	100	100	100	100	100	100	100
GRL	100	100	100	100	100	100	100	100	100	100
Pass trigger	92.35	92.38	91.98	90.73	87.54	94.41	94.56	94.45	94.11	93.63
Detector DQ	92.35	92.38	91.98	90.73	87.54	94.41	94.56	94.45	94.11	93.63
Has PV	92.35	92.38	91.98	90.73	87.54	94.41	94.56	94.45	94.11	93.63
2 loose photons	59.89	60.04	59.63	59.11	58.35	63.46	63.58	63.61	63.33	62.62
Trigger match	59.27	59.25	58.55	57.46	55.16	63.09	63.17	63.14	62.80	61.87
tight ID	49.98	50.14	49.17	48.08	45.78	53.39	53.43	53.22	52.85	51.68
isolation	45.90	46.00	44.42	42.29	38.80	49.83	49.88	49.41	48.66	46.80
rel. pT cuts	42.91	42.97	41.25	38.70	34.58	47.48	47.40	46.85	46.02	43.98
m_{yy} in [105, 160]GeV	42.22	42.23	40.22	37.43	33.09	46.95	46.78	45.99	44.92	42.68
b-veto	30.66	30.57	28.53	26.06	22.68	33.10	32.64	31.58	30.64	28.72
At least 2lep	13.68	14.63	17.85	16.51	14.55	12.22	13.08	19.37	19.46	18.42
pass WW2l	9.64	6.18	6.58	5.93	5.20	8.72	5.85	6.76	6.58	6.17
pass ZZ2l	3.95	8.36	11.15	10.48	9.25	3.39	7.12	12.48	12.72	12.14
WW2l-em	0.11	0.13	0.17	0.18	0.16	0.12	0.10	0.20	0.21	0.21
fall to 1lepton category	10.88	10.59	6.77	5.98	5.06	12.07	12.17	7.12	6.21	5.84

Table 24: Efficiencies in percent for event selection for signals.(Continued)

B Pythia8 for signals

Here, the script used for generating SH model WW 1lepton channel at the mass point of X 400 GeV, S 200 GeV is given. The scriptes for other mass points, and other decays, are basically the same.

```
include("Pythia8_i/Pythia8_A14_NNPDF23LO_EvtGen_Common.py")
evgenConfig.generators = ["Pythia8", "EvtGen"]
evgenConfig.process     = "gg->X->SH->WW+yy, 1 lepton"
evgenConfig.description = "Generation of gg > X > SH where S decays to W+W- with 1 leptor
evgenConfig.keywords = ["BSMHiggs"]

genSeq.Pythia8.Commands += ['Higgs:useBSM = on',
                            'ParticleDecays:mSafety = 0.0',
                            'HiggsBSM:gg2A3 = on',
                            'HiggsA3:parity = 1',
                            'Higgs:clipWings = off',
                            '36:m0 = 400.0',
                            '36:mWidth = 0.01',
                            '36:doForceWidth = yes',
                            '36:addChannel = 1 1 100 25 35',
                            '36:onMode = off',
                            '36:onIfMatch = 25 35',
                            '36:mayDecay = on',
                            '35:mMin = 50.0',
                            '25:mMin = 50.0',
                            '35:m0 = 200.0',
                            '35:mWidth = 0.01',
                            '35:doForceWidth = yes',
                            '25:onMode = off',
                            '25:onIfMatch = 22 22',
                            '35:onMode = off',
                            '35:onIfMatch = 24 -24',
                            ]


from GeneratorFilters.GeneratorFiltersConf import MultiLeptonFilter
filtSeq += MultiLeptonFilter("LepOneFilter")
filtSeq.LepOneFilter.NLeptons = 1
filtSeq.LepOneFilter.Ptcut = 7000
filtSeq.LepOneFilter.Etacut = 3

filtSeq += MultiLeptonFilter("LepTwoFilter")
filtSeq.LepTwoFilter.NLeptons = 2
filtSeq.LepTwoFilter.Ptcut = 7000
filtSeq.LepTwoFilter.Etacut = 3
filtSeq.Expression = "LepOneFilter and not LepTwoFilter"
```

C MC Reweighting

The discrenpancy between continuum MC and data sideband data includes both yields and shape difference. If the cross section of all 3 MC processes, $\gamma\gamma + jets$, $V\gamma\gamma$ and $t\bar{t}\gamma\gamma$ follow the SM prediction, the sideband yields compared to the sideband data shown in the Figure 30.

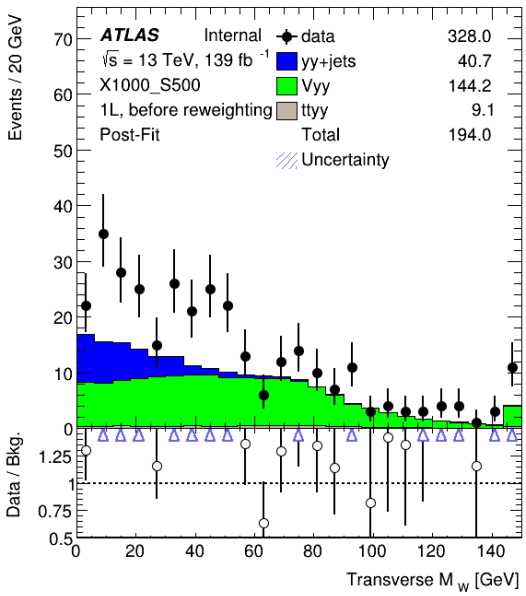

Figure 30: m_T^{W1} distribution for $\gamma\gamma + jets$, $V\gamma\gamma$ and $t\bar{t}\gamma\gamma$ processes and the sideband data.

For the yields difference, to simplify the situation, the ratio between 3 MC processes are fixed and these are scaled by 1.69. In the same way, 2 lepton channels are scaled with 1.04. With the scaling, the yields consistency between MC and sideband data is confirmed.

To further mimic the deviation, the bin by bin reweighting on m_T^{W1} distribution is done, as described in Figure 6. Other kinematic distributions are shown in the followiing Figure 31 to 42.

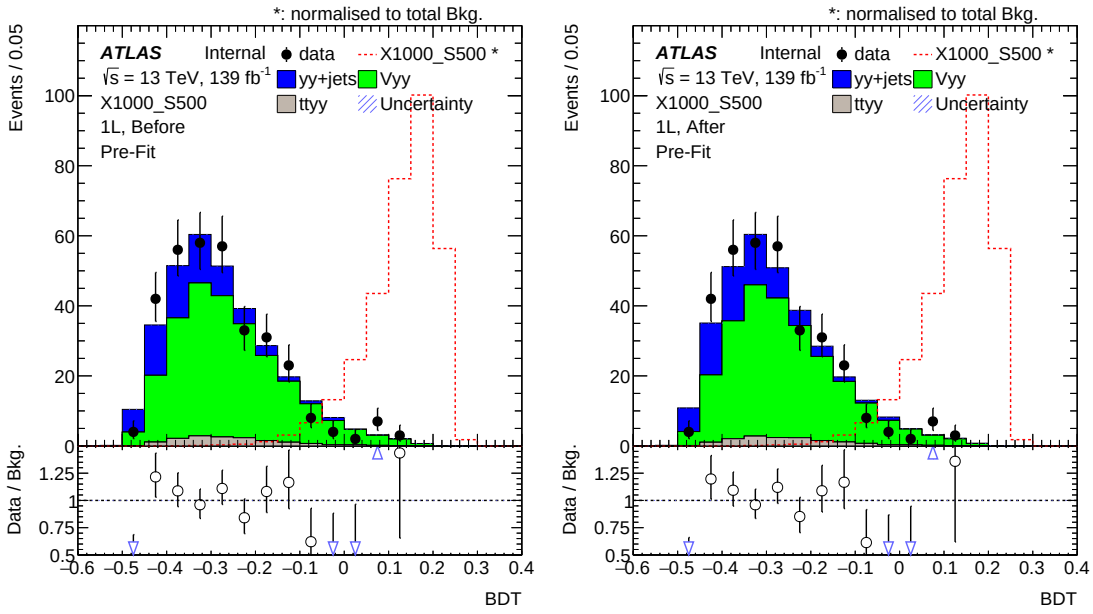

(a)

(b)

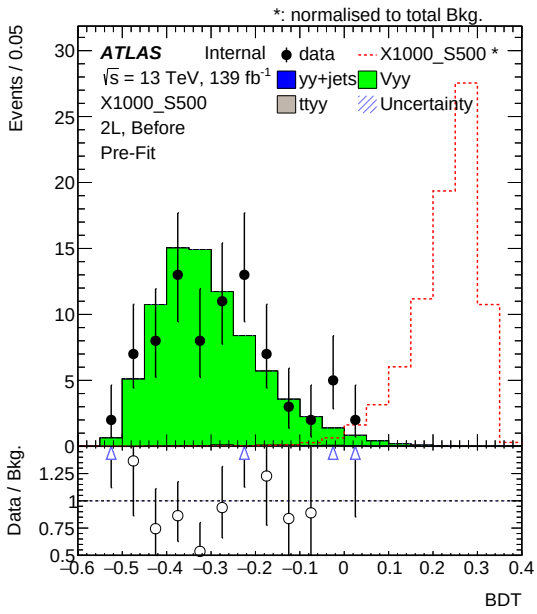

(c)

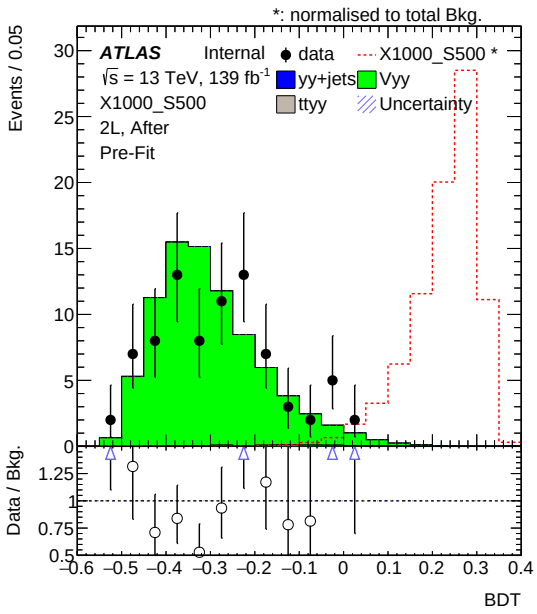

(d)

Figure 31: BDT distribution for continuum MC and the sideband data before(left) and after(right) background reweighting.

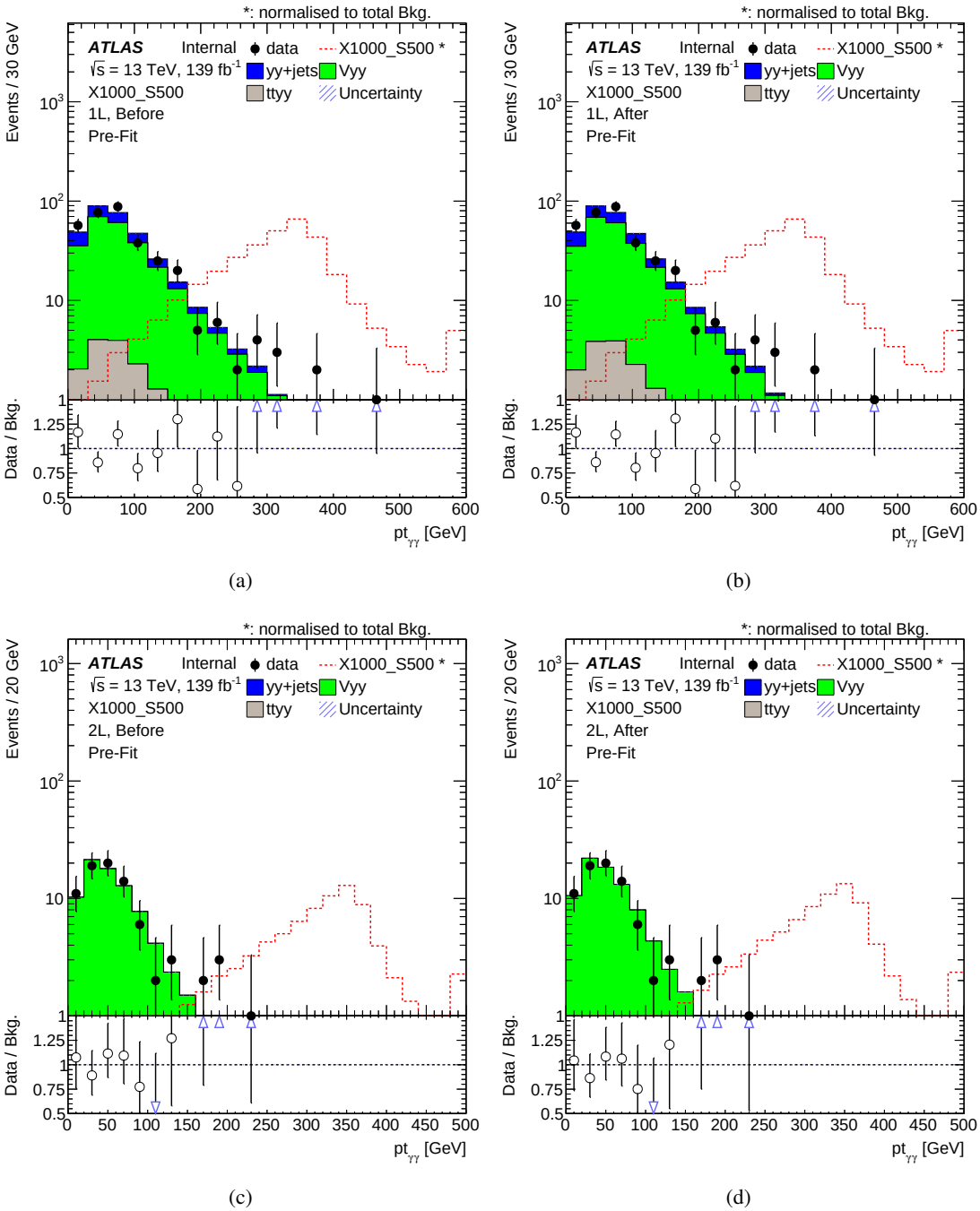

Figure 32: $p_{\mathrm{T}}(\gamma\gamma)$ distribution for continuum MC and the sideband data before(left) and after(right) background reweighting.

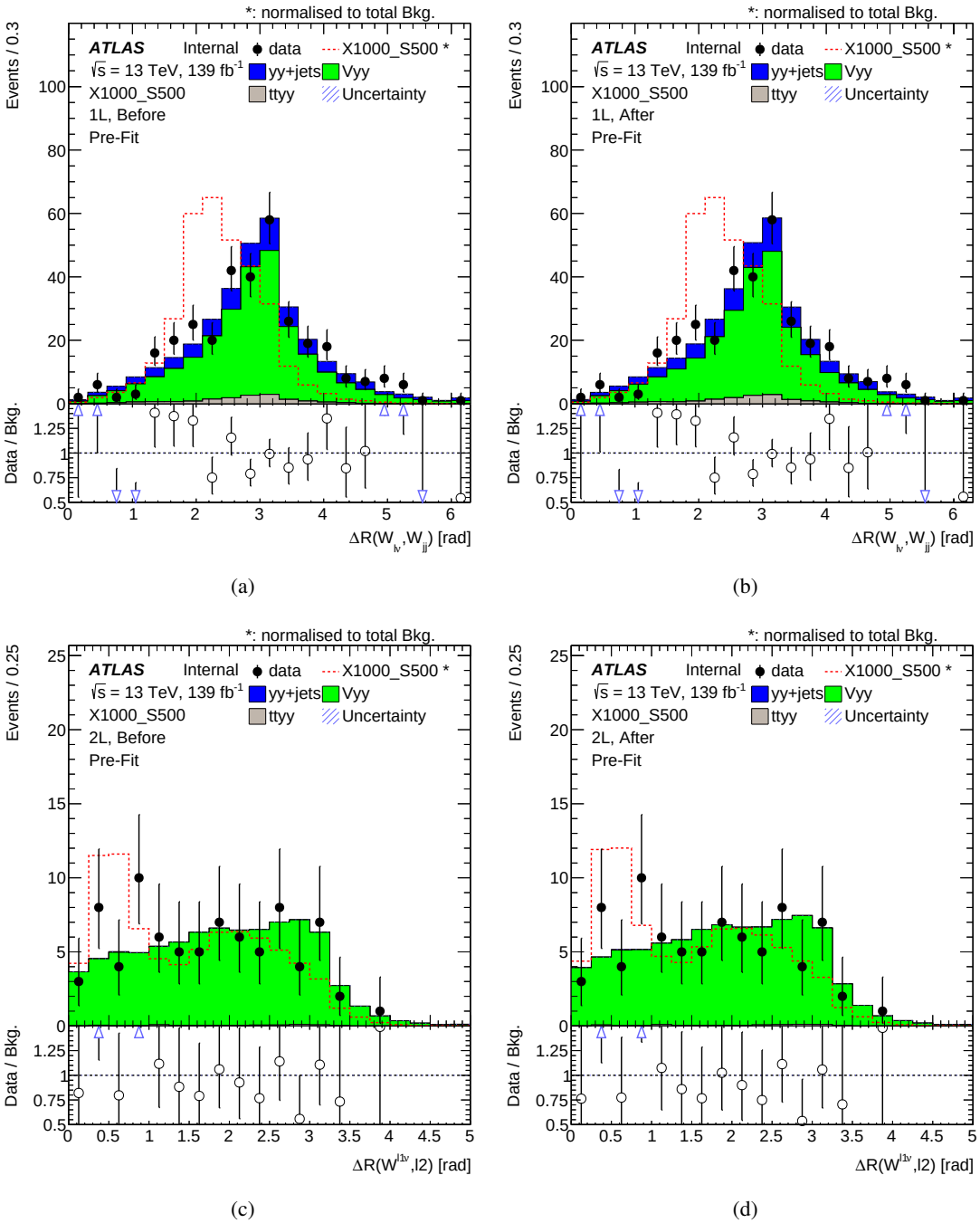

Figure 33: $\Delta R(W1, W2)$ distribution for continuum MC and the sideband data before(left) and after(right) background reweighting.

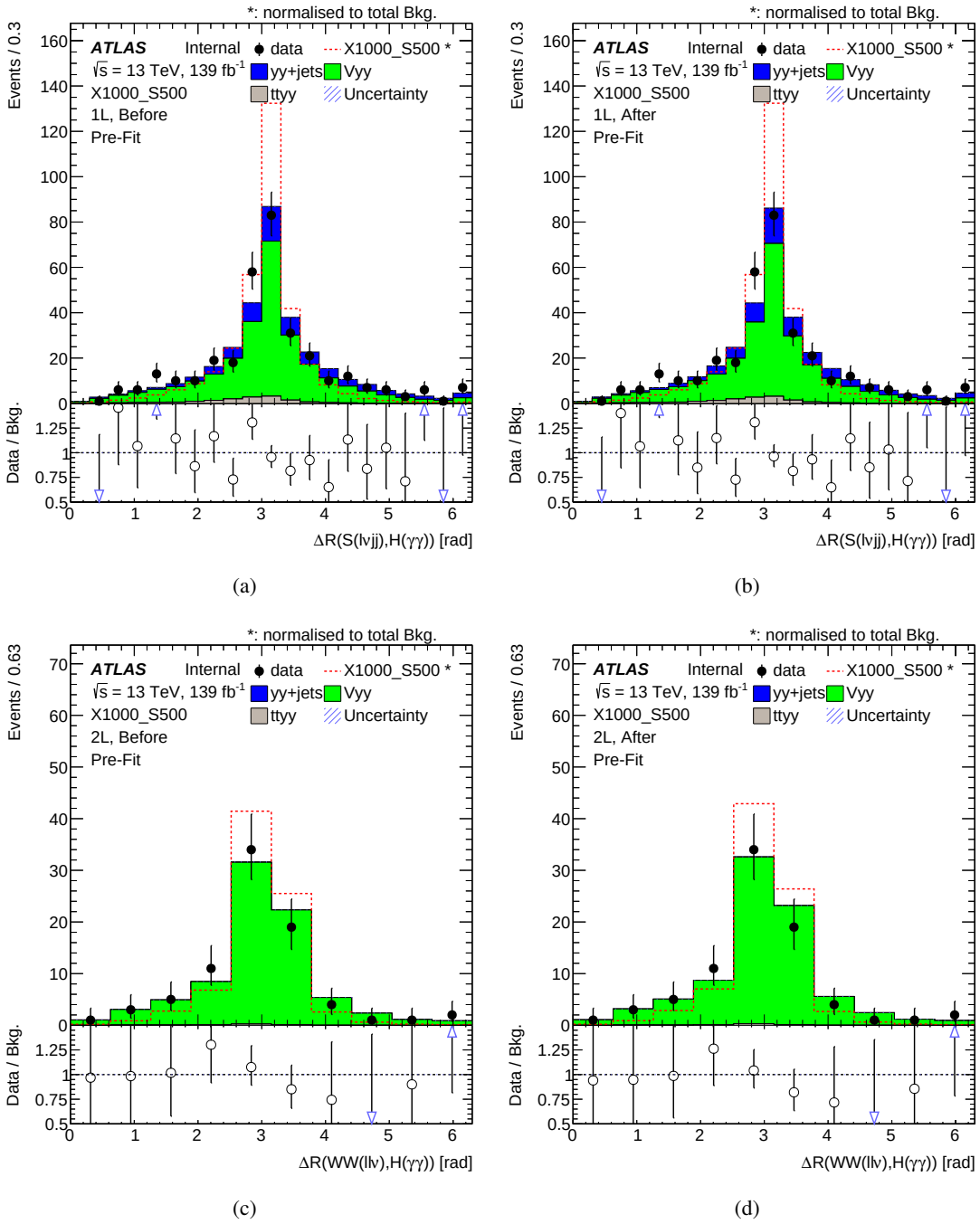

Figure 34: $\Delta R(WW, H)$ distribution for continuum MC and the sideband data before(left) and after(right) background reweighting.

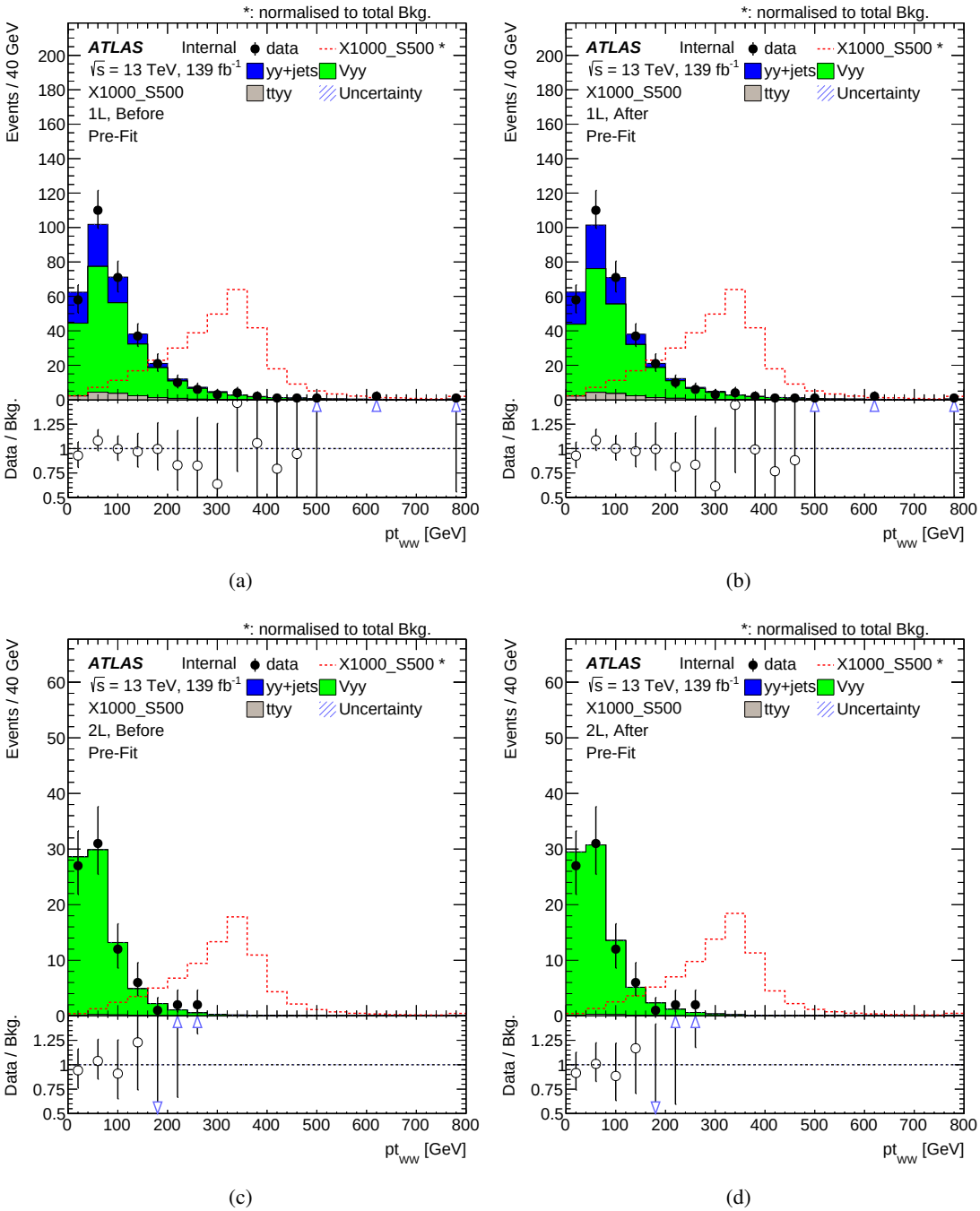

Figure 35: $p_{\mathrm{T}}(WW)$ distribution for continuum MC and the sideband data before(left) and after(right) background reweighting.

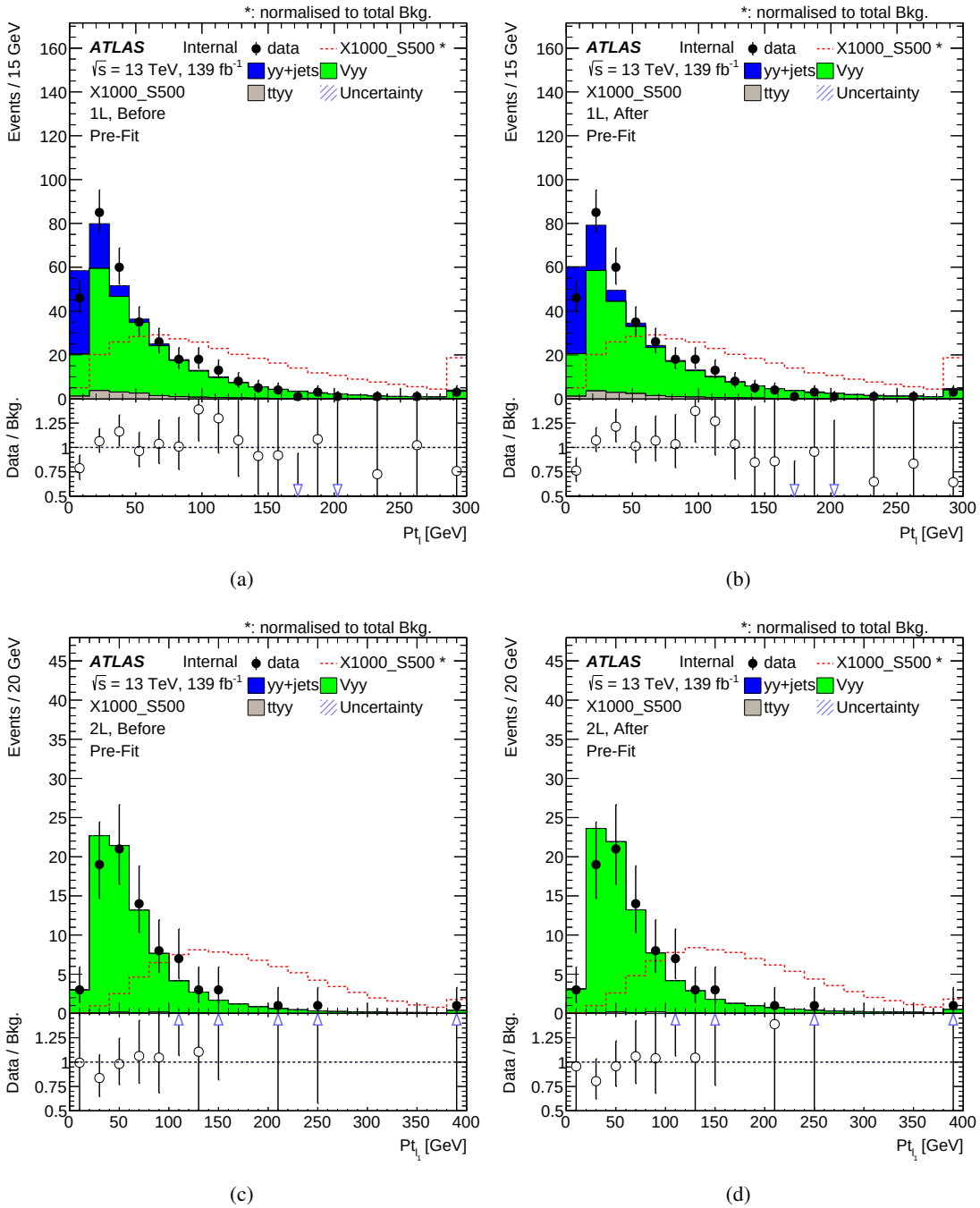

Figure 36: $p_{\mathrm{T}}(l1)$ distribution for continuum MC and the sideband data before(left) and after(right) background reweighting.

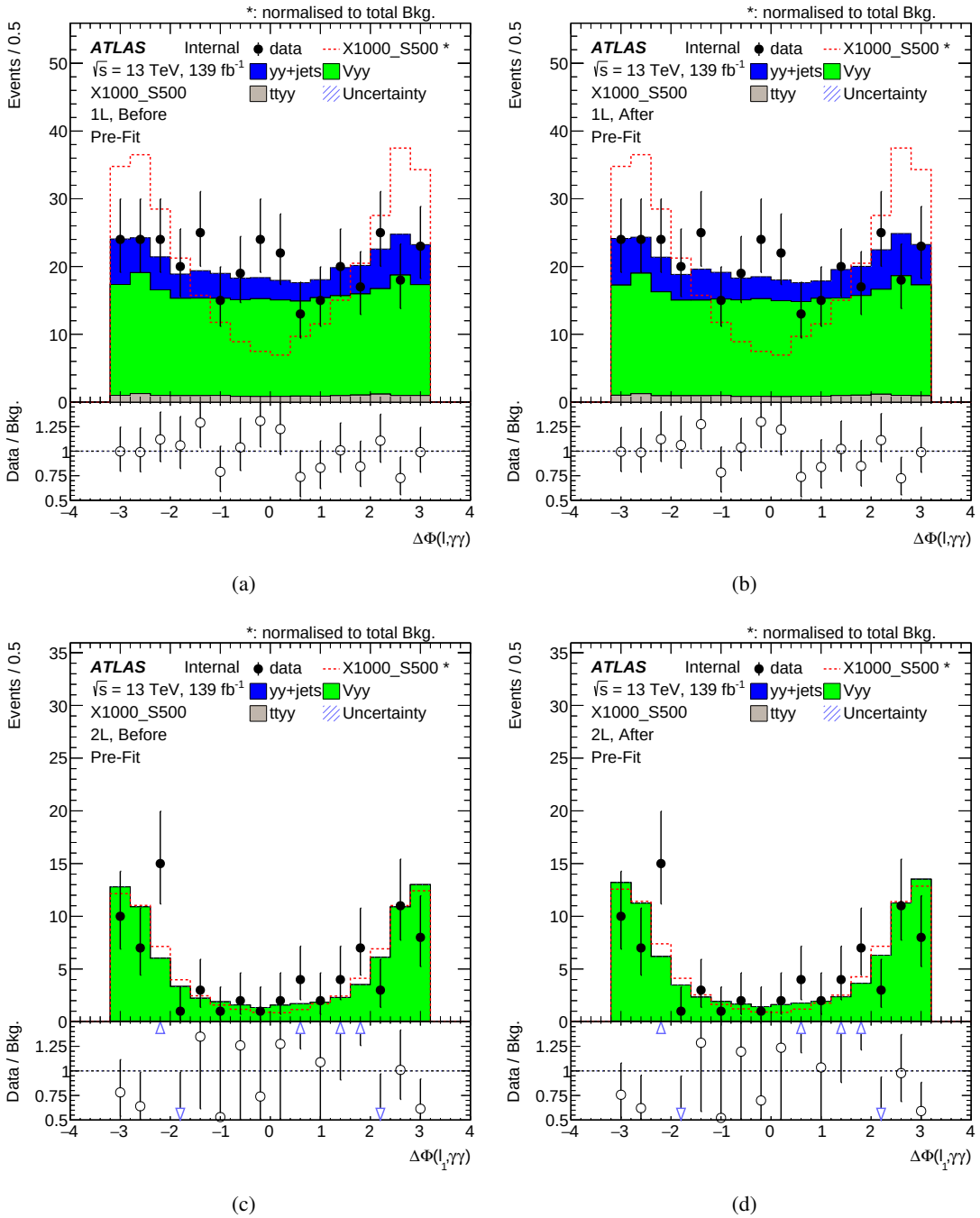

Figure 37: $\Delta\Phi(\gamma\gamma, \ell_1)$ distribution for continuum MC and the sideband data before(left) and after(right) background reweighting.

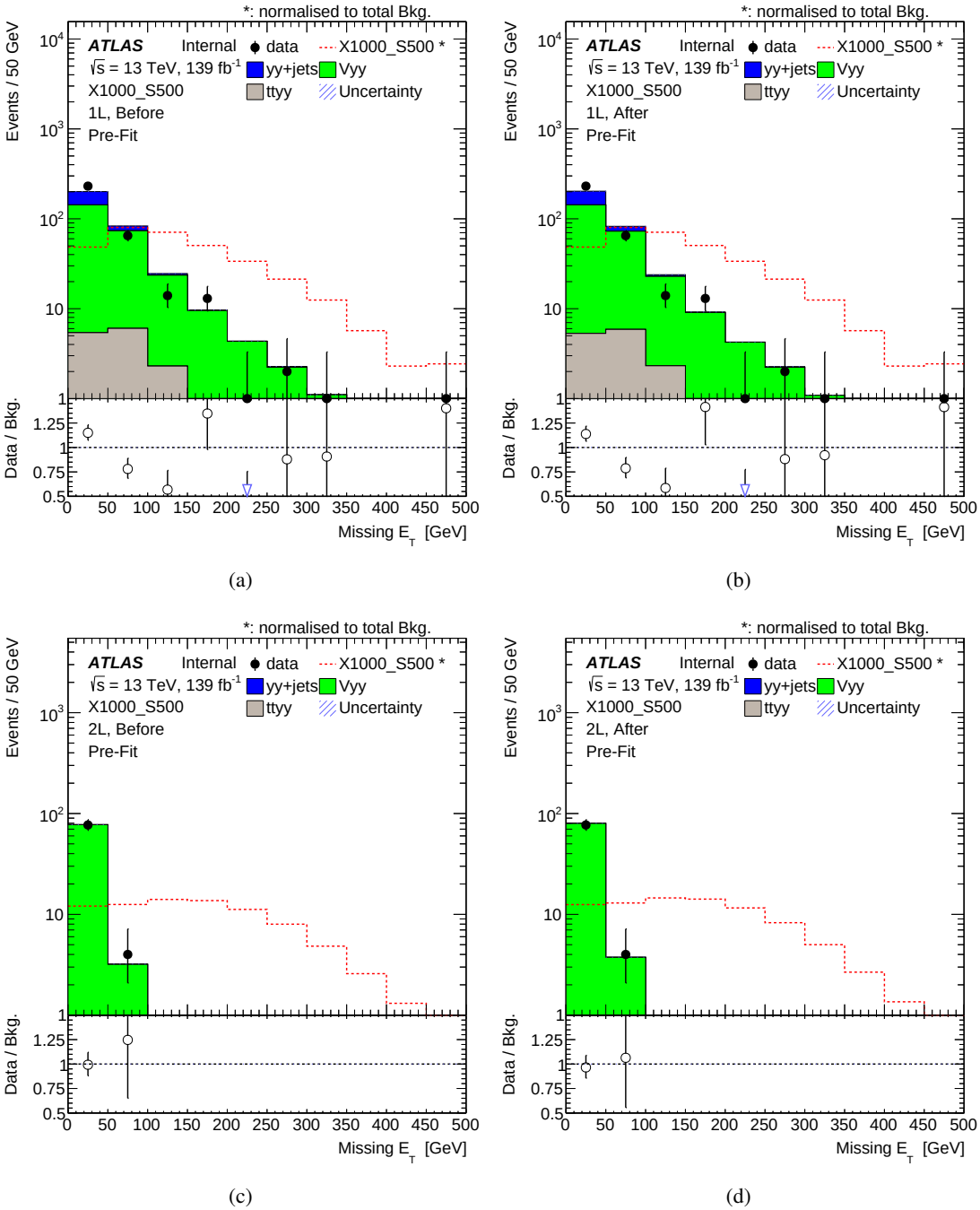

Figure 38: $E_{\mathrm{T}}^{\mathrm{miss}}$ distribution for continuum MC and the sideband data before(left) and after(right) background reweighting.

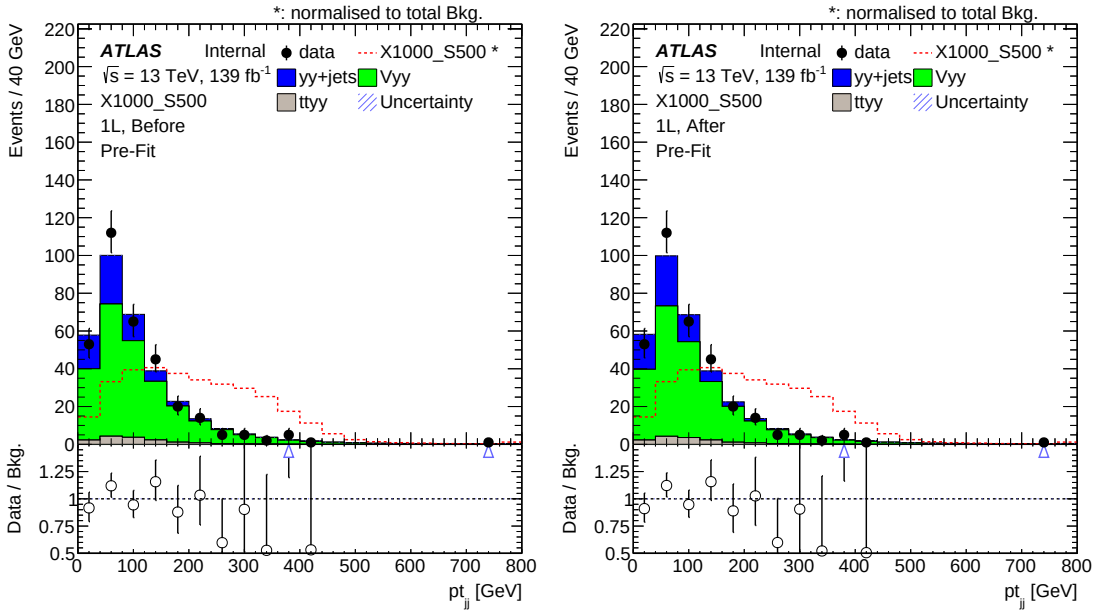

(a) (b)

Figure 39: $p_{\mathrm{T}}(jj)$ distribution for 1l continuum MC and the sideband data before(left) and after(right) background reweighting.

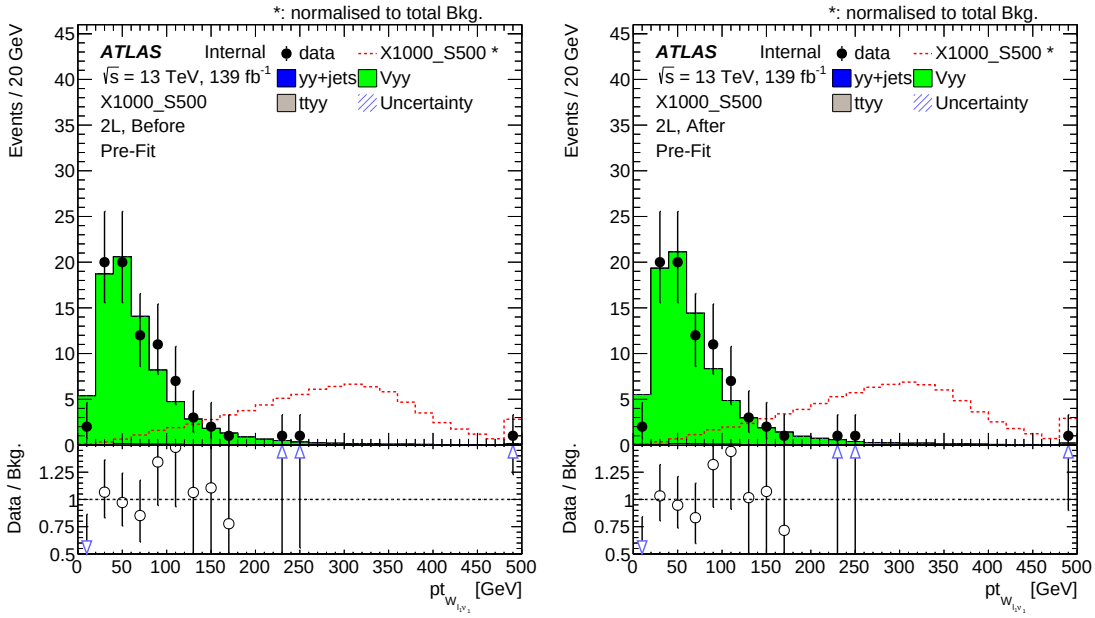

(a) (b)

Figure 40: $p_{\mathrm{T}}(l\nu)$ distribution for 2l continuum MC and the sideband data before(left) and after(right) background reweighting.

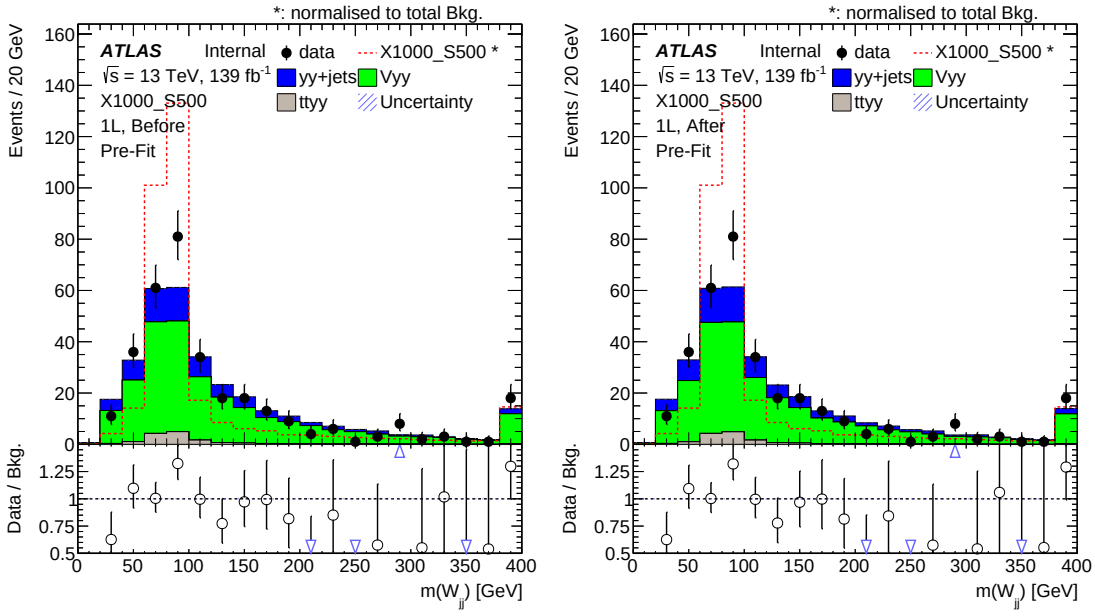

(a) (b)

Figure 41: $M(jj)$ distribution for 1l continuum MC and the sideband data before(left) and after(right) background reweighting.

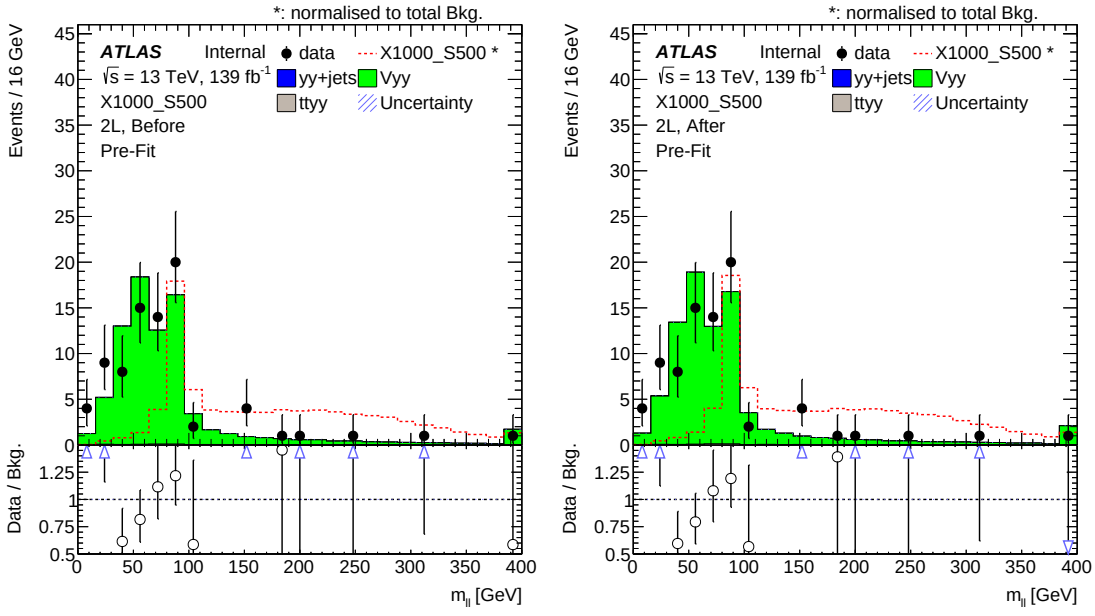

(a) (b)

Figure 42: $m(ll)$ distribution for 2l continuum MC and the sideband data before(left) and after(right) background reweighting.

D BDT training in all mass points

D.1 WW1l category

D.1.1 m_S = 170 GeV

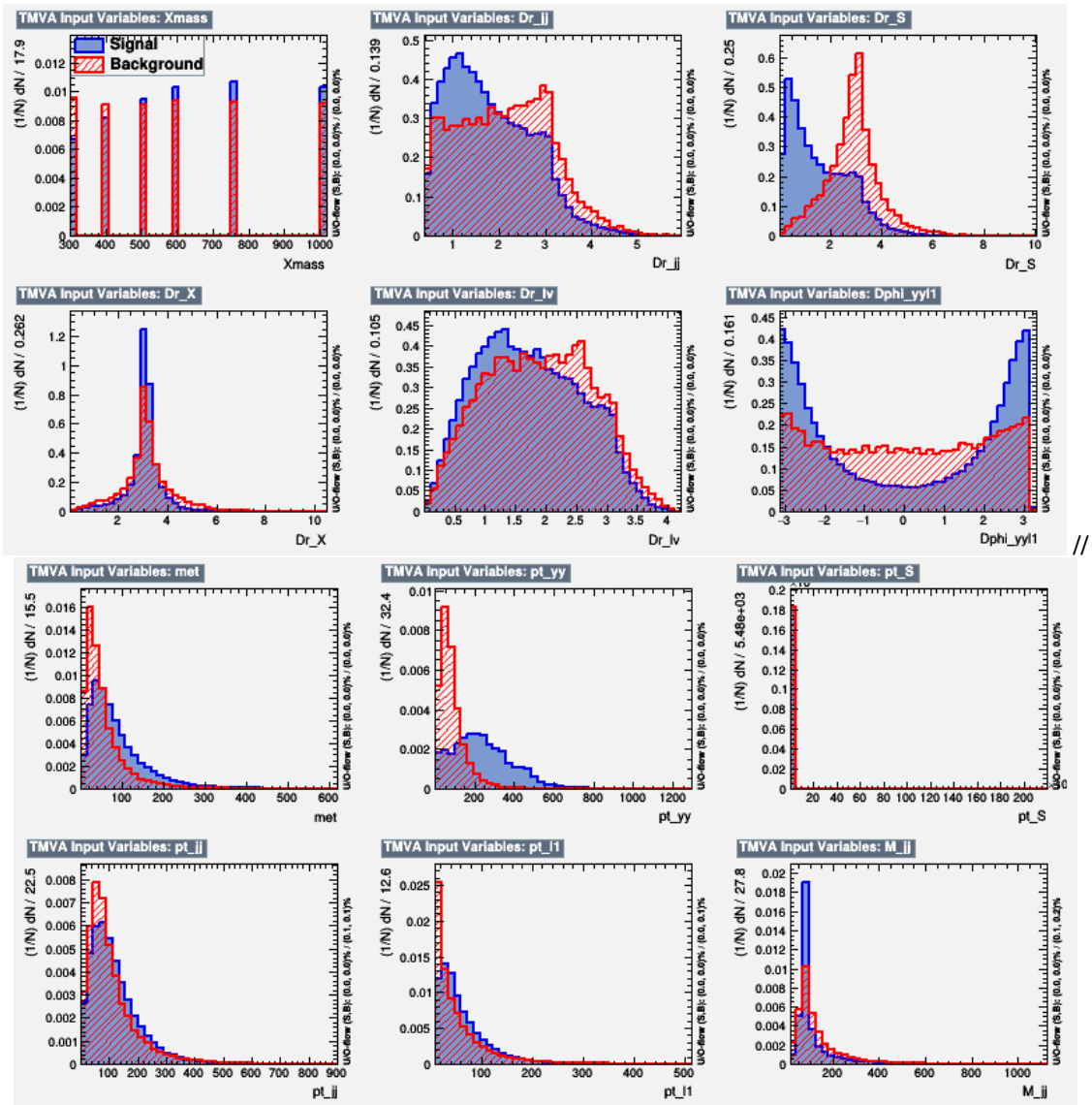

Figure 43: Input variables for BDT in WW1l category.

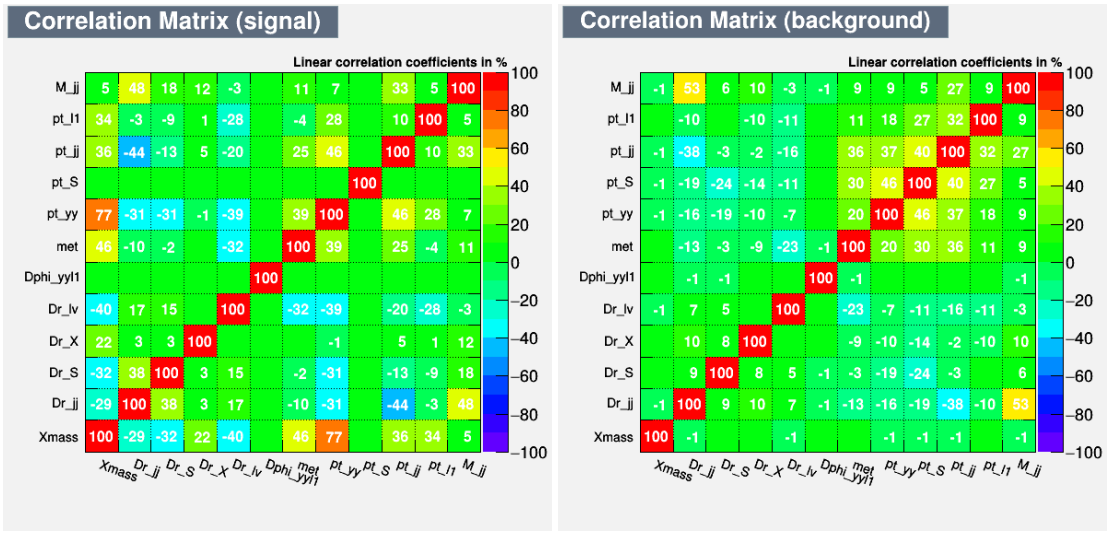

(a) Signal (b) Background

Figure 44: Input variables' correlation in WW1l category.

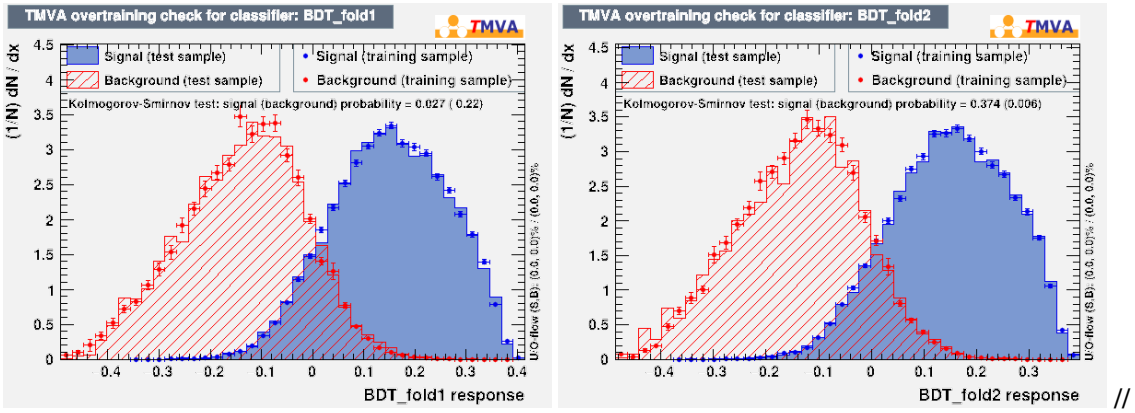

(a) fold1 (b) fold2

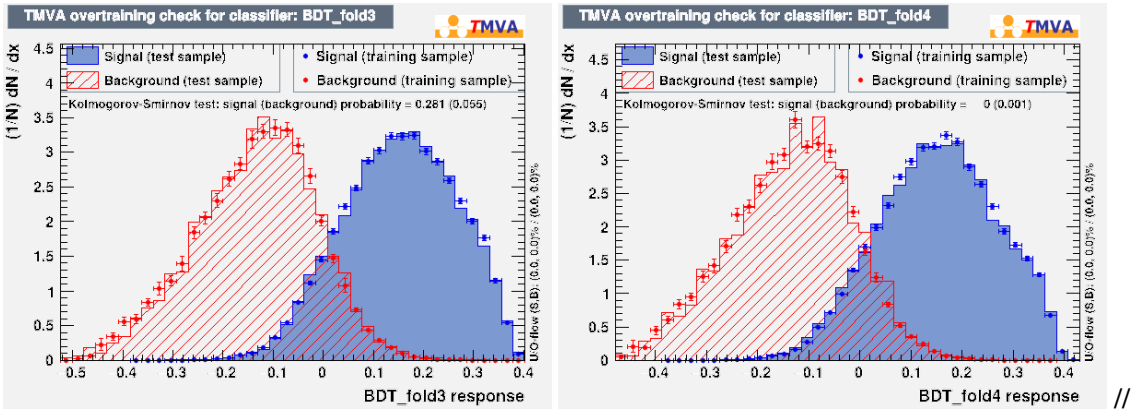

(c) fold3 (d) fold4

Figure 45: BDT distributions for training and test templates in 4 folds

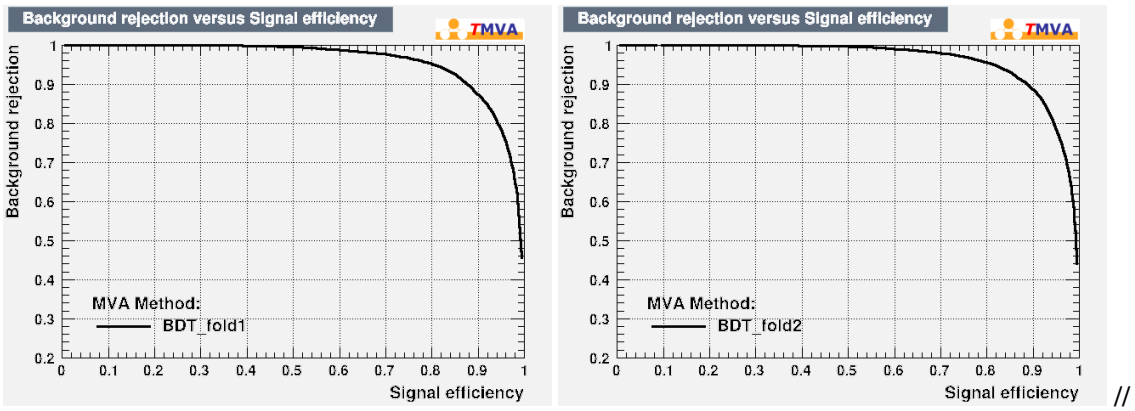

(a) fold1 (b) fold2

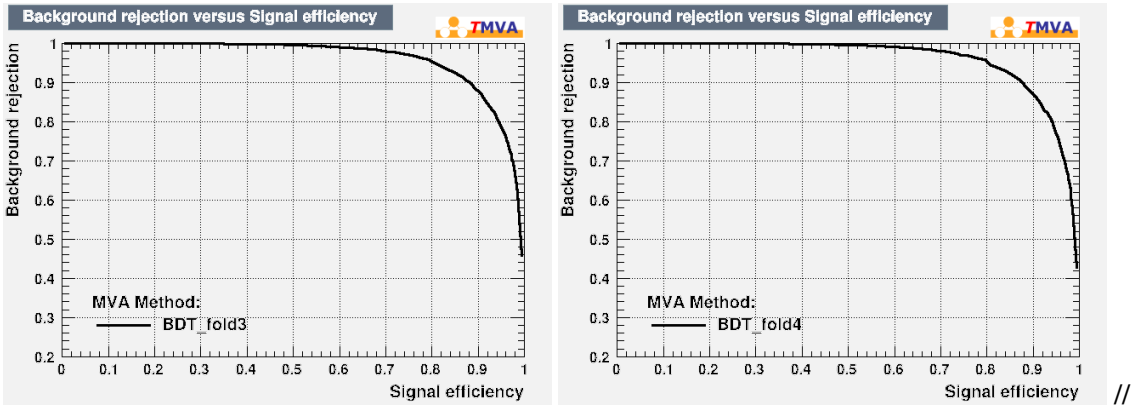

(c) fold3 (d) fold4

Figure 46: Trainned BDT ROC in 4 folds

D.1.2 m_S = 200 GeV

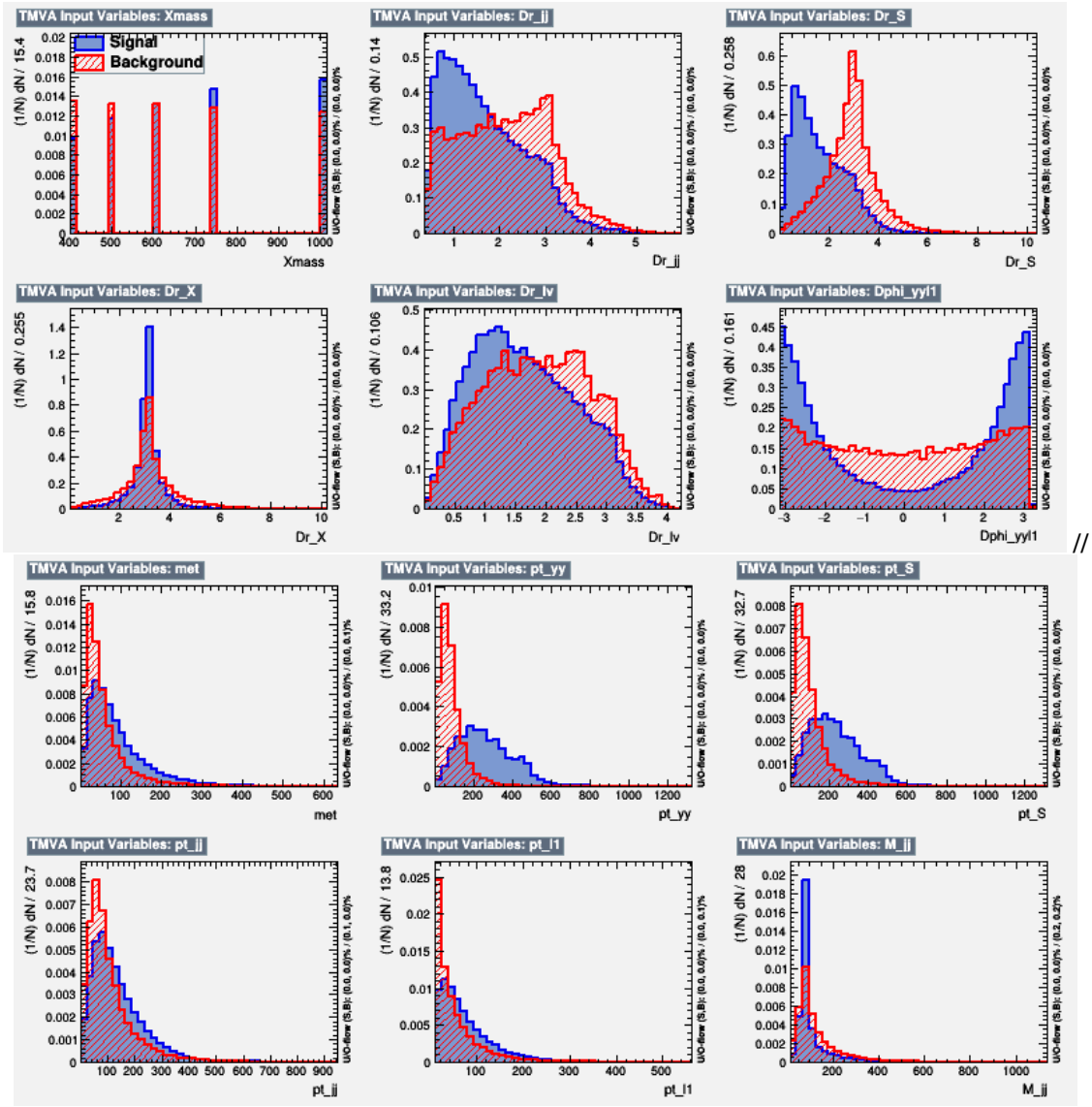

Figure 47: Input variables for BDT in WW1l category.

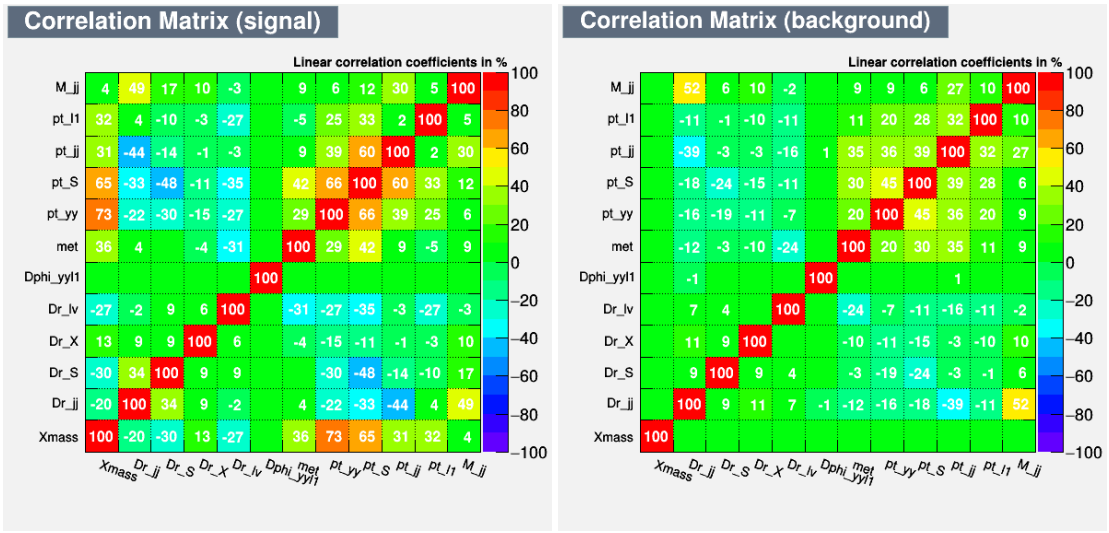

(a) Signal (b) Background

Figure 48: Input variables' correlation in WW1l category.

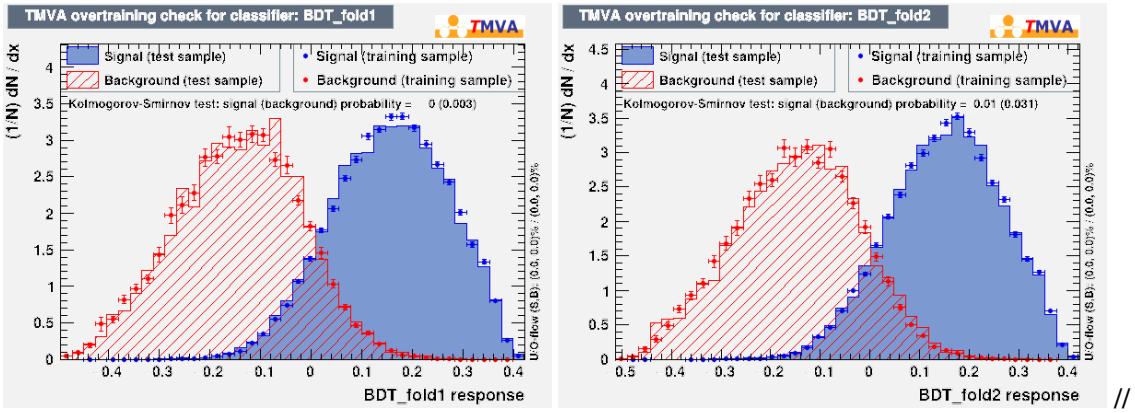

(a) fold1 (b) fold2

(c) fold3 (d) fold4

Figure 49: BDT distributions for training and test templates in 4 folds

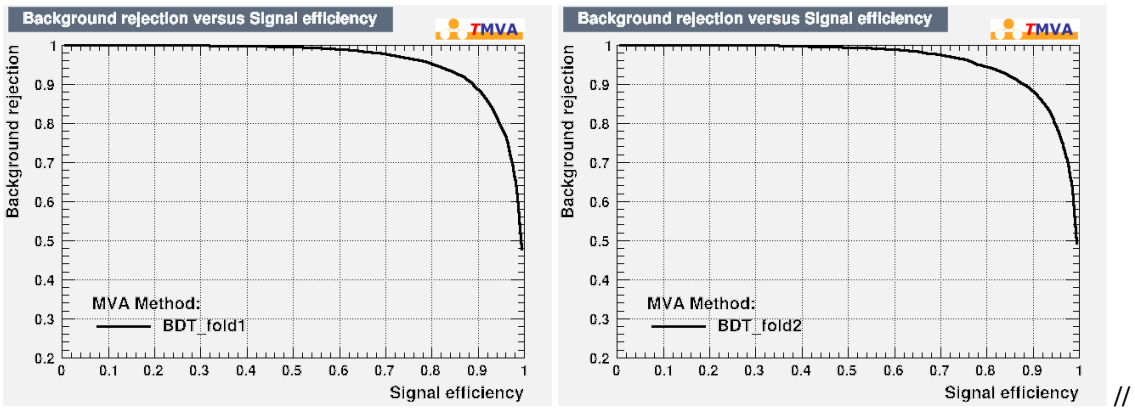

(a) fold1 (b) fold2

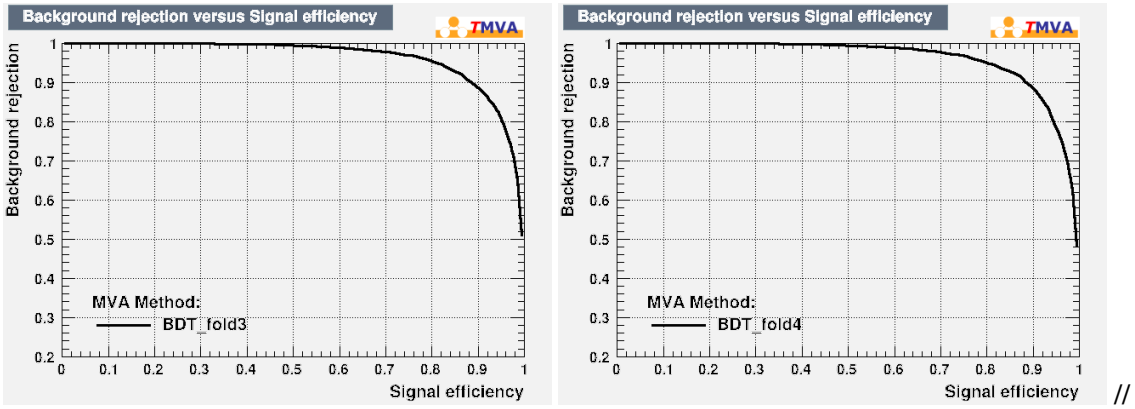

(c) fold3 (d) fold4

Figure 50: Trainned BDT ROC in 4 folds

D.1.3 m_S = 300 GeV

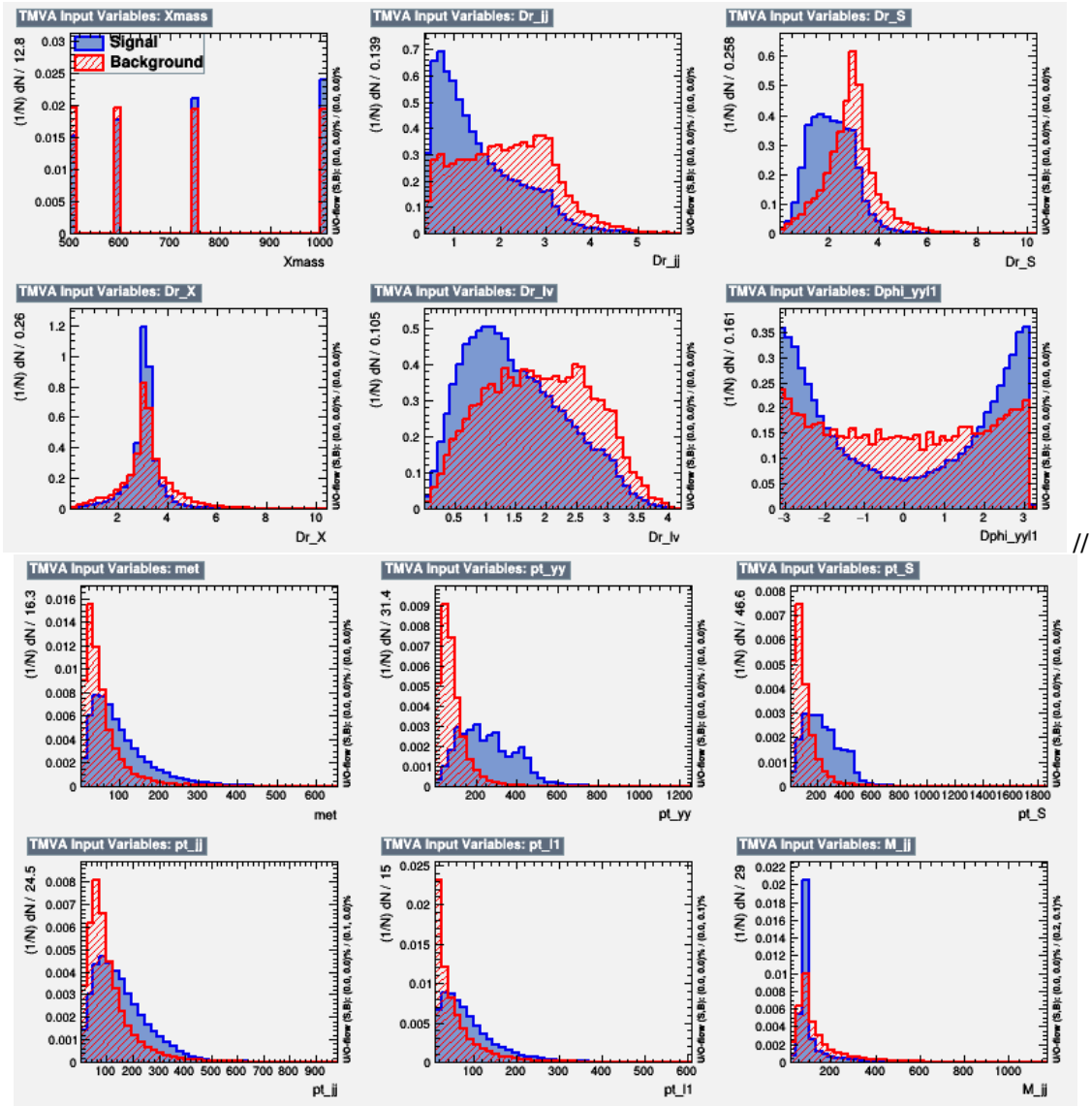

Figure 51: Input variables for BDT in WW1l category.

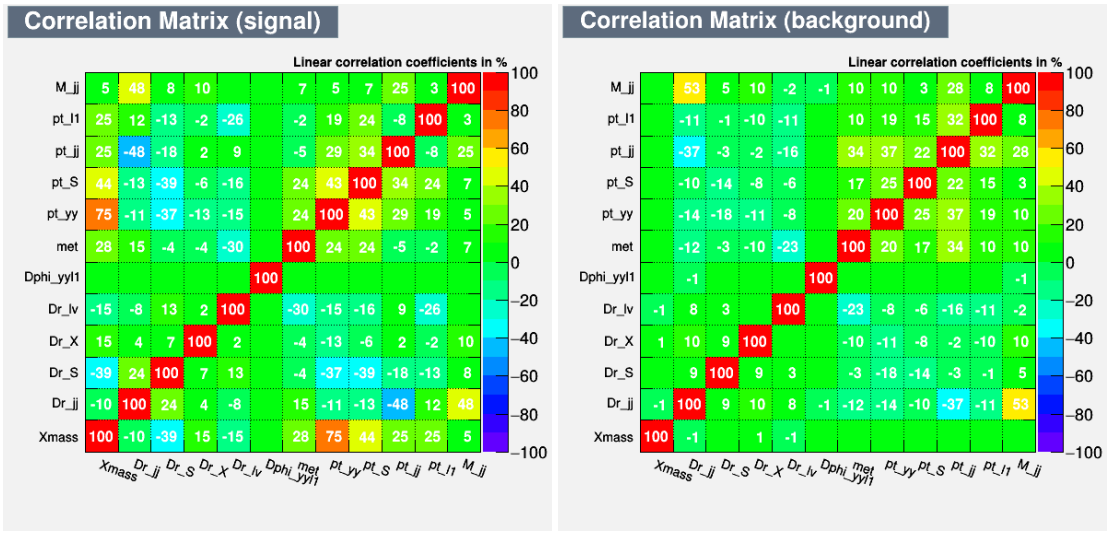

(a) Signal (b) Background

Figure 52: Input variables' correlation in WW1l category.

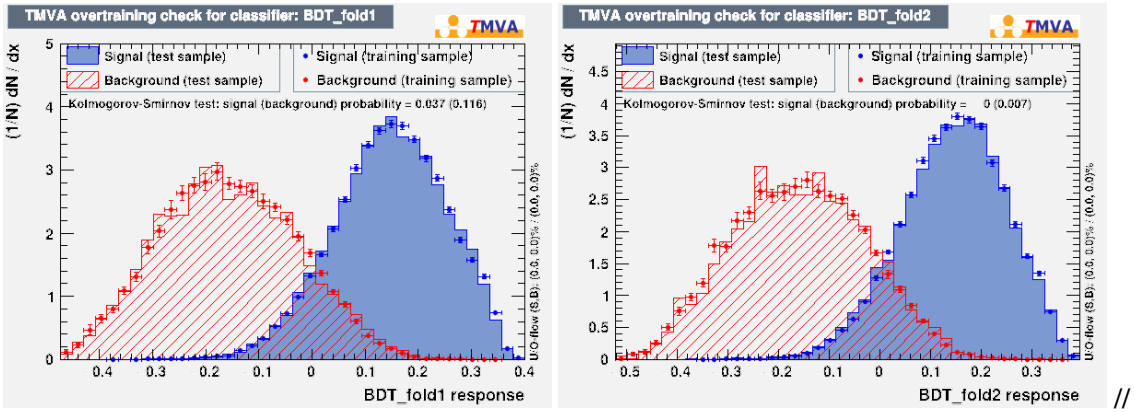

(a) fold1 (b) fold2

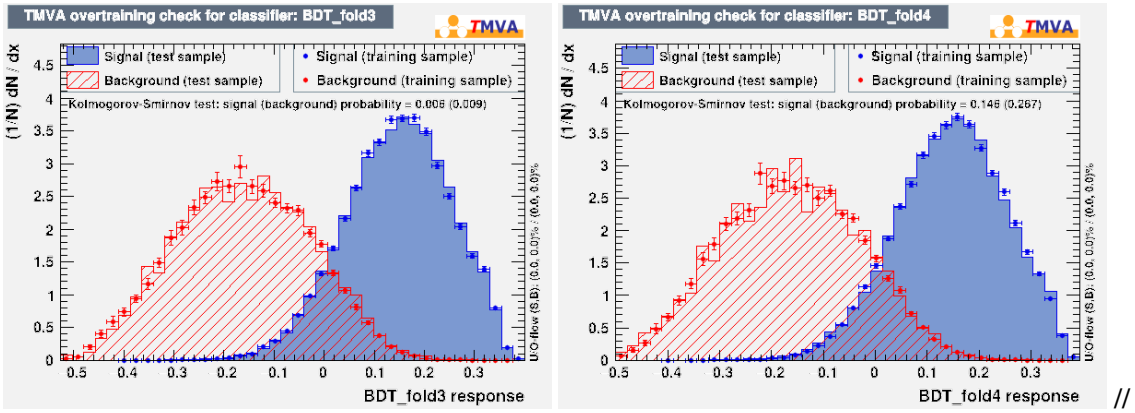

(c) fold3 (d) fold4

Figure 53: BDT distributions for training and test templates in 4 folds

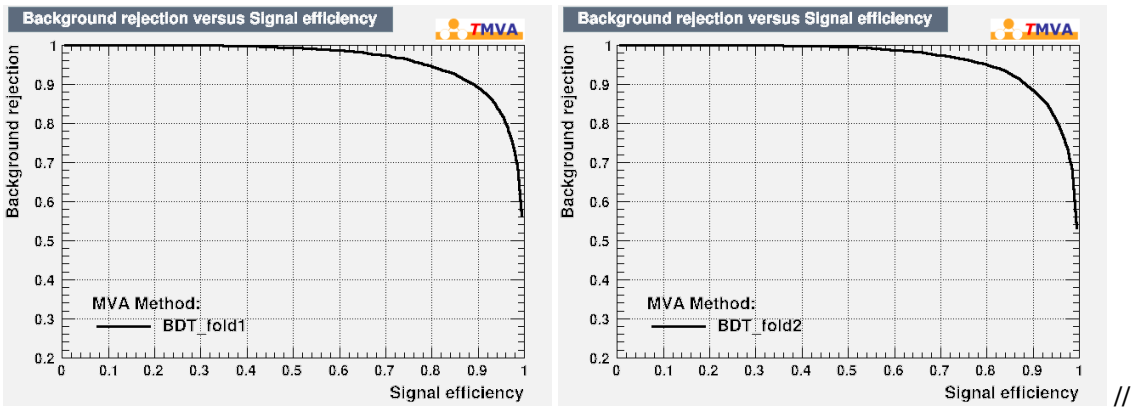

(a) fold1 (b) fold2

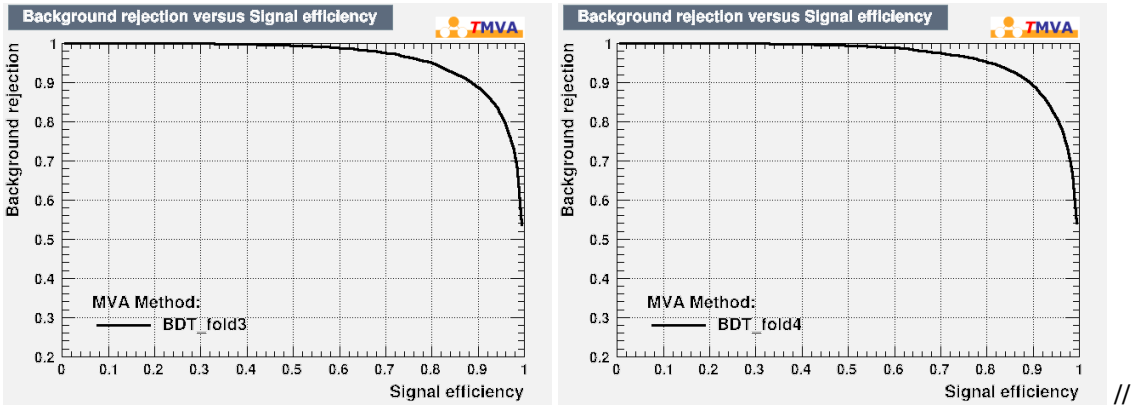

(c) fold3 (d) fold4

Figure 54: Trainned BDT ROC in 4 folds

D.1.4 $m_S \geq 400$ GeV

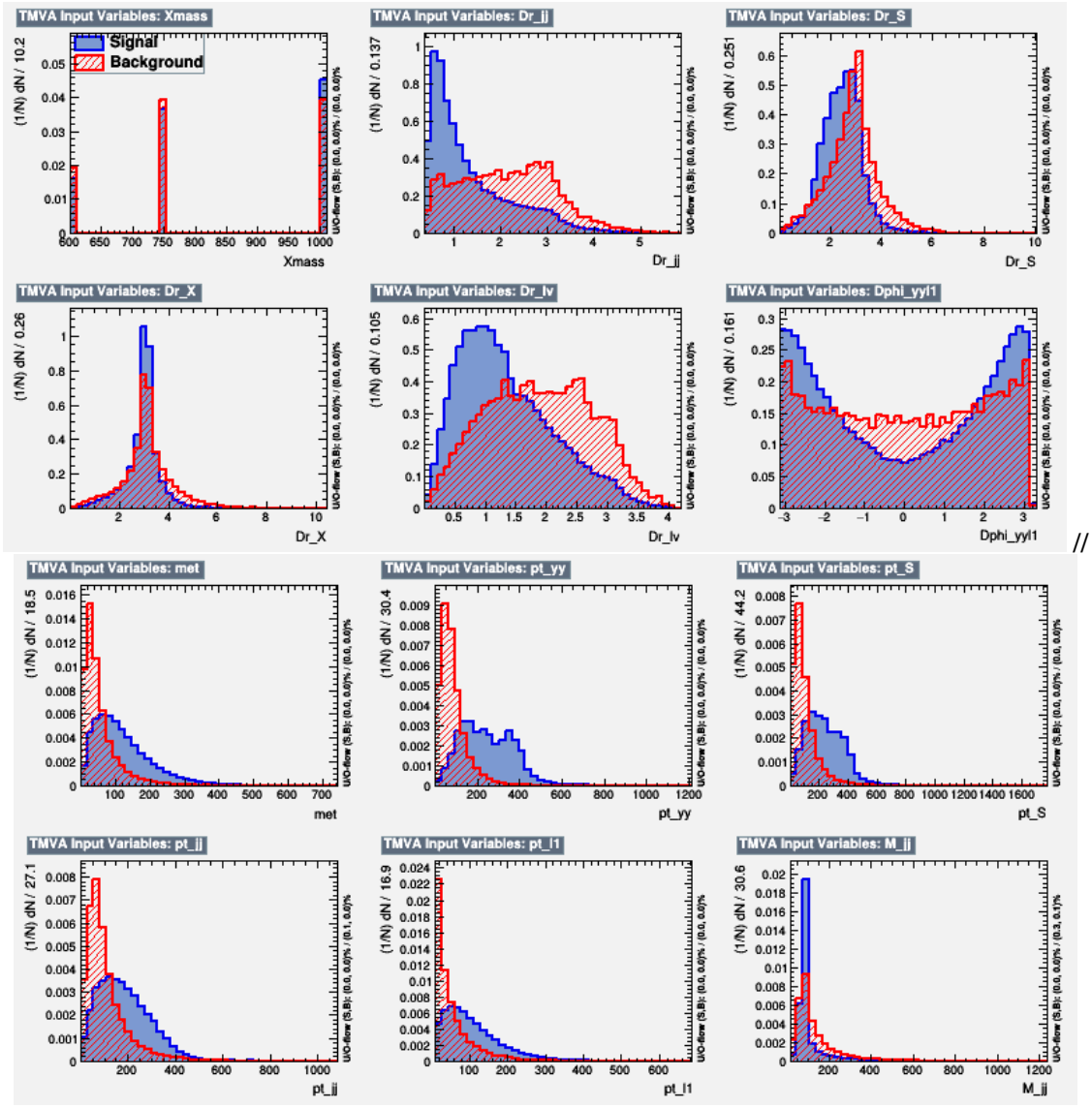

Figure 55: Input variables for BDT in WW1l category.

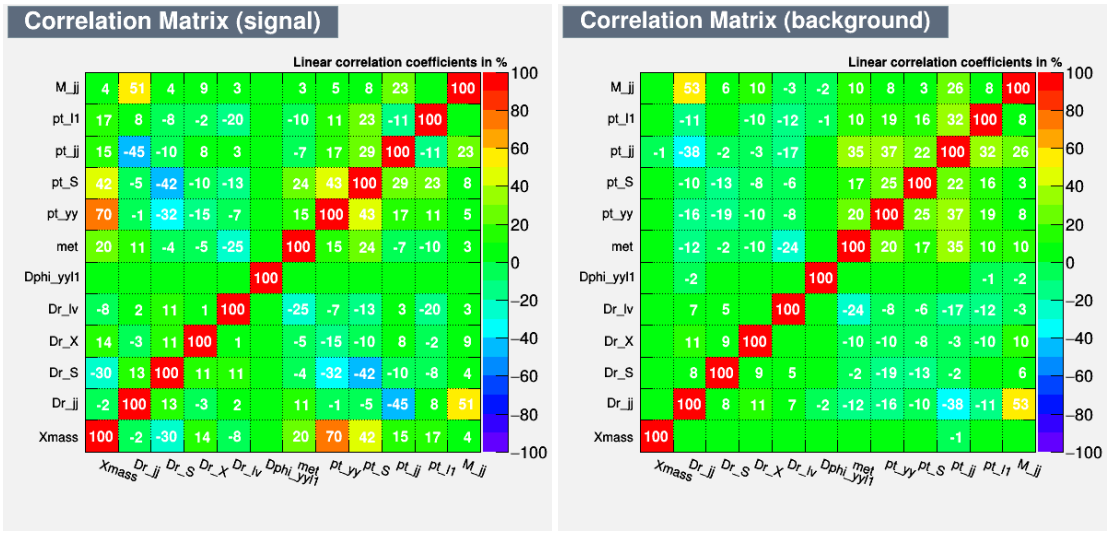

(a) Signal (b) Background

Figure 56: Input variables' correlation in WW1l category.

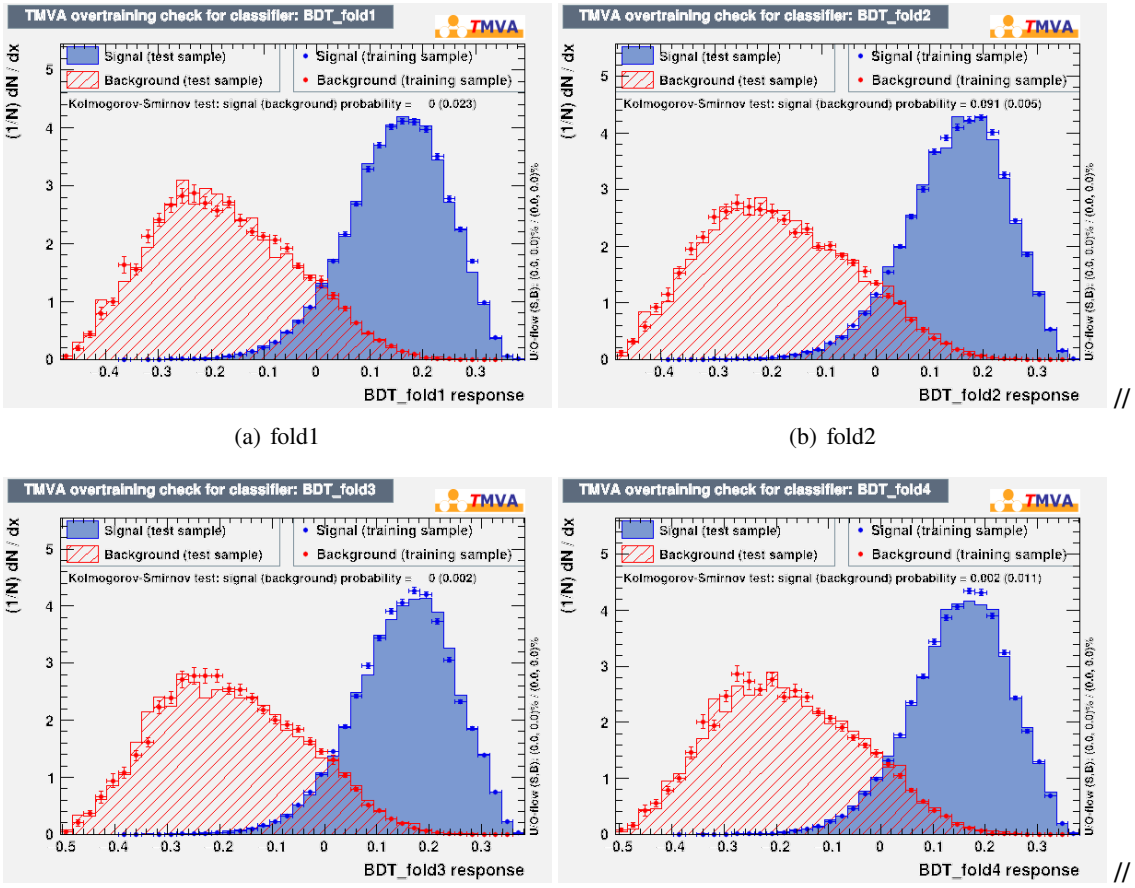

(a) fold1 (b) fold2

(c) fold3 (d) fold4

Figure 57: BDT distributions for training and test templates in 4 folds

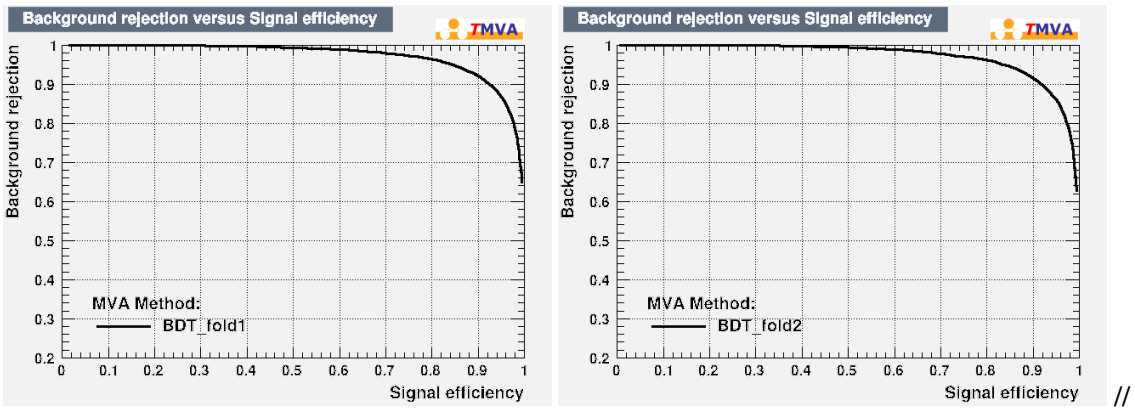

(a) fold1 (b) fold2

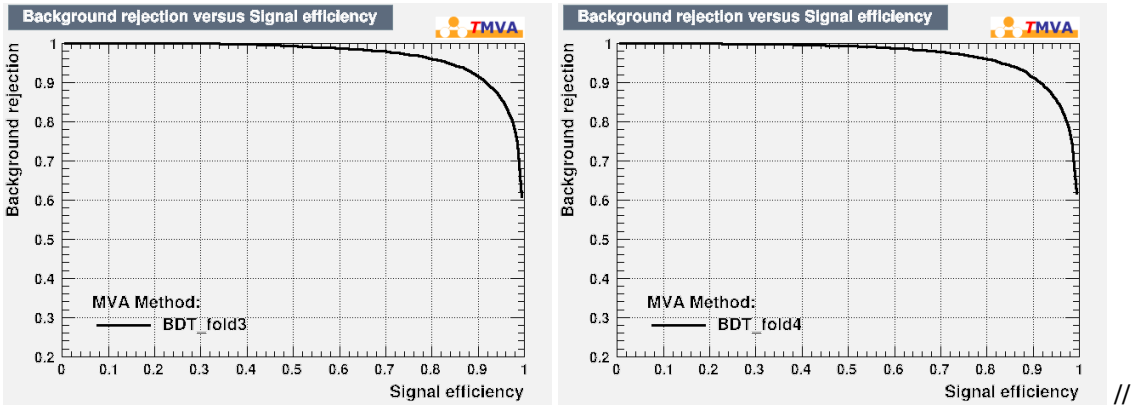

(c) fold3 (d) fold4

Figure 58: Trainned BDT ROC in 4 folds

D.2 WW2l category

D.2.1 m_S = 170 GeV

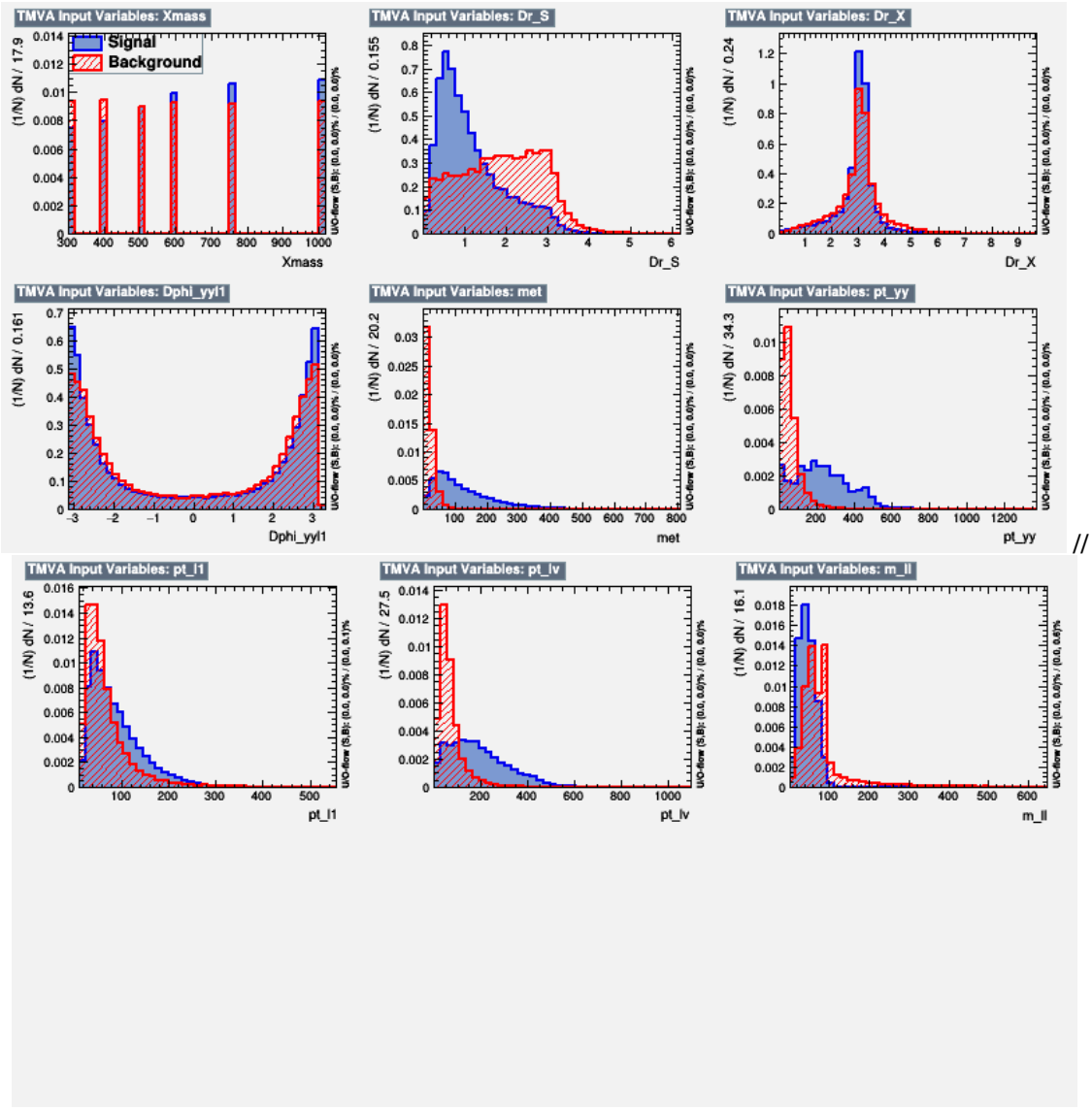

Figure 59: Input variables for BDT in WW1l category.

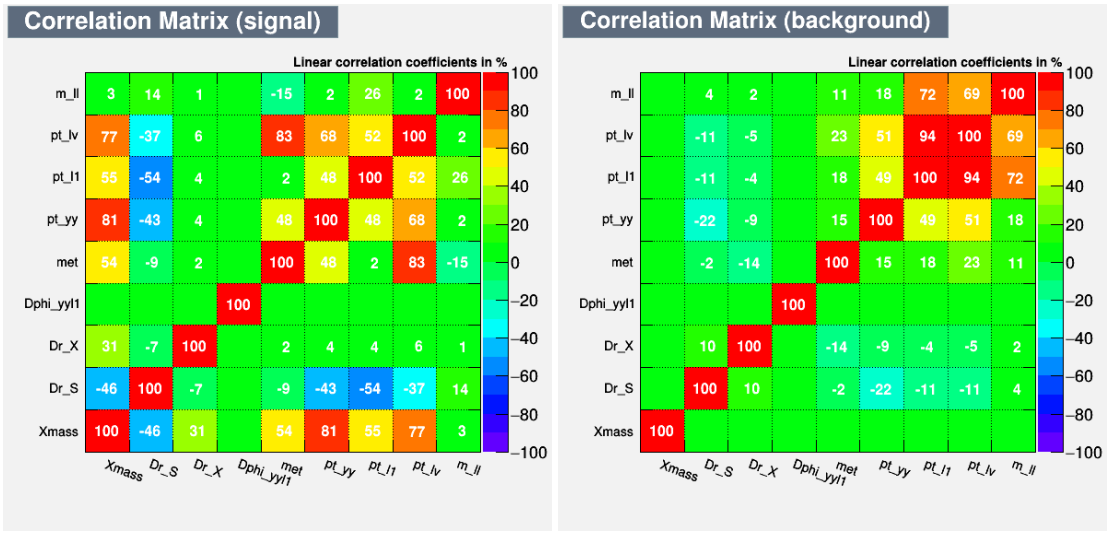

(a) Signal (b) Background

Figure 60: Input variables' correlation in WW1l category.

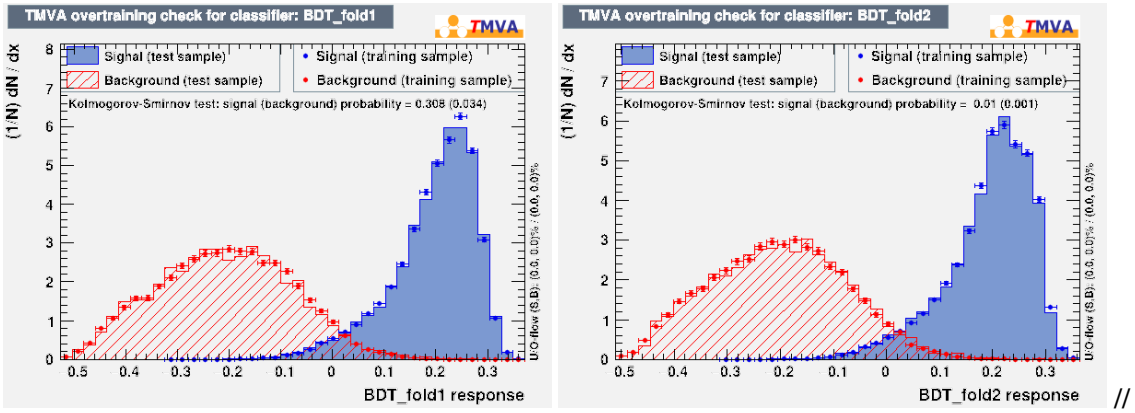

(a) fold1 (b) fold2

(c) fold3 (d) fold4

Figure 61: BDT distributions for training and test templates in 4 folds

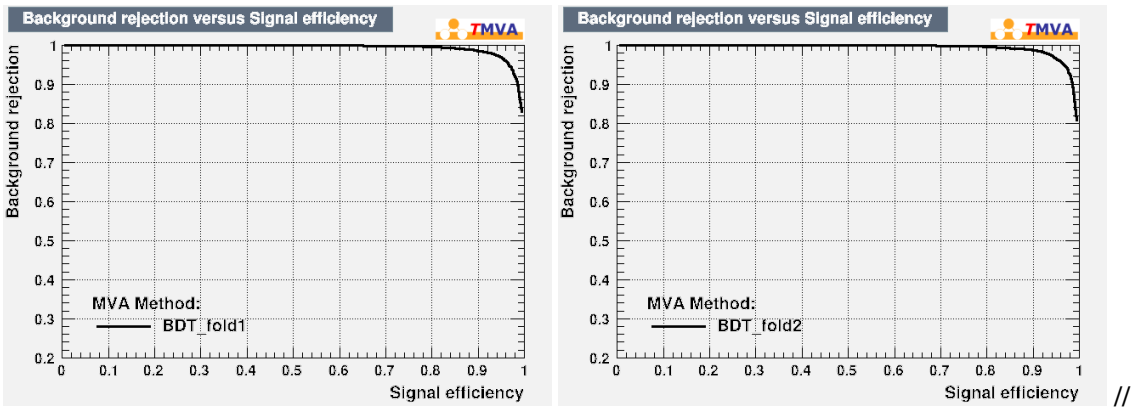

(a) fold1 (b) fold2

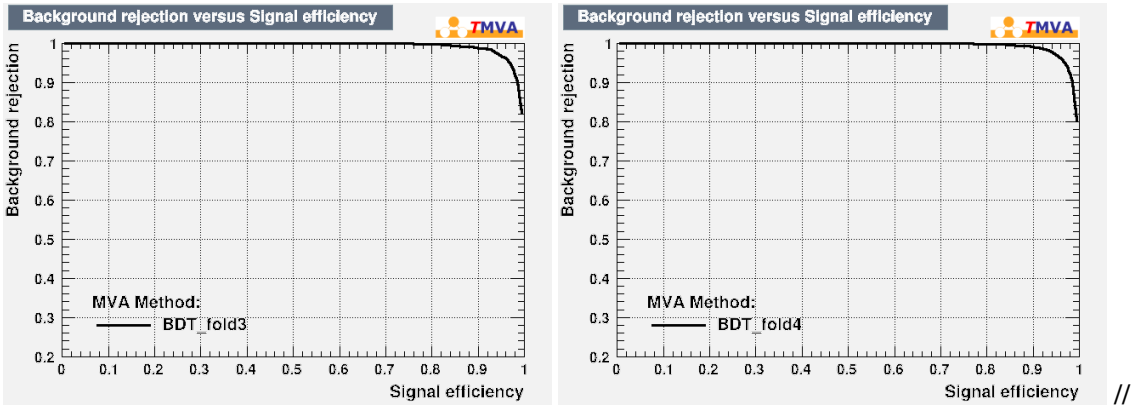

(c) fold3 (d) fold4

Figure 62: Trainned BDT ROC in 4 folds

D.2.2 m_S = 200 GeV

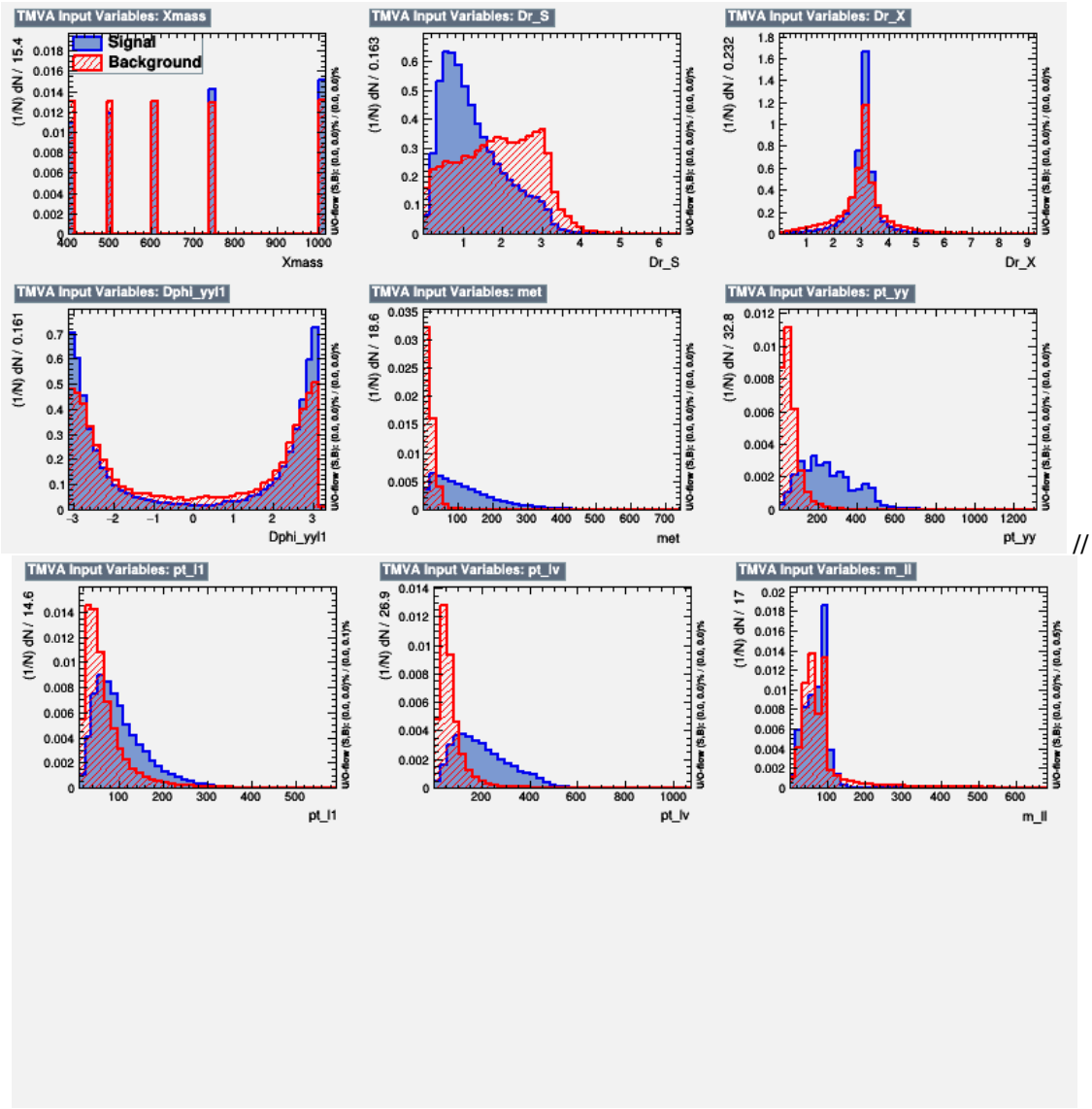

Figure 63: Input variables for BDT in WW1l category.

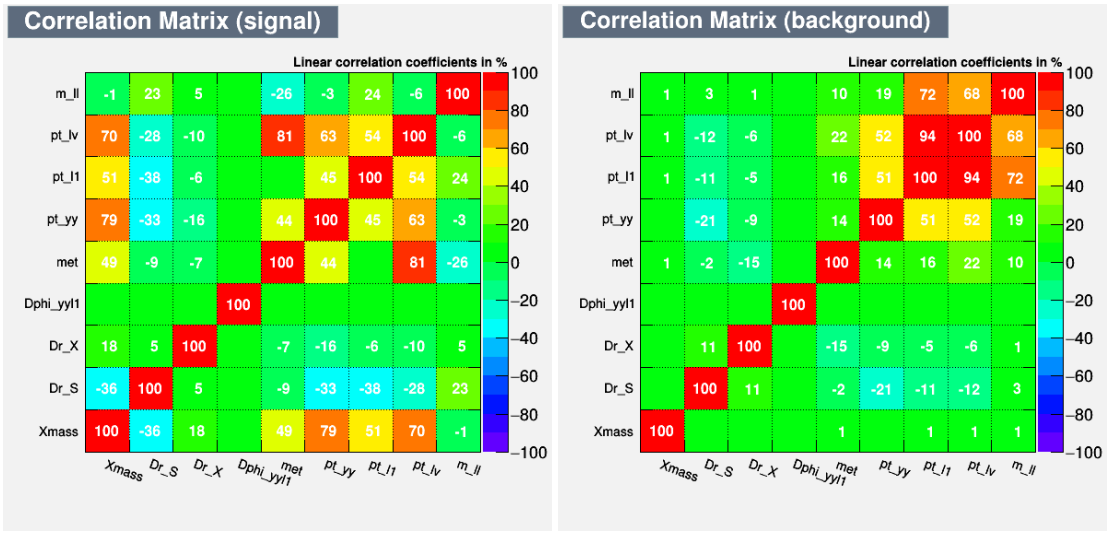

(a) Signal (b) Background

Figure 64: Input variables' correlation in WW1l category.

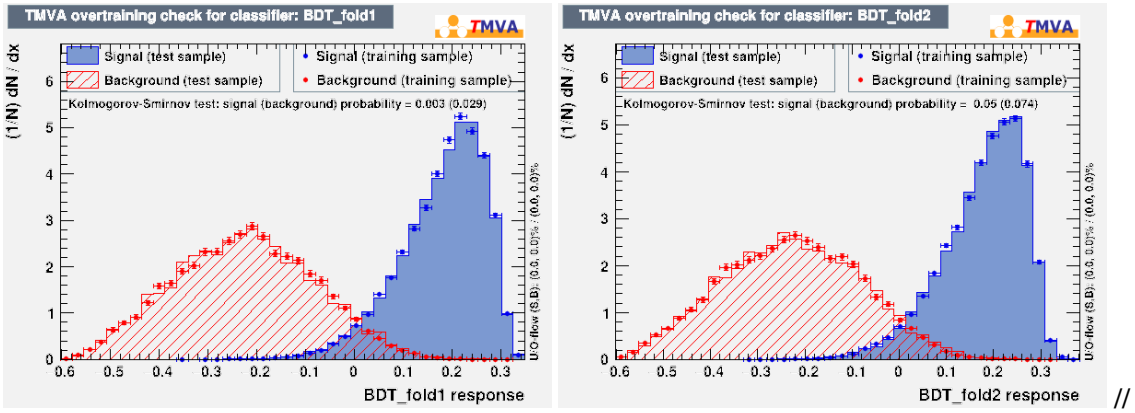

(a) fold1 (b) fold2

(c) fold3 (d) fold4

Figure 65: BDT distributions for training and test templates in 4 folds

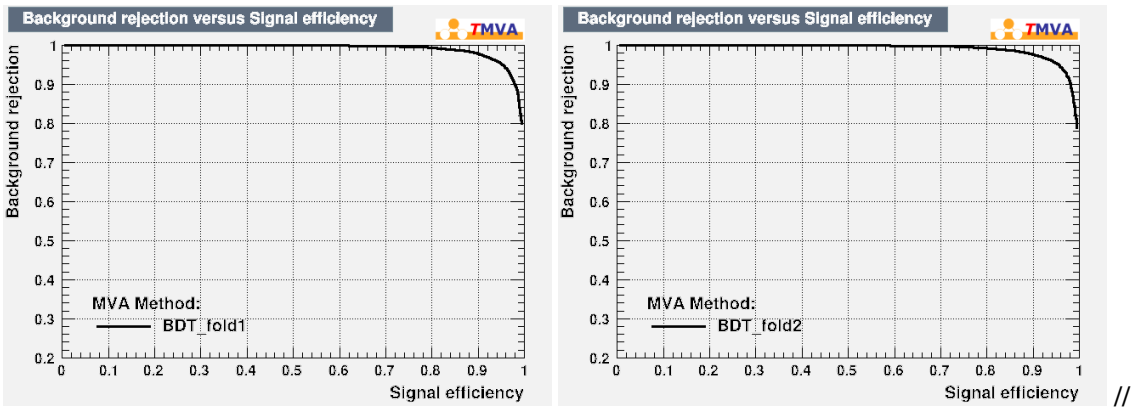

(a) fold1 (b) fold2

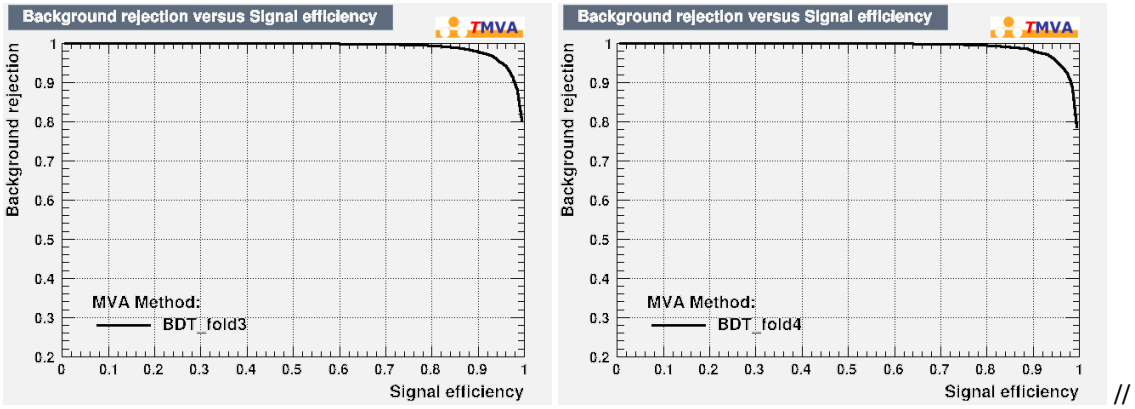

(c) fold3 (d) fold4

Figure 66: Trainned BDT ROC in 4 folds

D.2.3 m_S = 300 GeV

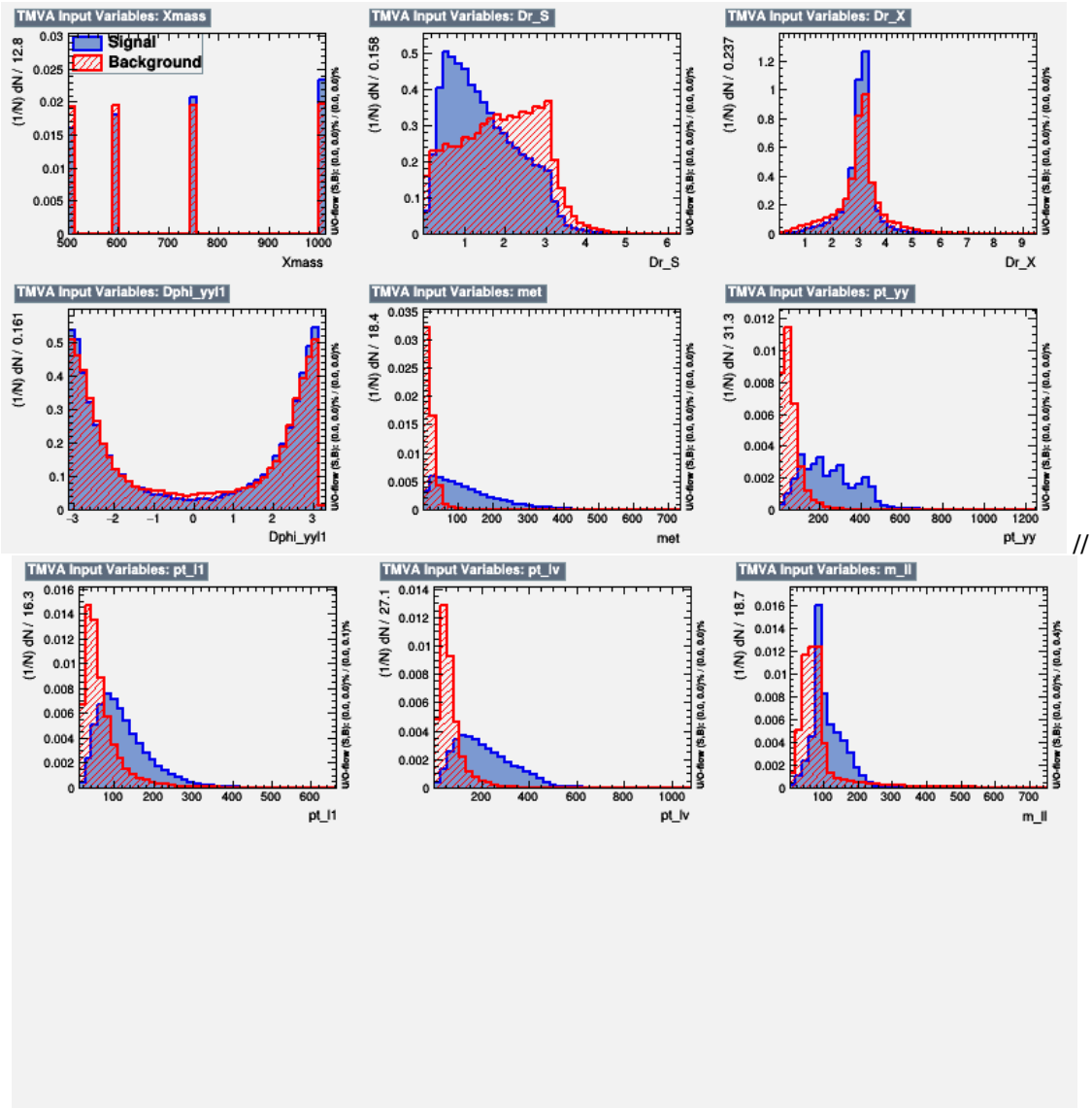

Figure 67: Input variables for BDT in WW1l category.

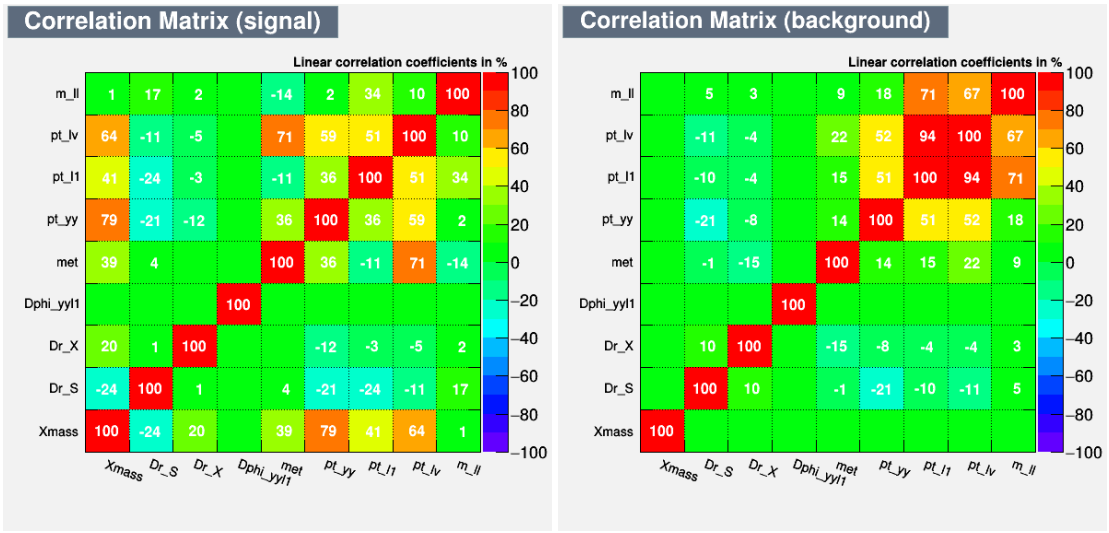

(a) Signal (b) Background

Figure 68: Input variables' correlation in WW1l category.

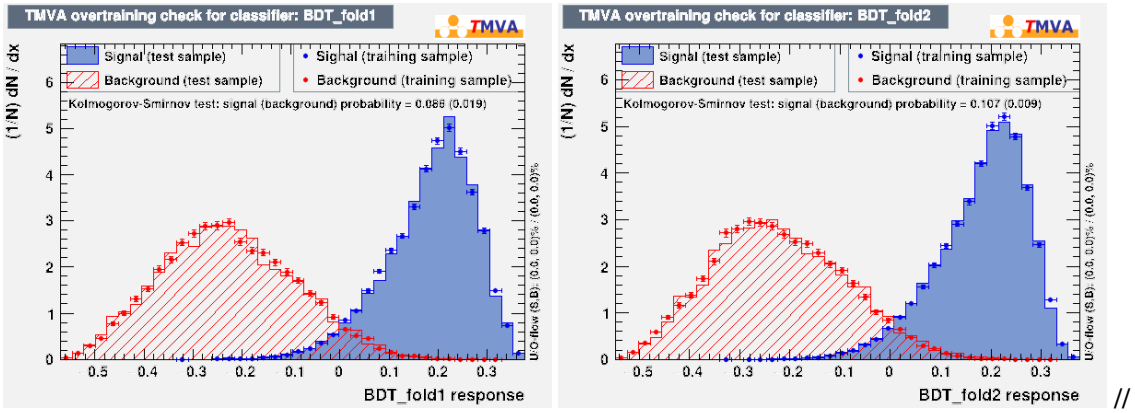

(a) fold1 (b) fold2

(c) fold3 (d) fold4

Figure 69: BDT distributions for training and test templates in 4 folds

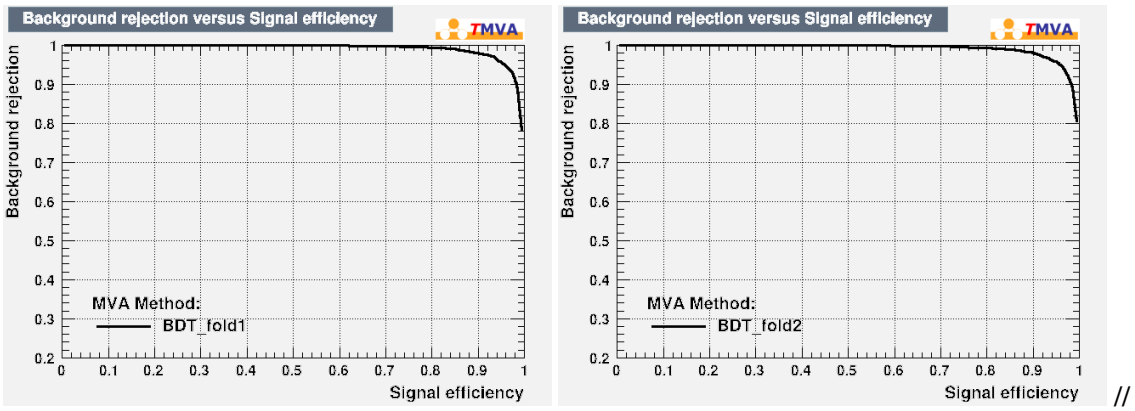

(a) fold1 (b) fold2

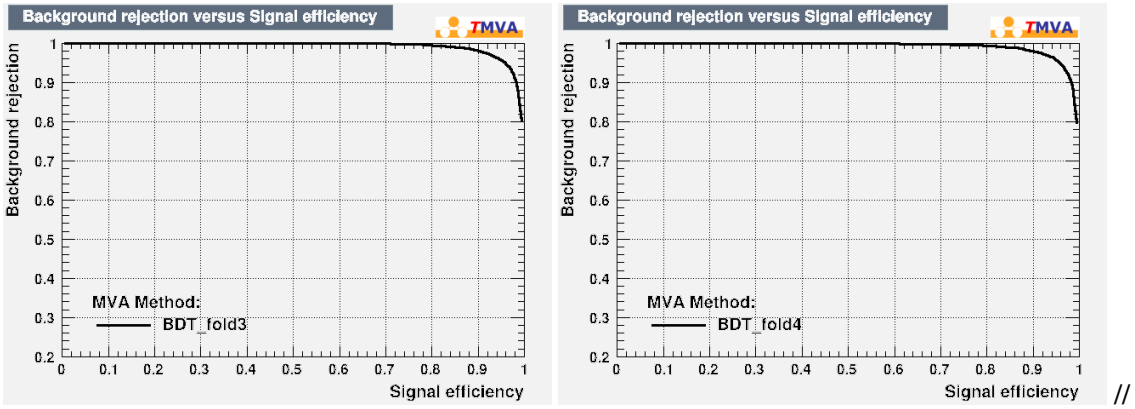

(c) fold3 (d) fold4

Figure 70: Trainned BDT ROC in 4 folds

D.2.4 $m_S \geq 400$ GeV

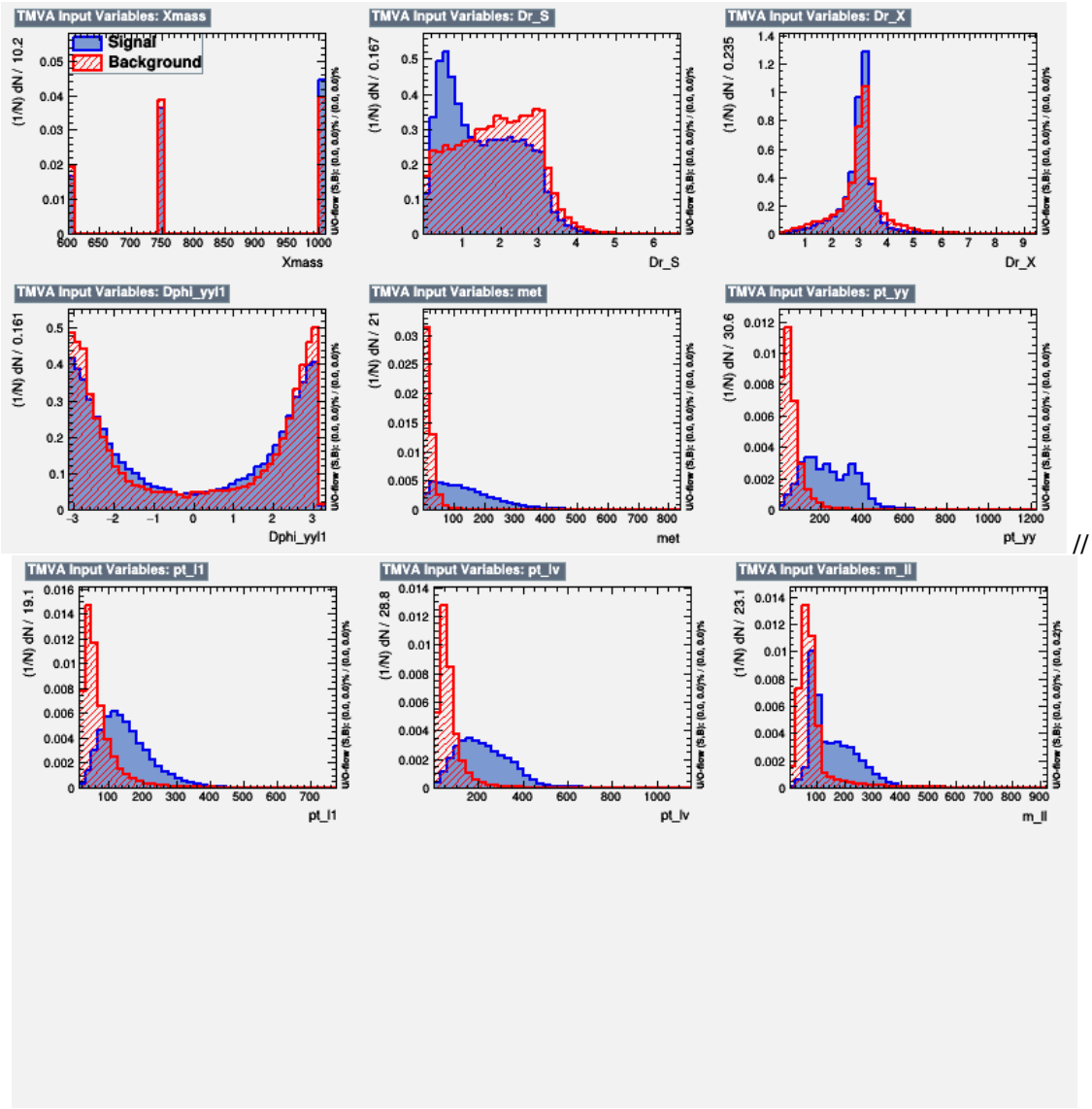

Figure 71: Input variables for BDT in WW1l category.

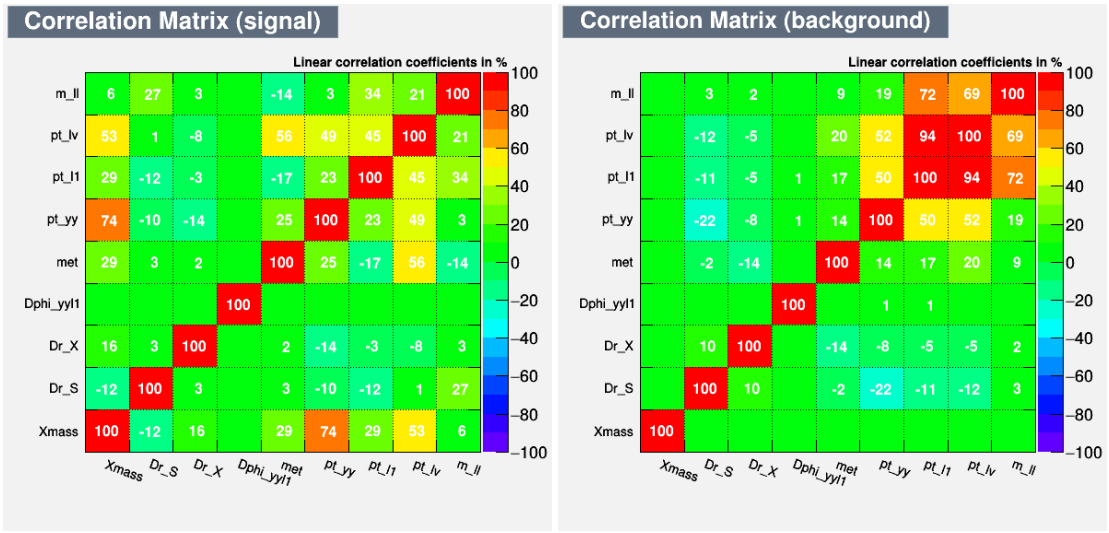

(a) Signal (b) Background

Figure 72: Input variables' correlation in WW1l category.

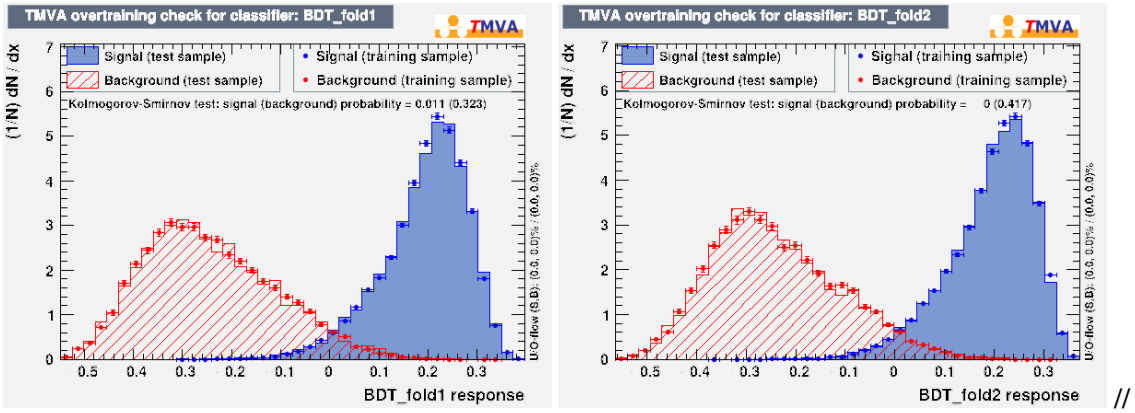

(a) fold1 (b) fold2

(c) fold3 (d) fold4

Figure 73: BDT distributions for training and test templates in 4 folds

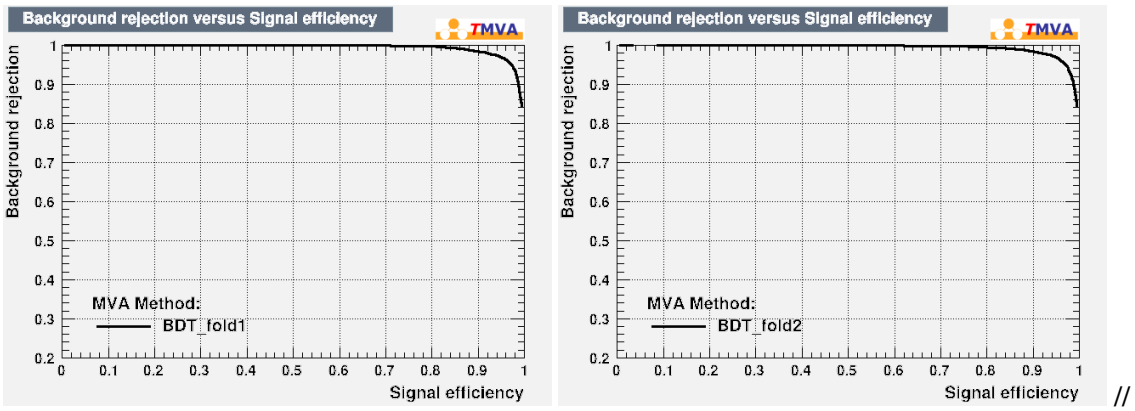

(a) fold1 (b) fold2

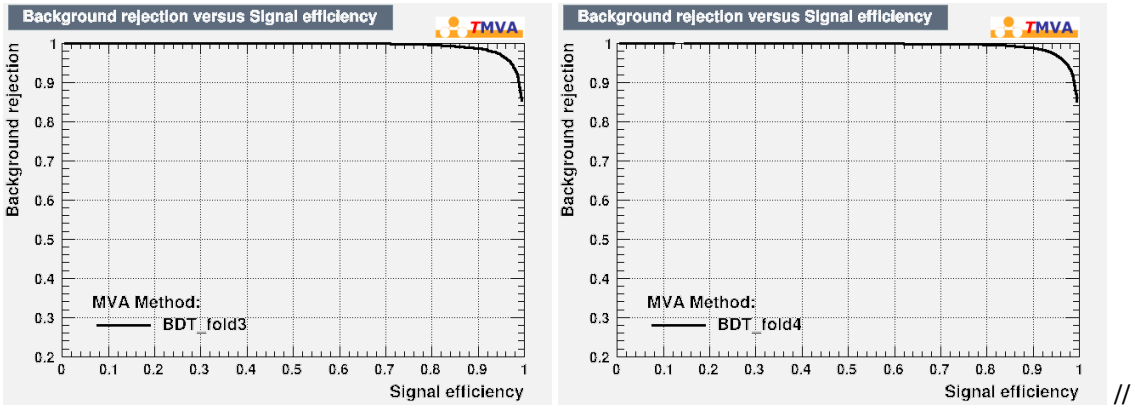

(c) fold3 (d) fold4

Figure 74: Trainned BDT ROC in 4 folds

E Diphoton vertex efficiency in SH signal samples

The efficiency for selecting the correct vertex is studied in $H \to \gamma\gamma$ analysis [29]. It varies between 60% to 100% depending on the diphoton p_{T}, the number of primary vertices in the event, the Σp_T and Σ_T^2 of the hard scattering vertex. And the selection efficiency using an artificial neural network is usually higher than that using the hardest vertex in SM Higgs processes, except for the $t\bar{t}h$ process. The same procedure is repeated in the SH process for validation. 3 mass points of (m_X, m_S) = (1000, 170), (1000, 500) and (600, 400) GeV are considered and merged together, covering a wide $p_T^{\gamma\gamma}$ region from 0 to 600 GeV. For each mass point sample, 20000 events in $\gamma\gamma + lvlv$ channel are used with a mixture of mc16 a, d, e. These events are only required to pass the default HGam selections, i.e. the first 4 criteria listed in Sec. 3. The other selections on leptons and jets are supposed to not influence the diphoton vertex. Figure 75 shows the distribution of $p_T^{\gamma\gamma}$, number of primary vertex and $log(\Sigma p_T^2)$ in the merged samples. In $p_T^{\gamma\gamma}$ plot, the 3 peaks are the signature of 3 mass points. Figure 76 shows the efficiencies of selecting the correct primary vertex as a function of the above variables Figure 77 shows the fraction of events that selected vertex by 2 approaches (hardest vertex and NN) are the same one.

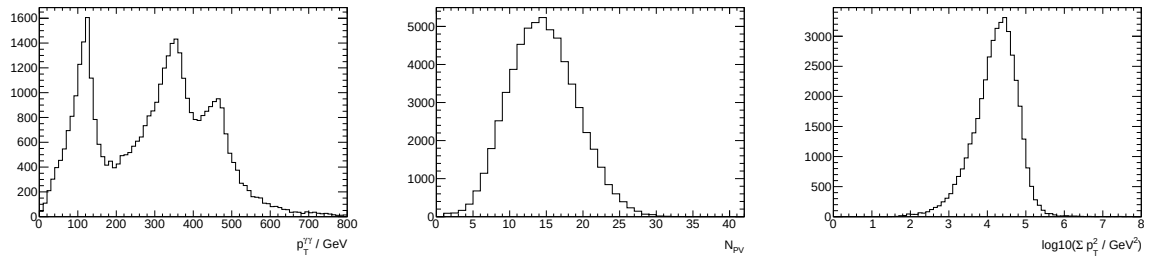

Figure 75: Distributions of $p_T^{\gamma\gamma}$, N_{PV} and $log(\Sigma p_T^2)$ in $SH \to \gamma\gamma + lvlv$ process, with mass points (m_X, m_S) = (1000, 170), (1000, 500) and (600, 400) GeV. Distributions of these variables in SM Higgs sample can be found in Ref [29].

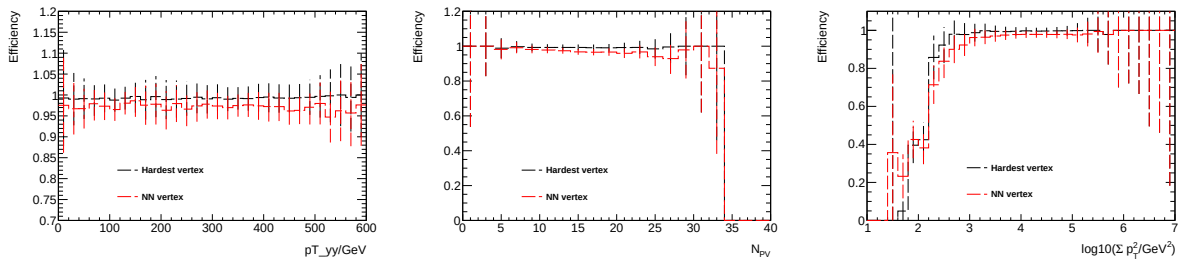

(a) $p_T^{\gamma\gamma}$ (b) N_{PV} (c) $log(\Sigma p_T^2)$

Figure 76: Efficiency of selecting a correct vertex by two approaches as a function of variables.

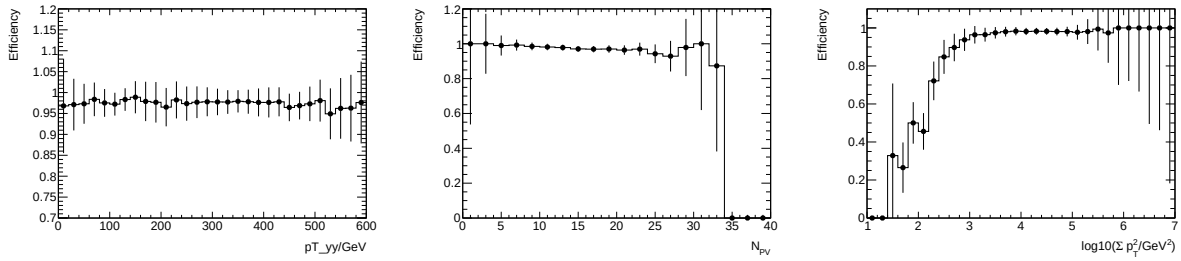

(a) $p_T^{\gamma\gamma}$ (b) N_{PV} (c) $log(\Sigma p_T^2)$

Figure 77: Fraction of the event that selected vertex by 2 approaches are the same one as a function of variables.

F Toy Limits results

In the previous selection, the limits are calculated by the asymptotic method. To validate the assumption that asymptotic should be performed with enough statistics, the limits with the toy are computed. For a first-step check, the result of mass point $m_X = 1000$ GeV, $m_S = 300$ GeV. The μ is scanned from 0 to 0.3, having 5000 toys SplusB and Bonly. The result documented in Table 25 shows the difference between asymptotic and toy is acceptable .The issue at $+2\sigma$ band is due to the wrong setup of the scanned range of μ. Results with 1000 toys where the range of μ is from 0 to 0.4: 0.310 ($+2\sigma$), 0.224 ($+1\sigma$), 0.152 (Median), 0.112 (-1σ), 0.067 (-2σ) , giving the confidence that the issue can be fixed with a wider POI range.

	$+2\sigma$	$+1\sigma$	Median	-1σ	-2σ
Asymptotic	0.348	0.227	0.152	0.109	0.081
toy	10.00	0.215	0.153	0.116	0.097

Table 25: The expected limits of the search $m_X = 1000$ GeV, $m_S = 300$ GeV with asymptotic and toy.

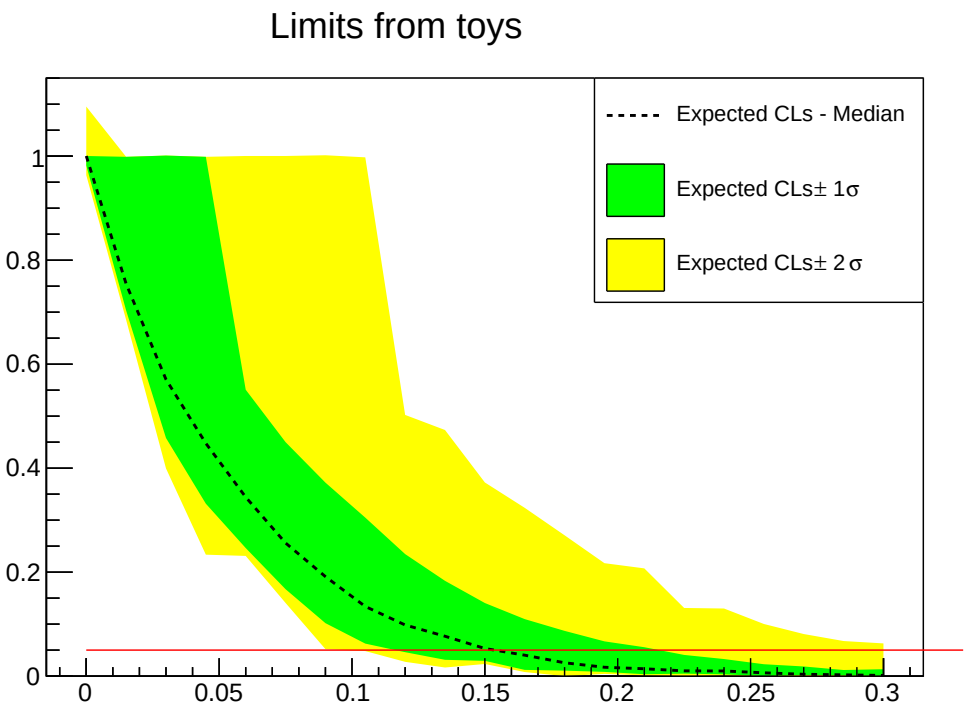

Figure 78: The expected limits of the search $m_X = 1000$ GeV, $m_S = 300$ GeV with toy.

G Signal Injection Test

To test the robustness of the model used in the binned likelihood fit, a signal injection test is applied. In the test, the signal plus background model is fitted to various signal plus background toy datasets in which the signal strengths are set to 1, 1.5 and 2 respectively. The fitted signal strength distributions with 5000 toys for these three cases are shown in Figure 79. It is obvious that the fitted signal strengths peaked at the nominal values following mostly the Gaussian distributions and the deviations are relatively small and stable. The σ of the signal strength is about 0.2, so it is in expected considering the left signal plus background events usually less than 10 in the BDT tight region.

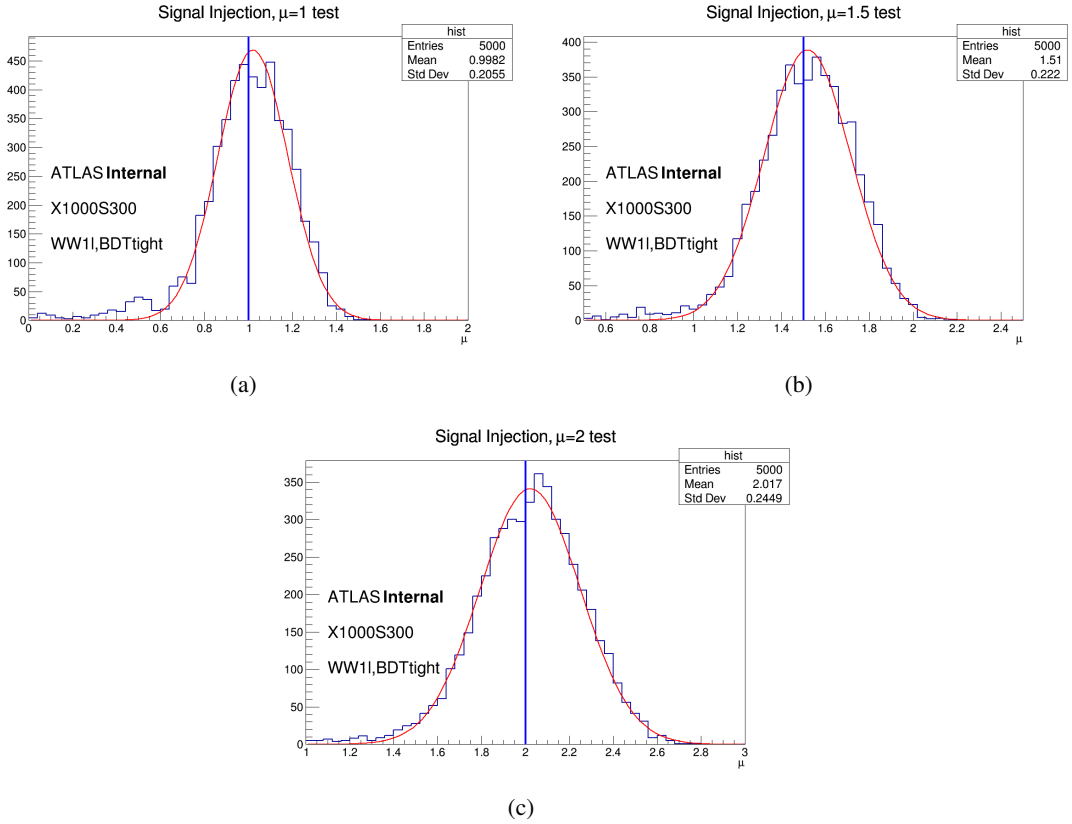

Figure 79: Signal strength distributions in the test of the signal injection with $\mu = 1, 1.5$ *and* 2. Tests are done with the mass point (mX,mS) =(1000,300) and 1 lepton BDT tight region is chosen.